FACULTY OF TECHNOLOGY

EFFECT OF BENDING PARAMETERS ON BENDING FORCES AND SURFACE STRAINS IN AIR BENDING OF ULTRA-HIGH STRENGTH STEELS

Aki-Petteri Pokka

DEGREE PROGRAMME OF MECHANICAL ENGINEERING

June 2020

ABSTRACT

Effect of bending parameters on bending forces and surface strains in air bending of ultra-high strength steels

Aki-Petteri Pokka

University of Oulu, Degree Programme of Mechanical Engineering

Master's thesis 2020, 65 p. + 25 p. appendixes

Supervisors: D.Sc. (Tech.) Antti Kaijalainen, M.Sc. (Tech.) Anna-Maija Arola

The aim of this thesis is to investigate the effects of different parameters on bending forces and strains on the outer surface, and to study the bendability of ultra-high strength steels as well as their behaviour in bending. The aim is to provide a basis for further research by testing the effect of a wide variety of parameters such as punch radius, rolling direction and punch velocity on bendability. The bendability is investigated experimentally with bending tests, utilising Digital Image Correlation (DIC) for optical strain measurement of the outer surface of the specimen.

Punch radius was found to have the greatest effect on the distribution of strain on the outer surface. Smaller punches resulted in significantly higher and more localised deformation. Using punches with smaller radii than the recommended minimum for the material was found to result in shear banding and cracking on the specimen surface. The three studied steel grades, S700MC, S900MC and S1100, were found to distribute strain very differently. The S700 grade was found to distribute strain most evenly, while the S900 had the most localised strain distributions. The S1100 grade was found to be the most susceptible to fracturing, even if the strain distributions were generally wider and the maximum strains on the surface lower than in the S900. The rolling direction was found to have varying effects on each grade. For the S700 and S900, bendability was better in transversal direction. For the S1100, the bendability was either equal or slightly better in the longitudinal direction. Multi-breakage was found to affect both the bending force and strains significantly. After the sheet was observed to separate from the punch, indicating a shift from 3- to 4-point bending, the bending forces were found to start increasing and the maximum strains to start stagnating as the distribution started to grow more from the sides. Punch velocity was not found to have any measurable effect on either strain or force.

Although some trends could be seen from the results, it was conceded that the sample sizes of the individual parameter combinations were small. The presented results and the measurement data are considered useful for improving bending simulation and numerical models, and as a basis for further research, through which some of the findings may be generalised and used for improving workshop instructions.

Keywords: Ultra-high strength steel, Air bending, Bendability, Strain, Force

TIIVISTELMÄ

Särmäysparametrien vaikutus särmäysvoimiin ja pintavenymiin ultralujien terästen särmäyksessä

Aki-Petteri Pokka

Oulun yliopisto, Konetekniikan tutkinto-ohjelma

Diplomityö 2020, 65 s. + 25 s. liitteitä

Työn ohjaajat: TkT Antti Kaijalainen, DI Anna-Maija Arola

Tässä työssä tutkitaan eri työkalujen, särmäysparametrien sekä särmättävän materiaalin vaikutuksia ultralujien terästen särmäysvoimiin ja venymiin särmän ulkopinnalla. Työn tavoitteena on kartoittaa laajalla alalla eri parametrien, kuten painimen koon, valssaussuunnan ja särmäysnopeuden vaikutuksia ultralujien terästen särmäykseen, tutkia ultralujien terästen särmättävyyttä ja niille tyypillistä käyttäytymistä särmäyksessä sekä toimia pohjana jatkotutkimukselle. Työssä pyritään selvittämään näitä vaikutuksia ja syy-seuraussuhteita kokeellisesti särmäyskokeiden avulla, hyödyntäen digitaalista kuvakorrelaatiota (DIC) särmän ulkopinnan venymien optiseen mittaukseen.

Painimen koon todettiin vaikuttavan venymäjakaumiin eniten. Pienemmillä painimilla venymät keskittyivät pienemmille alueille, mikä johti merkittävästi suurempiin paikallisiin venymiin. Suositeltuja minimisärmäyssäteitä pienempien painimien käytön havaittiin johtavan kuroumajuovien ja säröilyn syntyyn materiaalin pinnalla. Venymän jakautumisessa pinnalla havaittiin suuri ero tarkasteltavien terästlaatujen, S700MC, S900MC ja S1100, välillä. Tasaisimmat jakaumat havaittiin S700-laadulla ja suurimmat paikalliset venymät S900-laadulla. S1100-laadun todettiin murtuvan herkimmin, vaikkakin venymäjakamat olivat sillä S900-laatua tasaisemmat. Valssaussuunnan vaikutus vaihteli tarkasteltavien materiaalien välillä. S700- ja S900-laaduilla särmättävyys oli parempi poikittaisessa suunnassa valssaussuuntaan nähden, kun taas S1100-laadulla särmättävyys oli pitkittäin yhtä hyvä tai hiukan parempi kuin poikittain. Levyn irtoamisen painimesta (ns. multi-breakage) todettiin vaikuttavan merkittävästi sekä voimiin että venymiin ultralujien terästen särmäyksessä. Levyn irrottua särmäysvoimien havaittiin nousevan ja venymäjakaumien alkavan kasvaa sivuilta. Särmäysnopeudella ei havaittu olevan vaikutusta mitattuihin voimiin tai venymiin.

Tuloksista voitiin havaita tiettyjä taipumuksia ja pääsuuntia eri tekijöiden vaikutuksista, mutta kunkin parametriyhdistelmien otoskoot myönnettiin pieniksi. Tuloksia ja kerättyä mittausdataa voidaan hyödyntää särmäyssimulaatioiden ja numeeristen mallien kehityksessä, sekä jatkotutkimuksen pohjana. Jatkotutkimuksen kautta tuloksia voidaan pyrkiä yleistämään ja edelleen hyödyntämään ohjeistusten kehittämisessä.

Asiasanat: Ultraluja teräs, särmäys, särmättävyys, venymä, voima

FOREWORD

The aim of this thesis is to provide a basis for further research by taking a broad look into the effects of a wide variety of parameters on bending. The thesis was conducted in a period of 7.1. – 11.6.2020. I would like to thank Anna-Maija Arola and Antti Kaijalainen for their supervision and help throughout the work process, as well as professor Jari Larkiola for his great feedback and advice. I would also like to thank Vili Kesti and Lars Troive at SSAB for their collaboration, feedback, and valuable information. Finally, I would like to thank my family and friends for their support and for maintaining my sanity during the ongoing pandemic.

Oulu, 11.6.2020

Aki-Petteri Pokka

TABLE OF CONTENTS

LIST OF SYMBOLS AND ABBREVIATIONS

A_5	total elongation in uniaxial tension
A_r	area reduction in uniaxial tension
b	bend length (specimen width)
DIC	digital image correlation
F_b	bending force
F_n	normal force at die shoulders
L_0	length of moment arm at the start of bending (half die width)
l_d	length of moment arm
M	bending moment
m	strain rate sensitivity
n	strain hardening exponent
R1t,R2t…	punch radius equal to the sheet thickness, twice the sheet thickness etc.
RD	longitudinal bending direction
R_d	die shoulder radius
R_i	radius of curvature of the inner surface
R_m	ultimate tensile strength
R_n	radius of curvature of the neutral axis
R_p	punch radius
$R_{p0.2}$	0.2% offset yield strength
S	punch stroke
s	arc length of a curve
T,t	sheet thickness
TD	transversal bending direction
V_p	punch velocity
W	die width
α	bending angle
ε, ε_b	strain, strain on the outer bend surface
θ, φ	half bending angle, tangential angle
κ, κ_n	curvature of a curve, curvature of neutral axis
μ	friction coefficient
ν	Poisson’s ratio
σ, σ^*	stress, unit moment

1 INTRODUCTION

Ultra-high strength steels (UHSS) are widely used in applications which require high strength without the increased weight from thicker sheets, such as lifting equipment and the automotive industry. Bending is a common method for sheet-metal forming and understanding the behaviour of UHSS in the bending process is necessary for effective utilisation of these materials in the mechanical engineering and metals industries.

The high strength of UHSS comes with the disadvantage of low bendability and formability in general. UHSS have generally comparatively low fracture strains and cannot sustain large amounts of local deformation. Bending as a forming method for UHSS can be challenging in this regard, as the deformation in bending tends to concentrate in the middle of the bend, leading to high local deformations. To counteract this, large radius punches are used in bending of ultra-high strength steels in an effort to spread the deformation to a larger area and avoid fracturing. Large radius bending, however, also comes with disadvantages such as higher bending forces, larger springback, and a noncircular, nut-like bend shape resulting from the shift from three-point to four-point bending in the so-called multi-breakage effect.

The aim of this thesis is to provide a broad investigation of the effects of different tools and parameters on the bending forces and strain distributions, and thus contribute to better understanding of UHSS bendability and behaviour in large radius air bending. The aim is also to provide a basis for further research by testing a large amount of different parameter combinations. As a by-product of the thesis, the large amounts of data gathered from the thesis experiments can be used for improving bending simulation and numerical models. Also, in the process, the reliability and capability of the experimental setup and procedures are further tested and improved on.

The main focus of this thesis is on the experimental part, although the basic theoretical background and concepts, that are relevant for the experiments, are also covered in the literature review. The bending experiments are carried out on ultra-high strength structural steels of 700, 900 and 1100 MPa grades, using a universal tensile testing machine with purpose-build bending tools that allow optical strain measurement of the specimen surfaces via Digital Image Correlation (DIC). The results of the experiments,

along with noteworthy observations and conclusions, are presented with numerous graphs and pictures of the specimens.

2 AIR BENDING

Bending is a widely used method of sheet-metal forming that has various applications ranging from customised fabrication of single parts to mass production of parts and products of all sizes. Bending is particularly useful because of its relatively fast speed, cost-effectiveness, and flexibility. Bending can also be used in place of welding in some applications. Bending is usually carried out at room temperature, but higher temperatures can be used as well, in order to decrease the bending forces and to increase the formability of materials with poor ductility or large cross-sections. (Lange 1985, p. 19.2; Arola et al. 2015a)

The most significant types of sheet-metal bending processes include air-bending, die bending, folding, roll bending and bending with pliable tools. Air bending is a process where the sheet, supported by two die shoulders, is bent with a punch stroke without bottoming or striking. Air bending is especially useful in small batch part manufacturing because of its flexibility and efficiency as a bending process. With air bending, it is possible to achieve different bend angles without tool changes just by controlling the punch displacement. This ability enables relatively easy compensation for variations in spring-back between different materials and sheet thicknesses without changing tools. Air bending also requires relatively small bending forces in comparison to other bending processes that involve bottoming. (Wang et al. 1993; De Vin 2000)

According to Lange (1985, p. 19.17-23), the final shape of the workpiece in air bending is mostly determined by the relative positioning of the tool components, the flow curve of the material and the sheet thickness. The geometry of the individual tool components, i.e. the punch and the die, is considered to have generally little influence on the final shape. It is worth keeping in mind, however, that according to Lange, air-bending is considered to take place only when the sheet has three points of contact to the tools. If the inner radius of the sheet becomes smaller than the punch radius, the load-scheme will shift from three-point to four-point bending and this, according to Lange, concludes air-bending. In addition to the three-point bending, Lange also counts folding as air bending, as long as the smallest inner bend radius of the sheet is larger than the radius of the clamping die. In this thesis, air bending is defined according to De Vin (2000) and Wang et al. (1993).

2.1 Bending tests

The main purpose of bending tests, according to Newby (1985), is determining the ductility or strength of a material. While most mechanical tests have an objective endpoint, e.g. the failure of the specimen, the endpoint in bending tests is subjective. The operator is the sole judge on whether the specimen surface has cracked, i.e. if the material has failed. The test procedures and specimen preparation methods have been developed over time, without close attention to detail and mainly by users instead of mechanical test equipment manufacturers. Consequently, the standardisation has been relatively sparse. Newby mentions two ASTM standards for bending ductility tests – ASTM E190 and ASTM E290. ASTM E190 provides guidelines for bending ductility tests of welds, while ASTM E290 provides guidelines for bending ductility tests of metals in general. (Newby 1985)

Notable standards for bending tests published after 1985 include ISO 7438:2016 and VDA 238-100. The standards provide guidelines for test principle, equipment, specimens, and procedure, while also presenting methods for determining the bend angle from the punch displacement measurements.

Bending ductility tests are conducted to determine either the minimum bend radius or the maximum bend angle of a material. The minimum bend radius is the smallest radius around which the specimen can be bent without its surface cracking and is expressed in multiples of the specimen thickness. As in, if a material has a minimum bend radius of $4t$, it can be bent around a radius equal to four times the thickness of the specimen without cracking. The maximum bend angle is the greatest angle to which the specimen can bent, using a fixed bend radius, without surface cracking. (Mandigo 1985)

2.1.1 Specimen preparation

Sheet and plate specimens do not normally require specific preparations other than cutting to the desired dimensions. Specimens are usually cut either parallel or perpendicular to the rolling direction of the material, but any orientation can be tested. The ductility is generally lower in the longitudinal orientation, where the bending axis is parallel to the rolling direction.

Bending test specimens should have a width-to-thickness ratio (*b/t*) greater than 8:1 whenever possible. When $b/t > 8$, plane-strain conditions apply, and the bending ductility is not affected by the exact *b/t* -ratio. When $b/t < 8$, the test results are strongly affected by the exact width-to-thickness ratio, which may cause unwanted variance in the results unless the specimens are all machined precisely to the exact same dimensions. (Mandigo 1985)

2.1.2 Test method

Bending tests are usually conducted by bending specimens either around progressively decreasing radii while the target angle is fixed, or to progressively increasing angles while the radius is fixed, until the specimen fails or cracks. The specimens are usually examined for cracking visually by the operator. The visual nature of the inspection makes the measurements rather subjective and difficult to properly reproduce as the definition for a visible crack may vary from tester to tester. (Mandigo 1985)

2.2 Stress /strain states

2.2.1 Uniaxial stress

Uniaxial stress is a one-dimensional stress state, where there is stress in only one principal direction, while the other principal stresses are zero. Uniaxial stress can be applied to bending according to the simple-beam theory, where only the tangential stress σ_x (according to the coordinate system illustrated in Figure 1) is assumed to exist and the other principal stresses σ_y and σ_z are ignored. Uniaxial stress state applies best for bending of narrow beams. For wider plates and sheets, the stresses in bending are better described by biaxial or triaxial stress states, where the other principal stresses are also considered. Although not completely accurate for bending of wide plates, the simplifying assumption of a uniaxial strain can be useful for simple models and approximate calculations. (Dadras 1985; Lange 1985, p.19.4)

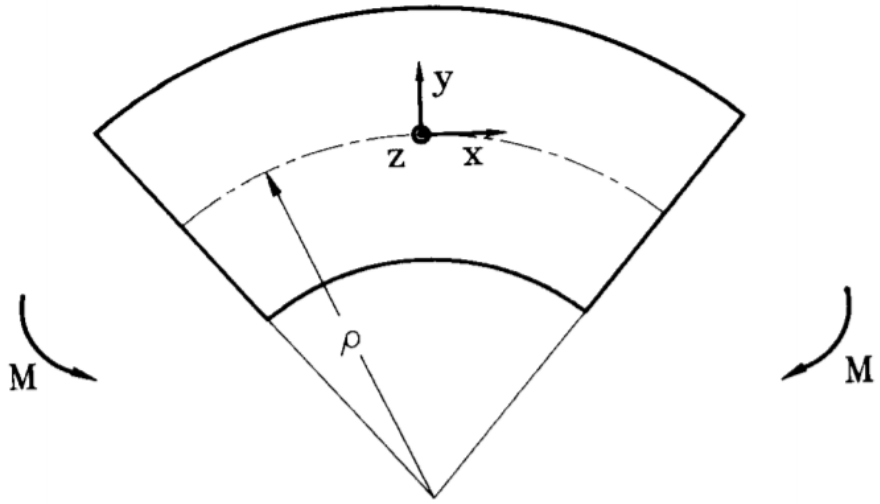

Figure 1. A section of a bent sheet (Perduijn & Hoogenboom 1995)

2.2.2 Plane strain

Plane-strain is a condition where there is strain in two directions but no strain in one direction, i.e. the deformation happens in a plane. Plane-strain occurs commonly in bending of wide sheet metal, where at the central regions of the bend, the strain ε_z parallel to the bend axis is prevented by the surrounding material. Most materials have a minimum in the forming limit curve at plane-strain conditions, as can be seen from the typical forming limit curve in Figure 2, meaning that they fracture at lower strains in plane strain than in other conditions. Assumption of plane strain is common for process models of sheet metal bending, and plain strain condition is indeed assumed in the models for stress and strain presented in this thesis. (Dadras 1985; Lange 1985, p.19.4; Taylor 1988)

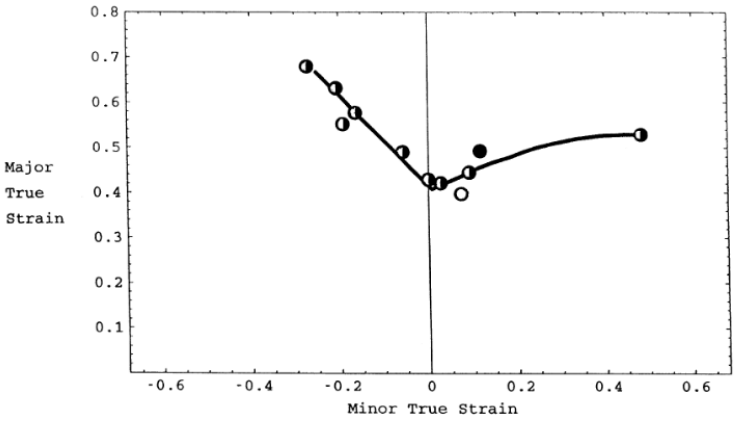

Figure 2. A typical forming limit diagram.

2.3 Bending models

2.3.1 Rigid-plastic and circular-straight models

The rigid-plastic model is a simple model, where the geometry of the bent sheet consists of a circular part with two straight legs (Figure 3). This model can be used for simple calculations for the bend angle and as a reference for describing the effects of different factors and phenomena on the sheet geometry. However, the various simplifying assumptions make the model generally quite inaccurate.

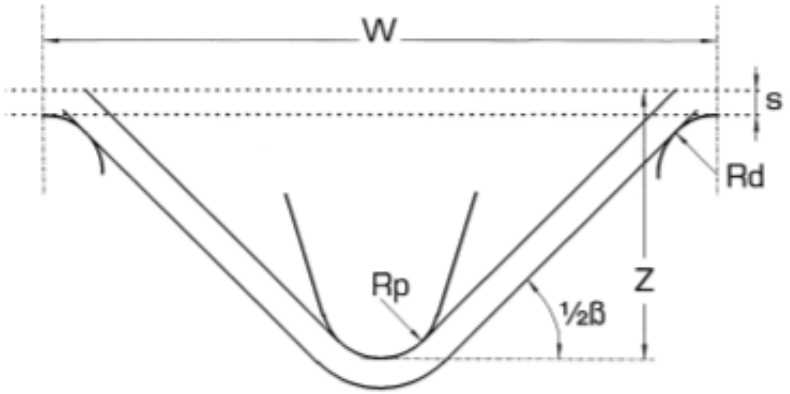

Figure 3. Sheet geometry according to the rigid-plastic model. (de Vin et al. 1996)

The circular-straight model is another simple model, where after unloading, the sheet geometry is assumed to consist of a circular section and two straight legs. The difference to the rigid-plastic model is that in this model, all sections are assumed to also deform elastically, meaning that the spring-back effect can be taken into account. (de Vin et al. 1996)

2.3.2 Wrap-around models

Various bending models (Stelson 1986; Wang et al. 1993; Asnafi 2000; Troive 2017) have been developed over the time, which assume wrap-around behaviour under the punch and calculate the sheet geometry (Figure 4) based on the local bending moments (Figure 5). In these “wrap-around models”, the bending moment under the punch is calculated according to the wrap-around assumption, after which the size of the wrap-around zone is calculated. Based on these calculations, the local bending moments and curvatures can be determined.

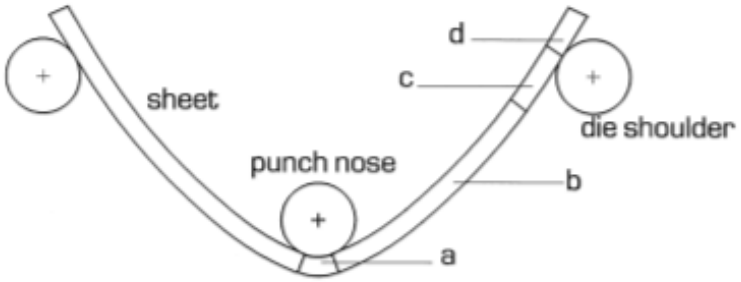

Figure 4. Sheet geometry according to the wrap-around models.

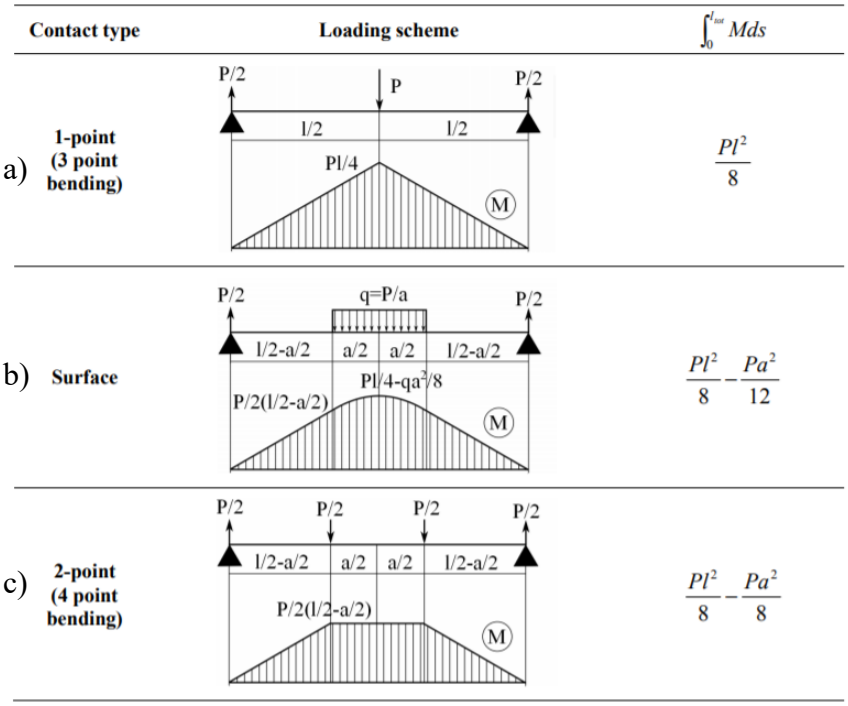

Figure 5. Bending moment distributions in a) 3-point bending, b) wrap-around, and c) 4-point bending. (Vorkov et al. 2014)

In wrap-around models, the geometry of a bent sheet can be generally divided into four sections, or zones, in the direction of the legs of the bent sheet, as shown in Figure 4. Section *a*, the "wrap-around zone", is directly below the punch, where the inner surface of the sheet follows the shape of the punch. In section *b*, the sheet is plastically deformed, and its curvature decreases towards the end of the leg as the local bending moment decreases. Section *c* is near the shoulders, where the sheet is deformed only elastically. Section *d* is beyond the contact-point between the shoulder and the sheet, and thus under no bending moment or deformation. The proportions of the sections depend on material properties, bend angle and tool geometry.

The wrap-around models are more accurate than the rigid-plastic and circular-straight models in their estimation of the sheet geometry and thus provide more accurate approximations for the required punch strokes and bend allowances, as well as for the strain distributions. However, these models are still far from perfect, as the wrap-around assumption limits their accuracy in cases when wrap-around does not occur, like in large radius bending of high-strength steels. (De Vin 2000)

2.4 Springback

Springback describes the characteristic of a bent sheet to straighten after load removal. The deformations that occur in the workpiece during the bending process are a combination of elastic and plastic deformations. After the bending moment is removed, the workpiece will unbend towards its original shape and only the permanent, plastic deformations will remain. Controlling springback is essential in the bending process, as the final shape of the bend (the bend radius and angle) depends on the amount of springback. Acquiring a precise bend shape requires a precise prediction for the amount of springback, which can be difficult in practice for multiple reasons. The amount of springback can be expressed by the springback ratio K:

$$K = \frac{R_n}{R_n'} = \frac{\alpha'}{\alpha} \tag{1}$$

where R_n and α are the radius of the neutral axis and the bend angle before springback, and R_n' and α_r' are the radius and the bend angle after springback.

The springback ratio depends significantly on the work material, as well as the amount of deformation in the sheet, namely the bend radius relative to the sheet thickness. Slight variations in sheet thickness or work material properties between workpieces can cause considerable scatter in springback. This is not a huge problem in single unit production, as these differences can be corrected individually with relative ease. In mass production, however, the scatter must be limited either by having tight tolerances for sheet thickness and material properties, or with an adaptive sheet-bending system based on computer modelling, which calculates the springback for given bending parameters and material properties and adjusts the required overbend to minimise the error. (Lange 1985, p. 19.7-9 & 19.30-34)

2.5 Bend angle estimation

Bend angle estimation is a necessary part of press brake bending and bend testing as it is usually not feasible to measure it directly. Bend angle can be estimated as a function of the punch displacement, tool dimensions and sheet thickness. Several equations of differing complexity and precision have been derived over the time. According to the ISO 7438 standard, the bend angle can be calculated as follows:

$$\alpha_{ISO} = 2\sin^{-1}\left(\frac{L_0 Q+(S-Q)\sqrt{{L_0}^2+(S-Q)^2-Q^2}}{{L_0}^2+(S-Q)^2}\right), \quad (2)$$

Where $Q = R_d + R_p + t$ (3)

L_0 is the half of the die width,

S is the punch stroke,

R_d is the die shoulder radius,

R_p is the punch radius and

t is the sheet thickness.

An expression for the bending angle was presented in VDA 238-100 as follows:

$$\alpha_{VDA} = -2\tan^{-1}\left(\frac{2g}{-h-\sqrt{h^2-4gi}}\sqrt{j^2-\left(\frac{-\sqrt{h^2-4gi}-h}{2g}+L_0\right)^2}-(\mathrm{j}-S)\right), \quad (4)$$

Where $g = {L_0}^2 + (j-S)^2$ (5)

$h = 2L_0\left({L_0}^2 - j^2 + (\mathrm{j}-S)^2\right)$ (6)

$i = j^4 - 2{L_0}^2 j^2 - (\mathrm{j}-S)^2\mathrm{j}^2 + {L_0}^2(\mathrm{j}-S)^2 + {L_0}^4$ (7)

$j = R_d + t$ (8)

Cheong et al. (2017) found the ISO Formula (2) to slightly overestimate the bend angle, which is not surprising, given that it is based on a simplified bending model of a circular part with two perfectly straight flanges. The VDA formula (4) was found to be slightly more accurate, although the authors conceded that factors such as machine stiffness and tooling design were not accounted for. It should also be noted that the VDA formula does not include the punch radius.

Troive (2017) presented an improved formula (9) based on ISO 7438, that also gives slightly smaller values for the bend angle than the ISO formula:

$$\alpha_{Troive} = \frac{1}{R_T}\left(\alpha_{ISO}(R_T + t) - 4tP_2\left[\tan^{-1} P_1 - \tan^{-1}(P_1 - P_2 \tan\frac{\alpha_{ISO}}{4})\right]\right), \quad (9)$$

Where $$P_1 = \frac{R_T}{\sqrt{{L_0}^2 - {R_T}^2}} \quad (10)$$

$$P_2 = \frac{L_0}{\sqrt{{L_0}^2 - {R_T}^2}} \quad (11)$$

$$R_T = R_d + R_p \quad (12)$$

The bend angles in the experimental section of this thesis are calculated according to Formula (9).

2.6 Strain

As illustrated in Figure 6, the outer and inner surfaces of a bent sheet are under tensile and compressive tangential stresses, respectively. As a result of the stress, the material deforms elastically and plastically according to the stress-strain behaviour of the material.

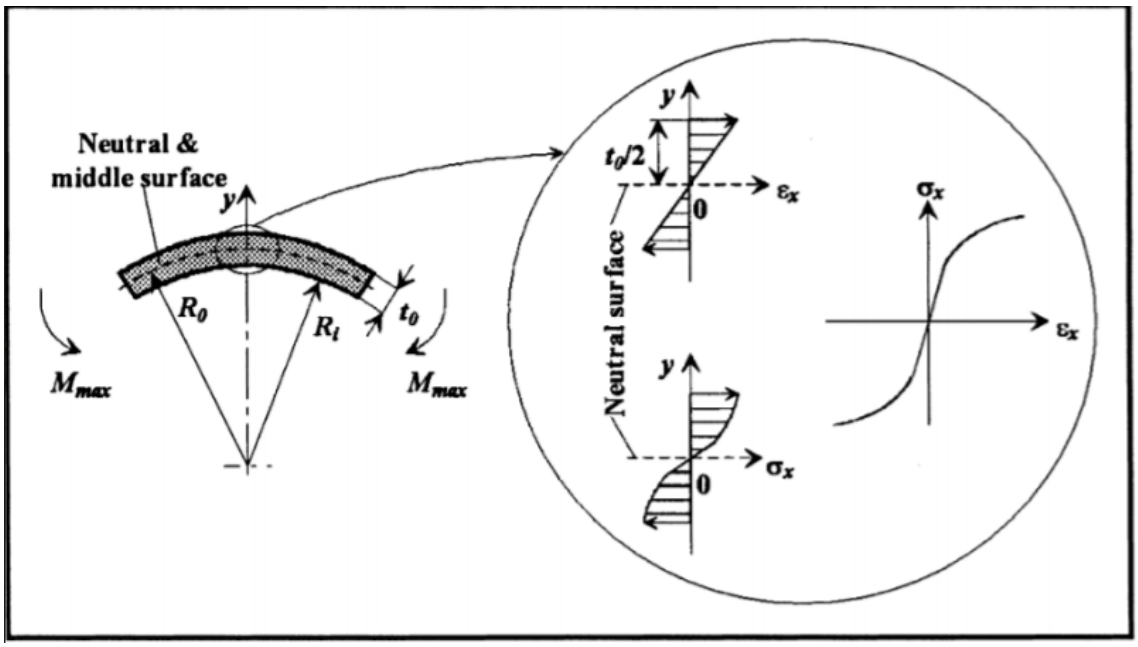

Figure 6. Stress and strain distributions across the cross-section of a bent sheet. (Asnafi 2000)

The local stress, and thus strain, can be calculated as a function of the bending moment. According to Vorkov et al. (2017), the local bending moment M at a certain point can be expressed as:

$$M = \sigma^* b t^2, \tag{13}$$

where σ^* is the local unit moment at said point, b the sheet width and t the sheet thickness. According to Aerens & Masselis (2000, see Vorkov et al. 2017), the unit moment can be approximated by:

$$\sigma^* = \left(\frac{2}{\sqrt{3}}\right)^{n+1} \frac{K}{2(n+2)} (\varepsilon_b + \varepsilon_d)^n \tag{14}$$

Where $$\varepsilon_d = \varepsilon_0 (1 + \frac{n}{2})^{1/n}, \tag{15}$$

ε_b is the strain on the outer surface,

n and K are material characteristics and

ε_0 is the initial strain, according to the Swift law: $\sigma = K(\varepsilon + \varepsilon_0)^n$.

If the initial strain is assumed $\varepsilon_0 = 0$, the Swift law is then equal to Hollomon's equation $\sigma = K\varepsilon^n$ and Equation (14) becomes:

$$\sigma^* = \left(\frac{2}{\sqrt{3}}\right)^{n+1} \frac{K\varepsilon_b{}^n}{2(n+2)}\ , \tag{16}$$

which, when substituted into Equation (13), expresses the relationship between the local bending moment and strain on the outer surface:

$$M_A = \left(\frac{2}{\sqrt{3}}\right)^{n+1} \frac{bt^2 K\varepsilon_b{}^n}{2(n+2)} \tag{17}$$

Based on Equation (17), the strain on the outer surface can be calculated as a function of the bending moment if the sheet dimensions and work hardening behaviour of the material are known. Figure 7 shows calculated approximate strain distributions for given moment distributions along the bend. It is evident that the shape of the strain distribution is majorly affected by the strain hardening exponent n, as well as the multi-breakage effect. Increase in the strain hardening exponent n produces wider strain distributions, as does the contact point shift in 4-point bending when using large radius punches.

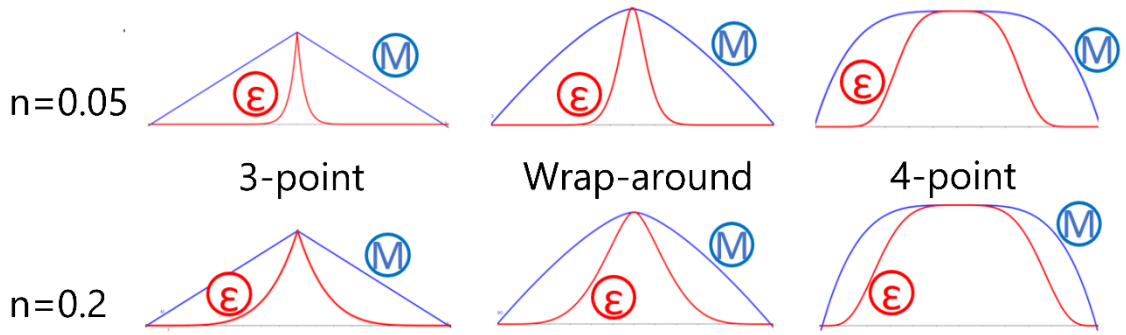

Figure 7. Approximate strain distributions calculated for different moment distributions based on n=0.05 and n=0.2, according to Hollomon's equation.

Another way to express strain in bending is as a function of the sheet curvature. According to Vorkov et al. (2017) and Troive (2017), and assuming the neutral axis is fixed at the middle of the cross-section, the bending strain at the outer surface ε_b can be expressed as:

$$\varepsilon_b = \frac{t}{2R_n}, \tag{18}$$

where t is the sheet thickness and R_n is the curvature radius of the neutral axis. According to Wang et al. (1993) and Asnafi (2000), Equation (18) describes the engineering strain on the outer surface, while the true bending strain is expressed as:

$$\varepsilon_x = \ln\left(1 + \frac{y}{R_n}\right), \tag{19}$$

where y is the distance from the neutral axis.

According to Lange (1985, p. 19.18), the curvature of the sheet is mostly independent of the punch radius during the three-point bending phase, and only starts to be affected by it when the inner radius becomes equal to the punch radius. As expressed in Equations (18) and (19), the strain on the outer surface depends on the curvature of the sheet, meaning that that the strain can also be expected to be unaffected by the punch radius from the beginning of bending until wrap-around. If the sheet does not separate from the punch after the wrap-around point and the inner bend radius stays equal to the punch radius, the maximum strains on the outer surface will stagnate. On the other hand, if multi-breakage happens and the inner bend radius becomes smaller than the punch radius, the maximum strains will keep increasing.

2.7 Bending force

Bending force, F_b, in thesis refers to the vertical force that is applied to the sheet by the punch, as illustrated in Figure 8.

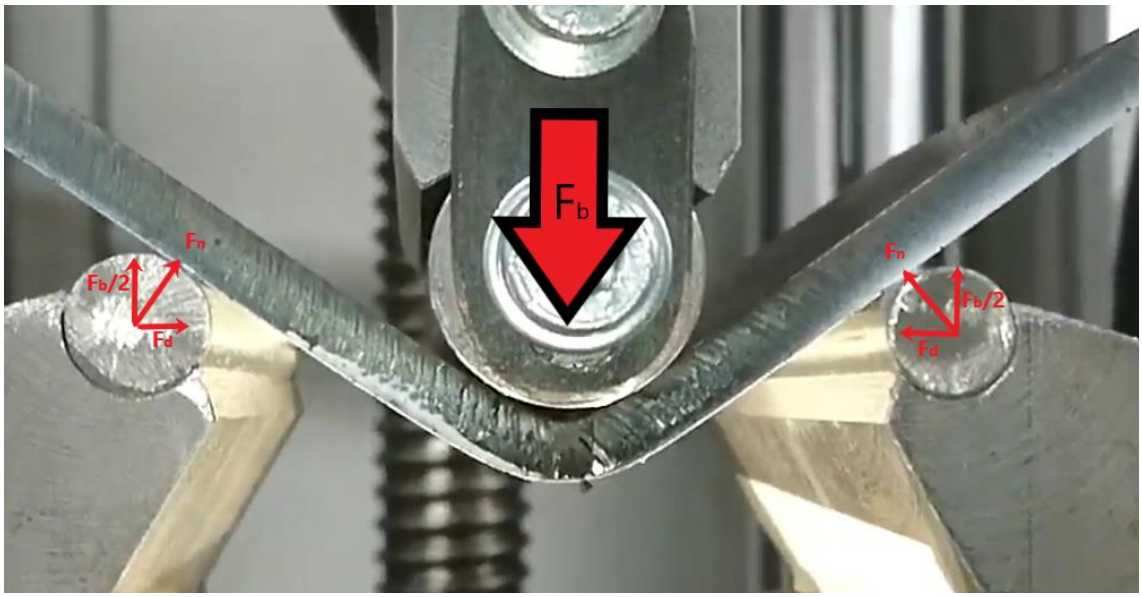

Figure 8. Bending force in air bending.

As bending tools and press brakes have limits for maximum loads, estimations for the required bending forces are necessary. For most cases, a rough estimation of the peak force is sufficient for the purpose, and the simplicity of the equation is beneficial for quick calculation in the workshop.

A commonly used equation for the peak bending force is as follows:

$$F = C * \frac{R_m b t^2}{W}, \tag{20}$$

where R_m is the ultimate tensile strength, b the bend length, t the sheet thickness, W the die width, and C a constant (1.6 – 1.8 for tempered and ultra-high strength steels, 1.2 – 1.5 for regular structural steels, according to Ruukki (2014)).

A variant of the common equation is presented in SSAB (2015) which takes punch and die shoulder radii into account:

$$F = \frac{R_m b t^2}{W - R_d - R_p}\,, \tag{21}$$

where R_d is the die shoulder radius and R_p the punch radius. According to Dannenmann (1974, as cited in Lange 1985, p. 19.22), the punch radius can be omitted from bending force calculations if the lower tool width is at least 5-8 times the punch radius.

While Equations (20) and (21) are useful in estimating the peak value of the bending force, it may sometimes be useful to be able to approximate the development of the bending force throughout the bending process. Vorkov et al. (2017) presented such an approximation. This approximation is based on the circular model and assumes the neutral axis is fixed at the middle of the cross-section throughout the bending process. Strain hardening behaviour is also assumed to follow Swift's law. According to Vorkov et al., the bending force F_b can be expressed as:

$$F_b = 2F_n \cos\theta\,(1 + \mu \tan\theta)\,, \tag{22}$$

where F_n is the normal force between the die and the sheet, θ is the half of the bending angle α and μ is the friction coefficient (Figure 9). The normal force F_n is then further defined as:

$$F_n = \frac{\sigma_A^* b t^2}{l_d + \frac{\mu t}{2}}\,, \tag{23}$$

where σ^*_A is the unit moment under the punch at point A, b the sheet width, t the sheet thickness, and l_d is the length of the moment arm, which is determined as:

$$l_d = \frac{w}{2\cos\theta} - \tan\theta\left(R_d + \frac{t}{2} + R_A\right), \tag{24}$$

where w is the die width, R_d is the die shoulder radius and R_A is the curvature radius of the neutral axis at point A, which is assumed to be fixed at the middle of the cross-section troughout the bending process, thus:

$$R_A = R_p + \frac{t}{2}\,, \tag{25}$$

where R_p is the punch radius. The unit moment σ^*_A was approximated according to Equation (14), which, assuming an initial strain of $\varepsilon_0=0$, becomes Equation (16). Inserting Equation (18) into Equation (16) gives:

$$\sigma_A^* = \frac{\left(\frac{2}{\sqrt{3}}\right)^{n+1} K\left(\frac{t}{2R_A}\right)^n}{2(n+2)} = \frac{\left(\frac{2}{\sqrt{3}}\right)^{n+1} K\left(\frac{t}{2R_p+t}\right)^n}{2(n+2)}, \quad (26)$$

where K and n are material characteristics for work hardening, according to Hollomon's equation $\sigma=K\varepsilon^n$. After substituting Equations (24), (25) and (26) into Equation (23), the normal force F_n is found as:

$$F_n = \frac{\left(\frac{2}{\sqrt{3}}\right)^{n+1} \frac{Kbt^2}{2(n+2)} \left(\frac{t}{2R_p+t}\right)^n}{\frac{w}{2\cos\theta} - \tan\theta\left(R_d+R_p+t\right) + \frac{\mu t}{2}} \quad (27)$$

The bending force F_b can finally be determined by inserting Equation (27) into Equation (22):

$$F_b = 2 * \frac{\left(\frac{2}{\sqrt{3}}\right)^{n+1} \frac{Kbt^2}{2(n+2)} \left(\frac{t}{2R_p+t}\right)^n}{\frac{w}{2\cos\theta} - \tan\theta\left(R_d+R_p+t\right) + \frac{\mu t}{2}} * \cos\theta\,(1+\mu\tan\theta) \quad (28)$$

$$= \frac{\left(\frac{2}{\sqrt{3}}\right)^{n+1} \frac{2Kbt^2}{n+2} \left(\frac{t}{2R_p+t}\right)^n (1+\mu\,\tan\theta)}{w - 2\sin\theta\left(R_d+R_p+t\right) + \mu t\cos\theta}$$

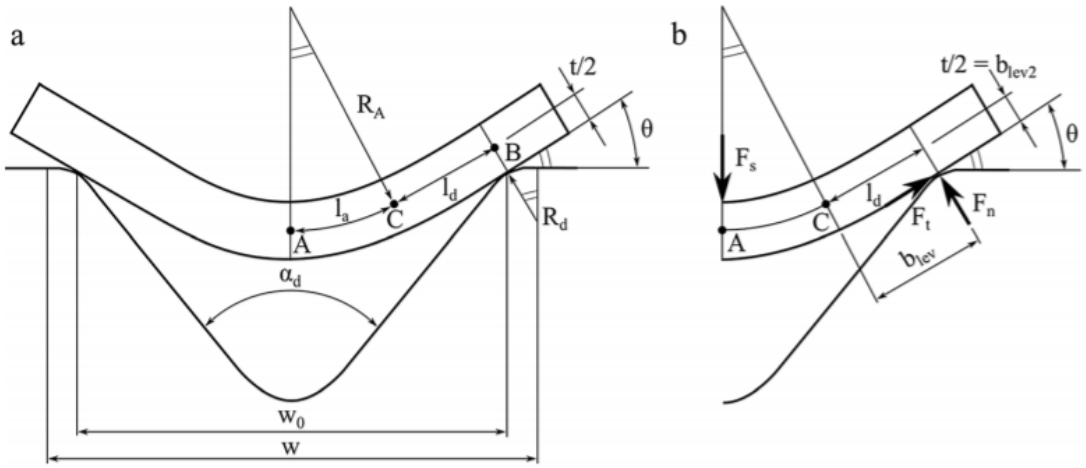

Figure 9. Parameters used for bending force approximation in Vorkov et al. (2017).

2.8 Fracture development

According to a model presented by Dao & Li (2001), fracturing in sheet metal bending usually develops in association with intensifying strain localisation. Fracture initiation is

started by orange peeling and gradually increasing surface waviness, which leads to shear band initiation at the wave bottoms. The development and propagation of these shear bands will ultimately result in fracture when the shear bands interact with second-phase particles or intersect with each other. Shear bands can also initiate and develop under surface, from second-phase particles and grain boundary precipitates.

In simulations on an aluminium alloy 6111-T4 done by Dao & Li, highly non-uniform deformation and early stage shear bands were observed with maximum principle strains of around 20%. Macroscopic shear bands were identified at 40-60%, and fully developed intense shear bands at 60-100% maximum strains. The development and intensity of strain localisation were found to depend strongly on the strain hardening properties and texture of the material. Decreased strain hardening, crystallographic rolling texture and constituent particles, especially near the outer surface, were correlated with increased surface roughening and strain localisation intensity. Although the simulations and experiments were conducted on aluminium, the fracture initiation through strain localisation, surface roughening and shear banding is a characteristic of polycrystalline materials, including steel. (Dao & Li 2001)

Lievers et al. (2003) showed by using a kinematic hardening version of the Gurson-Tvergaard-Needleman model (GTN), that the development of shear bands is affected by the isotropic/kinematic hardening parameter *b*. Shear bands were found to develop at much smaller bend angles in kinematic materials (b=0) than in isotropic ones (b=1), which can be seen as a drop in bending force at an earlier state. Inhomogeneous material behaviour, caused by either geometric or material imperfections, was also found to contribute to strain localisation.

Kaupper & Merklein (2013) generalised the failure stages and defect types for high-strength steel bending (Figure 10). In the first stage, surface waviness and geometric imperfection can be observed. In the second stage, some of the wave bottoms expand into ductile cuts, which in turn initiate fine shear cracks from their bottoms in the third stage. In the last stage, the instable growth and propagation of cracks leads to fracture in the major damaged zone at the center of the bend.

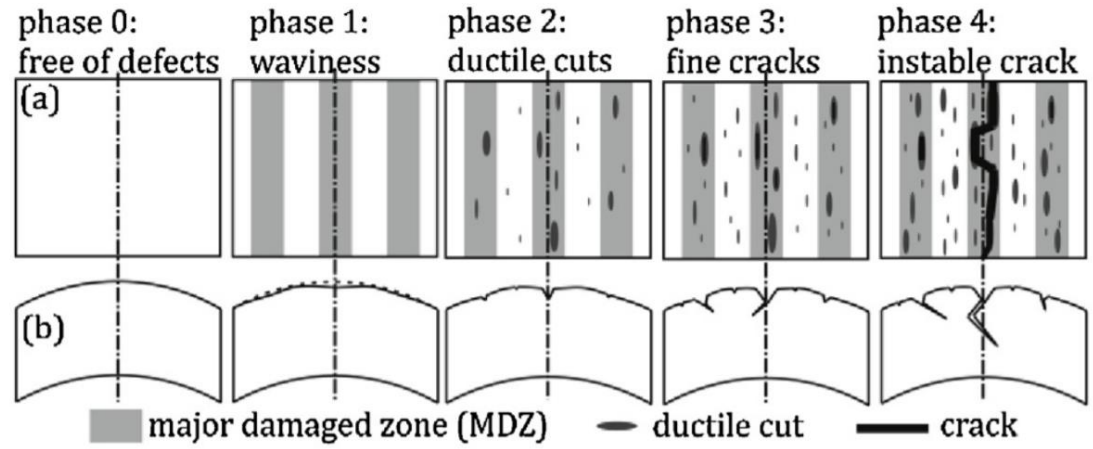

Figure 10. Failure stages and defect types for high-strength steel bending. (Kaupper & Merklein (2013)

Kaupper & Merklein (2013) also introduced a model for a "deformation path" of a specimen based on homogeneity and localisation of deformation, in which a linear growth represents homogenous deformation, a convex course represents localisation and a concave course represents stagnation in defect growth (Figure 11). At each of the first three (stable) stages, it is possible for a deformation path to either stagnate or to continue to the next failure stage, depending on the material and bending parameters.

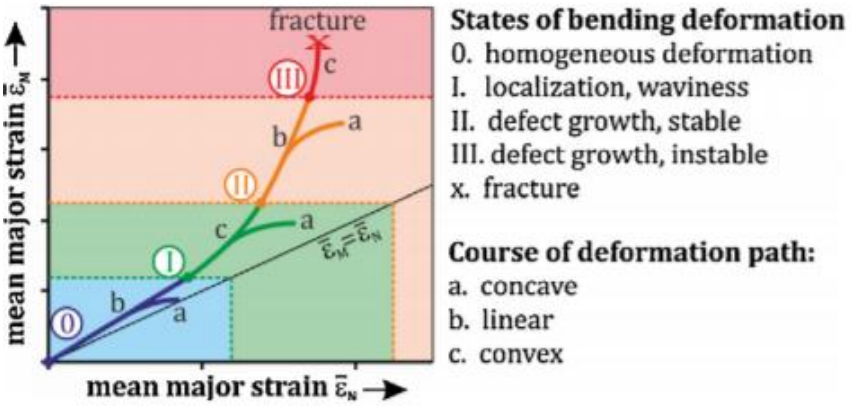

Figure 11. A generalised model for characteristic deformation paths in bending. (Kaupper & Merklein 2013)

Obviously, the exact proportions and locations of the failure stages on the deformation path are material specific. However, as an example, Kaupper & Merklein (2013) detected surface waviness, stable defect growth and instable defect growth at strains around 0.2,

0.4 and 0.7, respectively, for the materials used (HCT780X and HCT780C+ZE). As another example, Arola et al. (2015b) deemed surface waviness and groove formation to start at major strains of around 0.22 – 0.25 and fracturing at around 0.46 – 0.52 strain for a 960 MPa grade steel.

2.9 Bendability

Bendability of a material is generally expressed as the smallest radius that the material can be bent to, without developing visible cracks on the outer surface. Bendability in general is affected by numerous material properties, including strain hardening, second-phase particles, grain-boundary precipitates and surface roughening in deformation. (Datsko & Yang 1960; Dao & Li 2001)

2.9.1 n- and m- values

The strain distribution in bending is determined by the *n*-value (strain-hardening coefficient) and the *m*-value (strain rate sensitivity). The *n*- and *m*-values are determined by the effects of strain and strain rate on the flow stress. The higher the *n*-value, the more the flow stress increases with a given amount of strain. Similarly, higher *m*-values indicate higher flow stresses with higher strain rates. As regions with high flow stress tend to resist further deformation, higher *n*-values and *m*-values mean that the deformation is distributed to regions of lower strain and lower strain rates, respectfully, thus evening the strain distribution. In other words, higher *n*- and *m*- values indicate resistance to strain localisation, and hence better bendability. (Taylor 1988)

According to Taylor (1988), the true stress relationship to strain and strain rate can be expressed as:

$$\sigma = k\varepsilon^n \dot{\varepsilon}^m \tag{29}$$

For materials with positive strain rate sensitivity (*m*-values), such as most steels, higher strain rates lead to higher stresses. Thus, with these kinds of materials, it could be expected that higher bending speeds would lead to higher bending forces. (Taylor 1988)

2.9.2 Area reduction in uniaxial tension

Datsko & Yang (1960) found a correlation between the bendability of materials and their percentage area reduction A_r in uniaxial tension. When the neutral fiber is assumed to be at the center of the sheet and when $A_r \leq 20\%$, the relation between the inner bend radius to sheet thickness ratio R_i/t and the area reduction in uniaxial tension can be expressed as:

$$\frac{R_i}{t} = \frac{50}{A_r} - 1 \tag{30}$$

For Ar > 20%, (when the neutral fiber is assumed to have displaced from center of the sheet), the relationship is as follows:

$$\frac{R_i}{t} = \frac{(100-A_r)^2}{200A_r - A_r^2} \tag{31}$$

2.9.3 Rolling direction

Rolling direction affects bendability significantly. Ductility is generally lower when the bending axis is parallel to the rolling direction, and material failure at is more likely in this direction when using small bending radii. This is why the minimum bending radius tends to be generally around 0.5t higher in this direction than in the perpendicular direction. In a related study by Arola et al. (2019) the required bending forces were also found to be greater in the parallel (longitudinal) direction as well as the peak strains at the outer surface. (Datsko & Yang 1960; Lange 1985, p.19.30-34)

2.10 Multi-breakage

Large radius punches are commonly used in air bending of high-strength steels because of their limited formability. Although attractive for reducing the maximum strains on the specimen surface, the usage of large punch radii introduces another problem in the form of the multi-breakage phenomenon. Multi-breakage happens when the inner radius of the bent sheet becomes smaller than the punch radius, and consequently the sheet loses contact to the punch nose (Figure 12), leading to two points of contact at the sides of the nose and thus a change from three-point to four-point bending (Figure 5). Vorkov et al. (2017) consider large radius bending to be in effect when $R_p/W > 0.25$ or when $R_p > 1t$. In a previous study by Väisänen et al. (2009), however, multi-breakage was observed with R_p/W ratios as small as 6/45 (0.13) and punch radii as small as 1t.

Figure 12. Multi-breakage in large radius bending.

The effects of large radius bending become magnified as the R_p /t ratio increases further. One important observation by Vorkov et al. (2017) is that the shift of the contact points is not affected by material parameters. The positions of the contact points are defined only by the tool geometry in relation to the sheet thickness. Similar observations were made by Väisänen et al. (2009), as no significant difference in this behaviour was found between ultra-high-strength and regular high-strength steels.

Multi-breakage is problematical for the bending of ultra-high strength steels of 900 MPa grade and above, as their minimum bend radii tend to be in the order of 3-4t. Multi-breakage affects the bending process in many aspects and understanding the phenomenon is essential for the effectiveness of large radius bending. In multi-breakage, the contact points between the punch and the sheet shift towards the die shoulders, thus shortening the moment arms. Consequently, the required bending force is increased. Calculation of the required punch displacement and springback are also made more complicated, which may lead to overbending of the sheet. Furthermore, compared to the wrap-around model, a bend with multi-breakage will require longer initial length from the blank for a given part, i.e. the bend allowance is decreased. The decrease of the radius of curvature of the sheet below the punch radius will also lead to higher strains, which may lead to fractures on the outer sheet surface if multi-breakage is not taken into account in tool selection. (De Vin 2000; Vorkov et al. 2017)

2.11 Edge deformation

As described earlier, the outer and inner parts of the cross-section are under tensile and compressive circumferential stresses, respectively. Because of the Poisson effect, the outer part of the cross-section tends to contract, and the inner part tends to expand in the bending axis direction. This leads to anticlastic deformation, characteristic to all bending, in which the edges of the plate bend away from the punch. This in turn leads to loss of contact with the punch near the edges.

Anticlastic deformation is strongly dependent on the width of the plate b. The shape of the surface and the amount of the anticlastic deformation depend on the ratio b^2/R_nt. For narrow beams, where $b^2/R_nt \leq 1$, the curvature of the surface follows roughly the arc of a circle of radius R_n/v, where v is the Poisson's ratio. For wider plates, where $b^2/R_nt > 20$, the anticlastic deformation is mostly concentrated away from the center of the plate, and as b^2/R_nt increases, the deformation concentrates more and more at the edges. (Horrocks & Johnson 1967)

3 EXPERIMENTS

In this chapter, the experimental setup is presented along with the variable and constant parameters. Specimen preparation and DIC measurement settings are also discussed.

3.1 Test setup

A test setup similar to Arola et al. (2019) was used. The tests were conducted in room temperature using a Zwick 100kN universal tensile testing machine equipped with purpose-built bending tools with adjustable die width and compatibility with both the testing machine and the DIC strain measurement rig. Bending force and punch displacement were measured by the testing machine and strains at the outer surface were measured with a Lavision Strainmaster DIC-system.

The DIC-cameras were supported by tripods on the floor and the camera positioning, along with the rest of the test setup, is illustrated in Figure 13a. Figure 13b further illustrates the DIC-camera setup, where the openings in the lower tool allow a line of sight from the cameras to the specimen. It should be noted that the punch is stationary in this setup to keep the measurement area in focus throughout the tests. The required punch stroke for the bending is produced with the lower tool moving upwards.

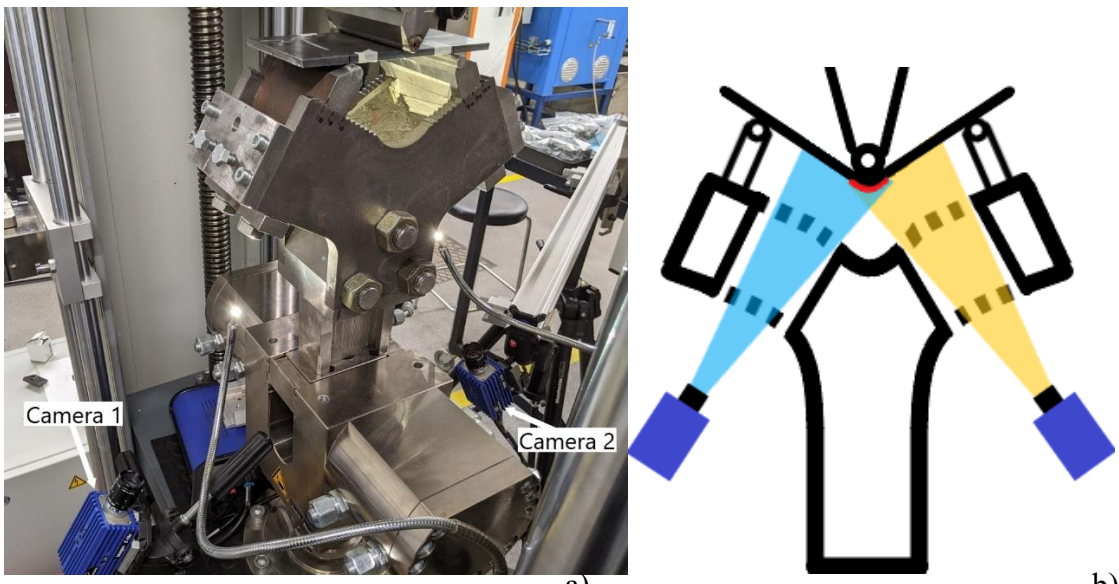

a) b)

Figure 13. a) Photo and b) scheme of the bending test setup. Cameras in blue, the measured area of the bent sheet marked in red.

The relevant dimensions and parameters of the setup are displayed in Figure 14. The bending angle α was calculated according to the Formula (9) presented by Troive (2017), based on the punch displacement data and the geometry of the setup.

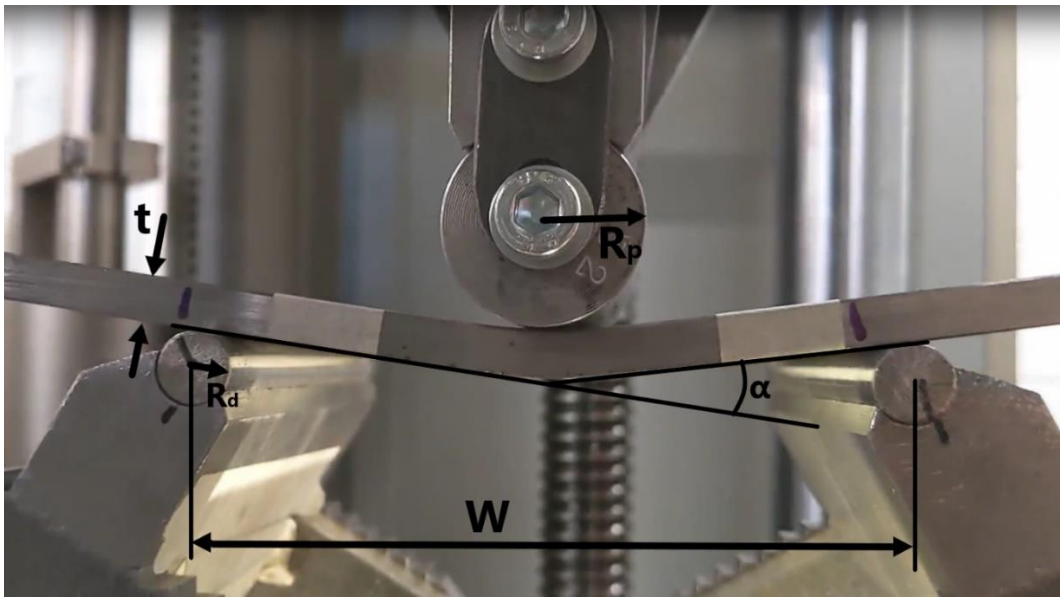

Figure 14. Dimensions of the bending test setup.

3.2 Parameter variations and test matrices

The tool and sheet parameters were varied in the experiments in order to measure their effect on the bending forces and strains on the outer surface. All the relevant parameters and their used values are listed in Table 1. A complete list of the tested parameter combinations, along with their respective test numbers, is presented in Appendix 1.

For facilitating the investigation of the effects of the individual parameters, the tests were reorganised into 14 test matrices. In matrices 1 – 6 (Figure 15), sheet thickness and the R/t ratio were varied, while the material grade, rolling direction, die width and punch speed were constant. In matrices 7 – 12 (Figure 16), material grade and the bending orientation were varied while other parameters were kept constant. In matrix 13 (Figure 17a), die width and bending orientation were varied. Finally, in matrix 14 (Figure 17b) the punch speed and material grade were varied, while other parameters stayed unchanged.

Table 1. Parameters in the test setup.

Parameter	**Used values**
Punch radius, R_p	1t, 2t, 4t (= 4, 6, 8, 12, 16, 24, 32 mm)
Die width, W	70 mm, 90 mm, 110 mm
Die radius, R_d	6 mm
Punch speed, V_p	1 mm/s, 10 mm/s
Material grade	S700, S900, S1100
Sheet thickness, t	4 mm, 6 mm, 8 mm
Bend length (specimen width), b	80 mm, 100 mm
Bending orientation	0° (RD), 90° (TD) (bend axis to rolling direction)
Bend angle, α	0° – 90°

Effect of R/t -ratio and sheet thickness:

Constants: Material, RD/TD, W, Vp

Matrix1

W=110	All RD	S700
	R/t=1	R/t=2
T4	02b	09
T6	06b	26
T8	22b	60

Matrix2

W=110	All TD	S700
	R/t=1	R/t=2
T4	03b	11
T6	08b	27
T8	24b	62

Matrix3

W=110	All RD	S900
	R/t=2	R/t=4
T4	14	52
T6	29	72
T8	63	82b

Matrix4

W=110	All TD	S900
	R/t=2	R/t=4
T4	16	54
T6	32	74
T8	66	80b

Matrix5

W=110	All RD	S1100
	R/t=2	R/t=4
T4	18	56
T6	33	75
T8	67	84

Matrix6

W=110	All TD	S1100
	R/t=2	R/t=4
T4	20	58
T6	35	78
T8	70	86

Figure 15. Test matrices for testing the effects of R/t ratio and sheet thickness.

Effect of material (and rolling direction):						
Constants: t, R/t, W, Vp						
Matrix7				Matrix8		
W=110	R/t=2	R8 T4		W=110	R/t=2	R12 T6
	RD	TD			RD	TD
S700	09	11		S700	26	27
S900	14	16		S900	29	32
S1100	18	20		S1100	33	35
Matrix9				Matrix10		
W=110	R/t=2	R16 T8		W=110	R/t=4	R16 T4
	RD	TD			RD	TD
S700	60	62				
S900	63	66		S900	52	54
S1100	67	70		S1100	56	58
Matrix11				Matrix12		
W=110	R/t=4	R24 T6		W=110	R/t=4	R32 T8
	RD	TD			RD	TD
S900	72	74		S900	82b	80b
S1100	75	78		S1100	84	86

Figure 16. Test matrices for testing the effects of material grade and rolling direction.

Effect of die width (and rolling direction):		
Constants: material, t, R/t, Vp		
Matrix13		
S900	R/t=2	R12 T6
	RD	TD
W=110	29	32
W=90	42	44
W=70	38	40

a)

Effect of punch speed (and material):		
Constants: material, W, t, R/t, RD/TD		
Matrix14		
S900	R/t=2	R12 T6
All TD	Vp=1	Vp=10
S700	27	46b
S900	32	48
S1100	35	49/50

b)

Figure 17. Test matrices for testing the effects of a) die width and b) punch speed.

3.3 Specimen preparation

Three different materials with sheet thicknesses t of 4, 6, and 8 mm were tested. The specimens were cut from larger plates into rectangles with a width b of either 100 mm or 80 mm, depending on the expected bending force requirements for each parameter combination. 80 mm width was only used for tests that could not be conducted with 100 mm widths due to the maximum force limit of the machine. Even with the narrower specimens, the b/t ratio remains over 10 and the b^2/R_nt ratio over 22, ensuring that plane strain conditions apply, and that the results are unaffected by edge deformation.

Each test combination was repeated twice in the rolling direction and transverse direction. For clarification, the bend direction is considered longitudinal (RD) when the bend axis is parallel to the rolling direction and transverse (TD) when the bend axis is perpendicular to the rolling direction as illustrated in Figure 18. The specimens were oriented in such a

way that the outer bend surface always corresponded to the underside of the hot-rolled coil.

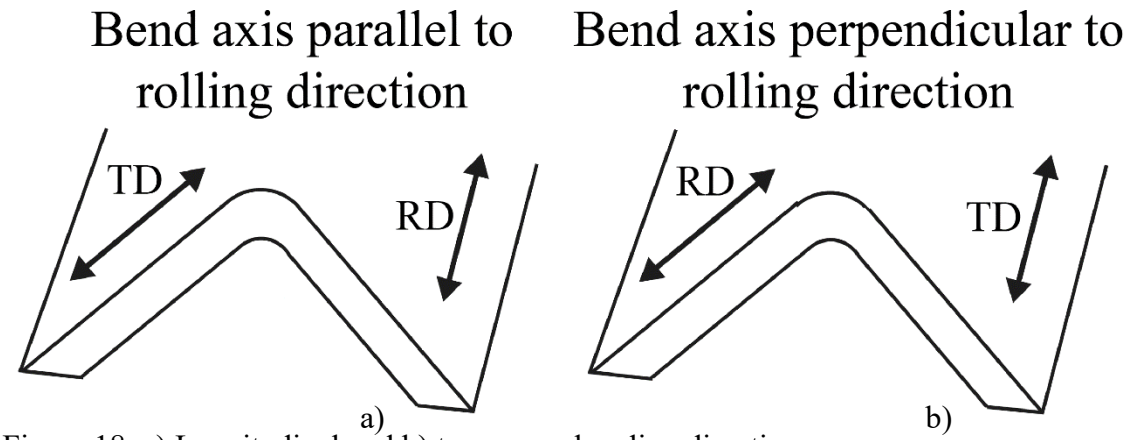

Figure 18. a) Longitudinal and b) transverse bending directions.

3.4 DIC measurement

Digital image correlation (DIC) is an optical measurement technique that is used for measuring displacement and strain fields on a surface of a specimen among other things. The operating principle of DIC measurement is essentially based on analysing image sequences taken of the loaded specimen throughout the test. The DIC software then compares the images in the sequence to a reference image of the specimen in an unloaded state. Based on this comparison, the software can then calculate displacements and strains at each point in time for a set amount of points on the specimen surface. Stereoscopic vision is necessary for accurate measurement of curved surfaces, which is why two cameras must be used for DIC measurement in bending tests.

To enable unambiguous identification and tracking of the points on the measured surface and thus, accurate calculation of displacements and strain, there must be a sufficient amount of distinctive, high-contrast features on the surface. Additionally, the surface should have a matte surface to reduce glare caused by reflections of the light source. Usually, the surface of a metal specimen does not fulfil these conditions, so an artificial surface pattern must be applied. A common method for preparing the surface for DIC is applying a “speckle pattern” using spray paint.

3.4.1 Speckle pattern application for DIC measurement

Before applying the paint, the outer bend surfaces were cleaned with ethanol to remove any brittle scale and dirt that may prevent the paint from attaching properly to the underlying material and thus affect the measurements significantly. Then, a random speckle pattern was applied to the region of interest at the center of the specimens, using matte black and matte white spray paint (Figure 19). The quality of the speckle pattern is essential to the measuring accuracy of DIC, which is why special attention and effort was paid to the painting process to achieve the best possible speckle pattern quality. A rule of thumb, presented by Jones & Iadicola (2018), states that a good pattern should have at least three features in each facet, as in the features should be under third of the facet size, but the features should also not be below 3 pixels in size. As the used facet size in these experiments is 15x15 pixels, and the image scale is approximately 20 pixels/mm, the optimal speckle size should be 3 – 5 pixels, or around 0.15 – 0.25 mm.

A near-optimal pattern was achieved for some specimens, but despite best efforts, some oversized speckles over 1 mm in size were obtained in almost every specimen. These lead to loss of information in these areas and can be observed as small holes in the calculated strain maps (Figure 20). To avoid the paint drying too much and peeling during the test, the specimens were tested within a few hours of painting.

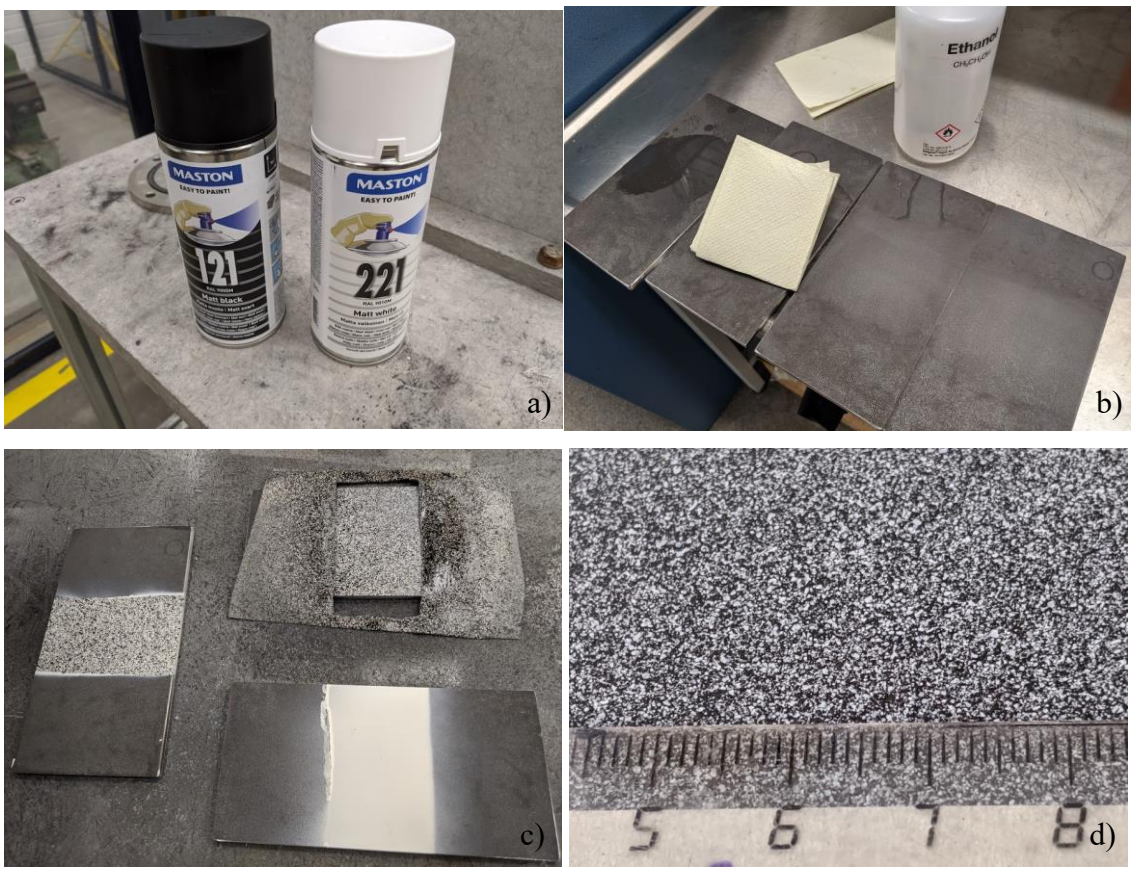

Figure 19. The speckle pattern application for DIC measurement. a) Black and white matte spray paints. b) Cleaning with ethanol before painting. c) Painting a speckle pattern with black speckles on white backgroung. d) Good quality speckle pattern.

3.4.2 Settings and parameters used in DIC measurement

For the DIC measurement, an imaging frequency of 2 Hz was used when the punch velocity was 1 mm/s. For the tests with a 10 mm/s punch speed, the highest available frequency of 10 Hz was used. For the DIC strain calculations, a facet size of 15 pixels and a step size of 5 pixels were used, corresponding to a strain gauge of approximately 0.25 mm. An outlier filter was applied for vectors deviating over 4x from the average in an 11x11 pixel area. Additionally, a second order polynomial smoothing filter was applied over a 5x5 pixel area.

The calculated peak strains and strain distributions were extracted from three lines across the bend, close to the center of the surface, with a 10 mm distance between each line, as illustrated in Figure 20. The amount of lines and their positioning were chosen for achieving a decently accurate representation of the strains in the central area of the bend, where plane-strain conditions apply. With a single line, the obtained peak strain and strain

distribution would be affected too much by local deviations and measurement noise. With three lines, the effect is reduced, and the deviations can be seen from the obtained charts.

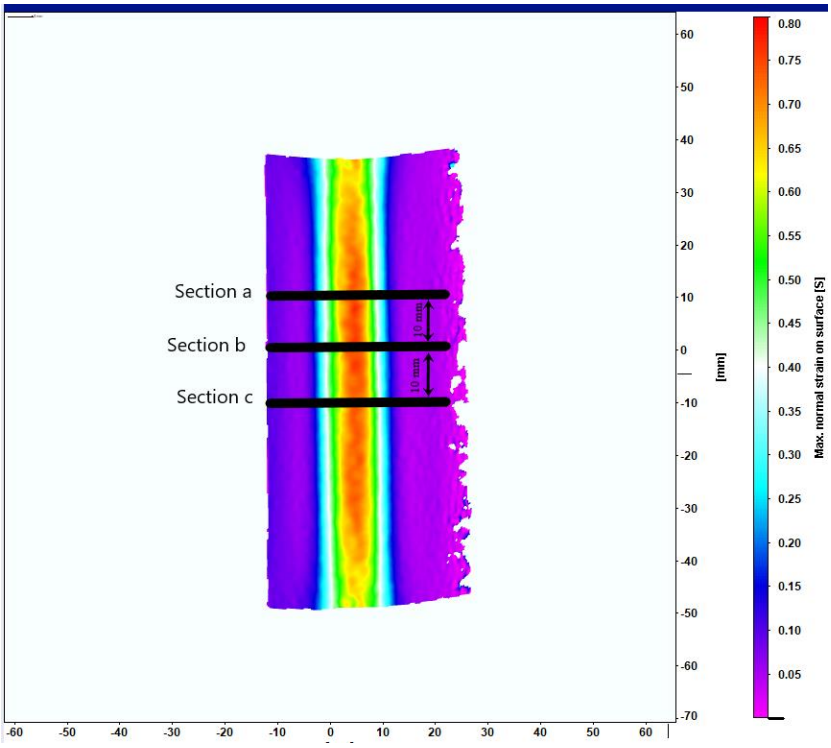

Figure 20. A strain map measured by DIC and the placement of the three section lines.

4 RESULTS AND DISCUSSION

In this chapter, the test results are presented along with discussion and possible explanations for the observations made. The chapter is divided into sections, where the effects of the parameters are presented and discussed, one by one.

The measurement data are presented in charts similar to Figures 21 and 22. Figure 21 illustrates the measured strain distributions. The measured data points from the three sections (Figure 20) were combined into one chart. The maximum values of each section were taken from each measurement. The averages of these values were then plotted against the bending angle, as seen in Figure 22b. A calculated strain distribution based on the circular model was included in each strain distribution chart for comparison.

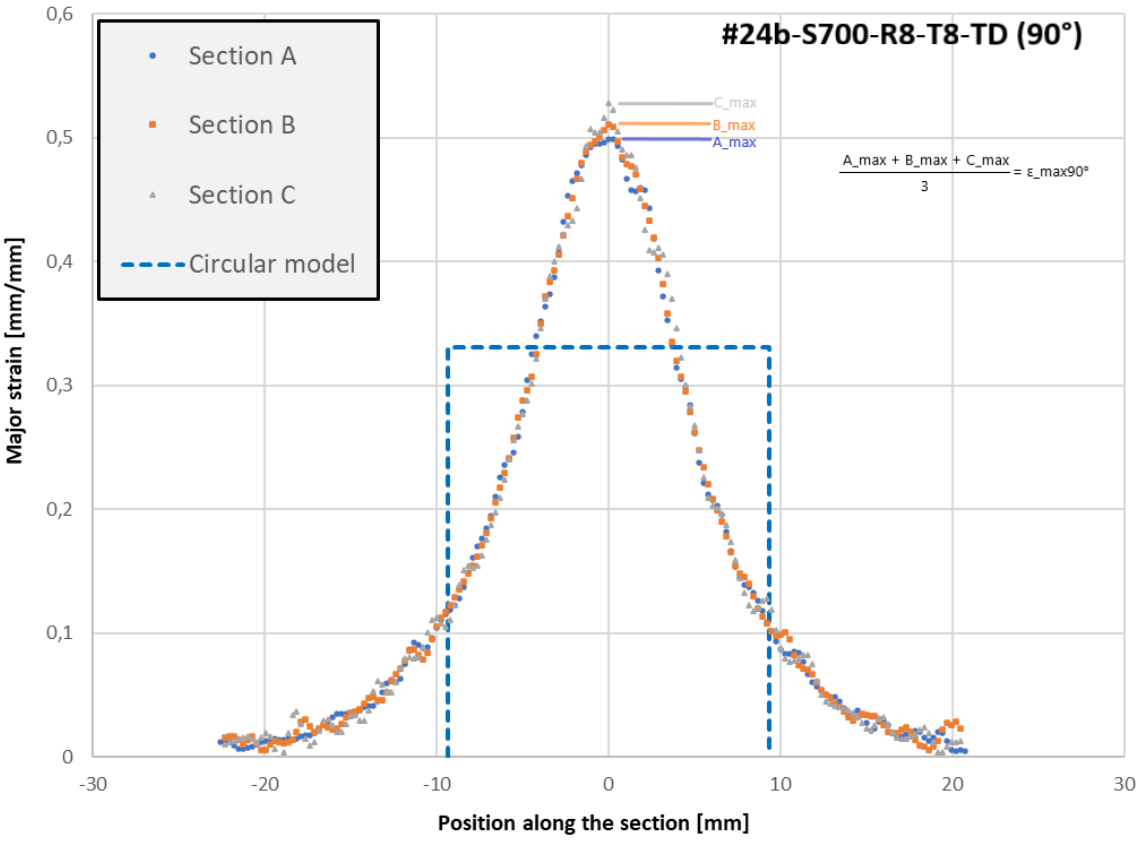

Figure 21. Strain distribution of test #24b at 90° bending angle.

The measured bending forces are also presented as a function of the bending angle, as illustrated in Figure 22a. To account for variances in the specimen widths, the bending forces are expressed as force per unit width.

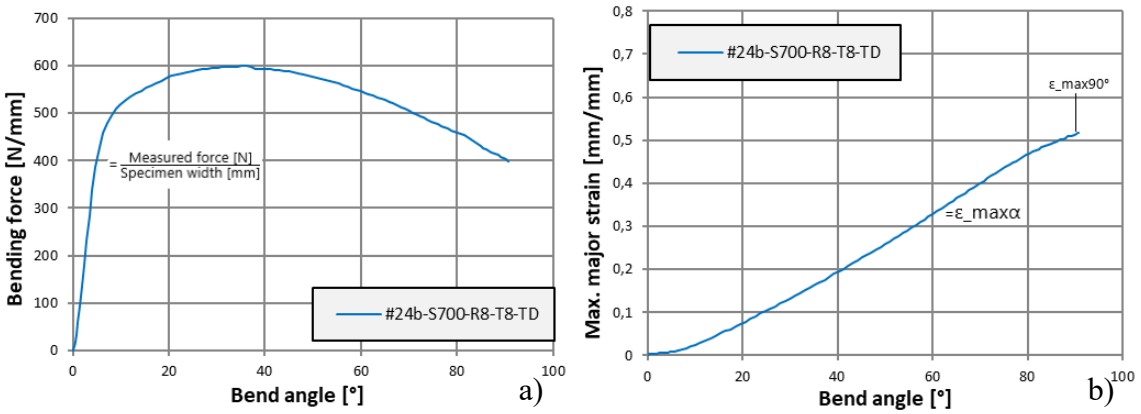

Figure 22. a) Bending force and b) maximum strain of test #24b, as functions of the bending angle.

4.1 R/t ratio

In this section, the measured effects of the punch radius relative to the sheet thickness (R/t ratio) are discussed. Two R/t ratios were used for each material. For S700, the tested ratios were R/t = 1 and R/t = 2. For S900 and S1100, ratios of R/t = 2 and R/t = 4 were tested. Further on, these ratios will be referred to as R1t, R2t and R4t.

4.1.1 Effect of R/t ratio on bending force

The R/t ratio had very minimal effect on the bending forces of the 4 mm sheets. The force curves were almost identical regardless of what punch was used (R1t, R2t or R4t). The only noticeable difference was the fracturing of some S1100 samples with R2t punches but not with R4t. (Figures 23a, 24a, 25a)

6 mm sheets were affected more by the R/t ratio. Increase in punch radius from R1t to R2t did not affect the peak force but increased the force by a few percentages towards the end of the test (Figure 23a). Doubling the punch radius from R2t to R4t did have a greater effect on the bending force curve. The curves were identical until about 30 – 35°, after which the force of the R4t punch tests started to increase again, while the force in tests with R2t punches decreased (Figure 24a, Figure 25a). Because of the second increase, the peak forces were around 6 – 8% higher when using R4t punches compared to R2t.

8 mm sheets were the most affected by the increase in punch radius. Increase from R1t to R2t did not increase the peak force, but it did make the force plateau for a duration of around 20° after the peak (Figure 23a). The switch from R2t to R4t punches had the

greatest impact, as can be seen from Figures 24a and 25a. With the R4t punches, the bending force increased almost linearly until the peak at around 75 – 80°, which was 20 – 29% higher than the peak force with the R2t punches.

According to Dannenmann (1974, as cited in Lange 1985, p. 19.22), the punch radius does not affect the peak force if the die width is at least 5 – 8 times the punch radius. This seems to apply to these results as well. Looking at Figures 23 – 25, the largest punch radius that does not affect the peak force is R_p = 16 mm, which is just under one seventh of the used die width.

4.1.2 Effect of R/t ratio on strain

The R/t ratio had a crucial effect on the measured strains at the outside surface. Punches with smaller R/t ratios resulted in narrower strain distributions (Figures 40 – 45 in Appendix 2) with higher peak strains that kept growing until the end of the test (Figures 23b, 24b, 25b). These also resulted in fractures with the S1100 material.

Conversely, the punches with larger R/t ratios produced wider strain distributions with lower peak strains. After a certain point between 40 – 70° angle, the peak strain stopped increasing and the strain distribution would start to grow around 10 – 20 mm away from the center instead. The more even strain distribution resulted in 13 – 70% lower peak strains at 90°, or 52 % on average, and prevented fracturing in the S1100 material.

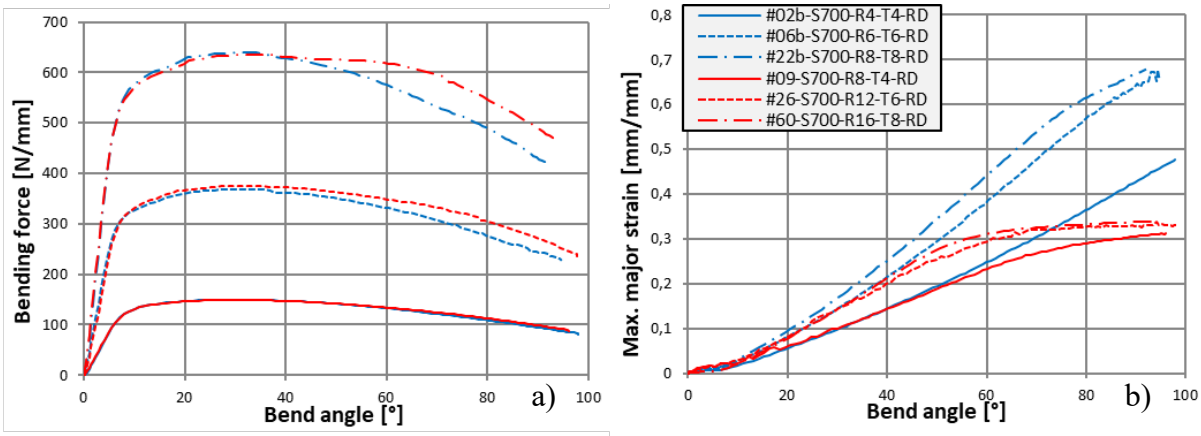

Figure 23. a) Bending force curve and b) maximum surface strain as a function of the bending angle. Material: S700, W = 110 mm, V_p = 1 mm/s, t = 4/6/8 mm, R_p = 1t / 2t, longitudinal direction.

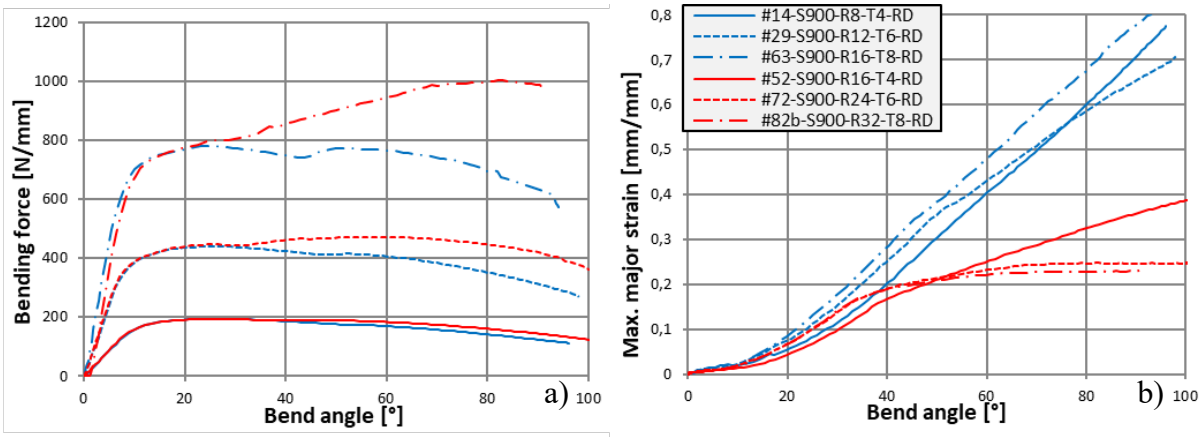

Figure 24. a) Bending force curve and b) maximum surface strain as a function of the bending angle. Material: S900, W = 110 mm, V_p = 1 mm/s, t = 4/6/8 mm, R_p = 2t / 4t, longitudinal direction.

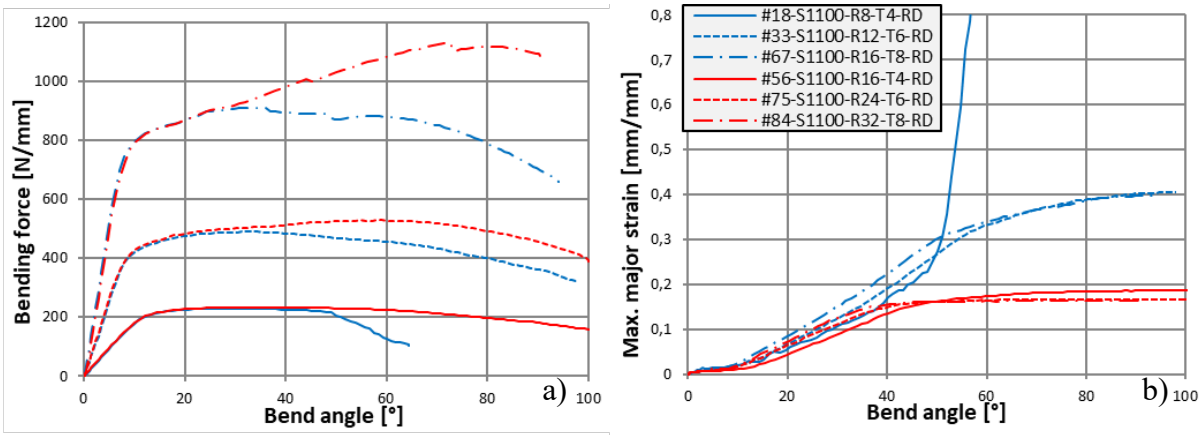

Figure 25. a) Bending force curve and b) maximum surface strain as a function of the bending angle. Material: S1100, W = 110 mm, V_p = 1 mm/s, t = 4/6/8 mm, R_p = 2t / 4t, longitudinal direction.

4.2 Sheet thickness

In this section, the measured effects of the sheet thickness are discussed. Three sheet thicknesses were tested for each material: 4 mm, 6 mm and 8 mm.

4.2.1 Effect of sheet thickness on bending force

The effect of the sheet thickness on bending force can be observed in Figures 23a, 24a and 25a. With R1t and R2t punches, the bending force scaled proportionally to the square of the sheet thickness. 8 mm sheets required 4.0 – 4.3 times the force of 4 mm sheets and 1.7 – 1.9 times the force of 6 mm sheets. Sheets of 6 mm thickness, in turn, required a force 2.1 – 2.6 times that of 4 mm sheets.

With R4t punches, the effect of sheet thickness on bending force was amplified by the secondary increases after the initial peak at around 25 – 30°. When using R4t punches, 8 mm sheets required 4.8 – 5.3 times the peak force of 4 mm sheets, and 2.0 – 2.1 times that of 6 mm sheets. Compared to the 4 mm sheets, the force required for 6 mm sheets increased by a factor of 2.3 – 2.5. This secondary increase in force is a result of the contact point shift during 4-point bending. As the contact point shift during bending is much greater with the larger punches and thicker sheets, the moment arm also decreases further, which leads to an increase in the required force at the later stages of bending.

4.2.2 Effect of sheet thickness on strain

The effect of the sheet thickness on the strain distributions can be observed in Figures 40 – 45 in Appendix 2 and the effect on maximum strain development can be seen in Figures 23b, 24b and 25b. 6 mm and 8 mm sheets showed similar strain distribution shapes and peak strain development throughout all the tests. When using R1t and R2t punches, 8 mm sheets showed 3 – 19% higher peak strains than 6 mm sheets, but with R4t punches, the peak strains were near identical. The strains in the 4mm sheets varied greatly relatively to the 6 mm and 8 mm sheets. With the S700 grade, the strains were significantly lower in 4 mm sheets than in the other thicknesses. However, with the S900 and S1100 grades, the 4 mm sheets had equal or slightly higher amount of strain compared to other thicknesses. The differing results in 4 mm sheets may be caused by differences in material properties between the different sheet thicknesses, but not enough data is available of the specific batches of materials used, so further research is necessary.

The strain distributions were naturally wider with the thicker sheets. Due to the limitations in the strain measuring setup, the observable area in the x-axis was too small to completely measure the strain distribution widths for all test. But from the available data, the strain distribution width seems to be directly proportional to the sheet thickness.

4.3 Steel grade

In this section, the measured effects of the steel grades are discussed. Three different grades were tested: S700, S900 and S1100. The relevant material parameters for each sheet thickness of each grade are listed in Table 2.

Table 2. Material parameters. Data was not available (N/A) for some parameters of some sheets.

Material	t (mm)	$R_{p0.2}$ (MPa)	R_m (MPa)	A_5 (%)	n	K (MPa)	Min. R_p	Min. W/t
S700MC	4	708 - 717	829 - 831	14 - 15	0.071	1078	1t	10
	6	726 - 735	838 - 848	15 - 16	0.070	1090	1t	10
	8	728 - 780	820 - 871	10 - 16	0.064	1073	1t	10
S900MC	4	N/A	N/A	N/A	N/A	N/A	3t	12
	6	978 - 986	1079 - 1095	4 - 10	0.049	1327	3t	12
	8	961 - 997	1080 - 1086	8 - 10	N/A	N/A	3t	12
S1100	4	1128 - 1130	1184 - 1195	11 - 13	N/A	N/A	3.5t	14
	6	1102 - 1118	1147 - 1170	12 - 13	0.046	1400	3.5t	14
	8	1126 - 1130	1153 - 1172	11 - 12	0.043	1391	4t	14

4.3.1 Effect of steel grade on bending force

As can be seen from Figures 29 – 34, the bending force curves were mostly of similar shapes for all materials. The only notable difference was the tendency of S900 to get a high second peak in the force curve, after around 45 – 50° with 6 mm and 8 mm sheet thicknesses. This second peak could also be seen, to some extent, in an 8 mm thick sheet of S1100.

When accounting for sheet thickness variance by dividing the force by the square of the sheet thickness, and averaging the results from longitudinal and transversal tests, the S1100 grade was found to increase the required force by 9 – 15% compared to S900 and 37 – 47% compared to S700. The S900 grade was found to require 23 – 32% higher force than S700. The results are presented in Table 3. The measured changes seemed to be within a couple of percentage points off the range of expected change based on the ultimate strengths of the materials presented in Table 4. Because of small sample size and

lack of tensile data from the materials used, no definite conclusions could be made on the accuracy of the ultimate tensile strength in bending force estimation.

Table 3. Effect of steel grade on the maximum bending force. Values without brackets are from tests with R2t punches. Values in brackets are from R4t tests.

Avg/t^2	**S1100/S900 (R4t)**	**S1100/S700**	**S900/S700**
T4	+12% (12%)	+47%	+32%
T6	+11% (9%)	+37%	+23%
T8	+15% (11%)	+44%	+25%

Table 4. Expected change in bending force based on the ultimate strengths of the materials.

R_m / R_m	**S1100/S900**	**S1100/S700**	**S900/S700**
T4	No data	42 – 44%	No data
T6	5 – 8%	35 – 40%	27 – 31%
T8	6 – 9%	32 – 43%	24 – 32%

4.3.2 Effect of steel grade on strain

The S700 grade was found to have the lowest maximum surface strains and the widest strain distribution when using R2t punches. The distributions at 90° were in triangular shape with a base width of around six times sheet thickness and peak strains of 0.24 – 0.29 (TD) and 0.31 – 0.34 (RD), as can be seen from Figures 46 – 48. No surface defects could be seen on the specimen surfaces with R2t punches nor with R1t punches (Figure 26).

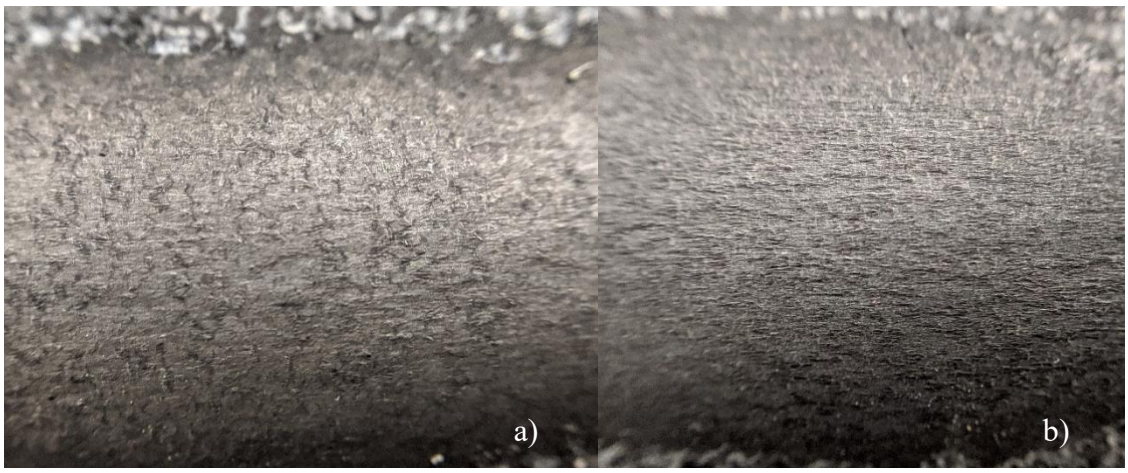

Figure 26. Surface of S700 specimens. a) Test #06b with 0.66 peak strain. b) Test #22b with 0.68 peak strain.

The S900 was measured to produce the narrowest strain distributions and the greatest maximum strains out of the tested materials. When using R2t punches, the maximum surface strains were measured growing almost linearly throughout the tests, unlike the S700 and S1100 grades, which started to stagnate towards the end of the tests (Figures 26 – 28). As can be seen from Figures 46 – 48, the strains at 90° are concentrated in a narrow area with a width of around two times sheet thickness and a peak strain of 0.56 – 0.65 (TD) and 0.65 – 0.78 (RD). The amount of strain the S900 grade sustained without fracturing is surprising, considering the total elongation is under 10% for this material (Table 2). Although the material did not fracture, shear banding, orange peeling or other defects are likely with this amount of strain. In closer inspection, S900 specimens with over 0.6 peak strain were observed to have clearly visible shear banding on the outer surface, with some specimens (over 0.7 peak strain) developing deep grooves that could be considered cracking or fracturing (Figure 27).

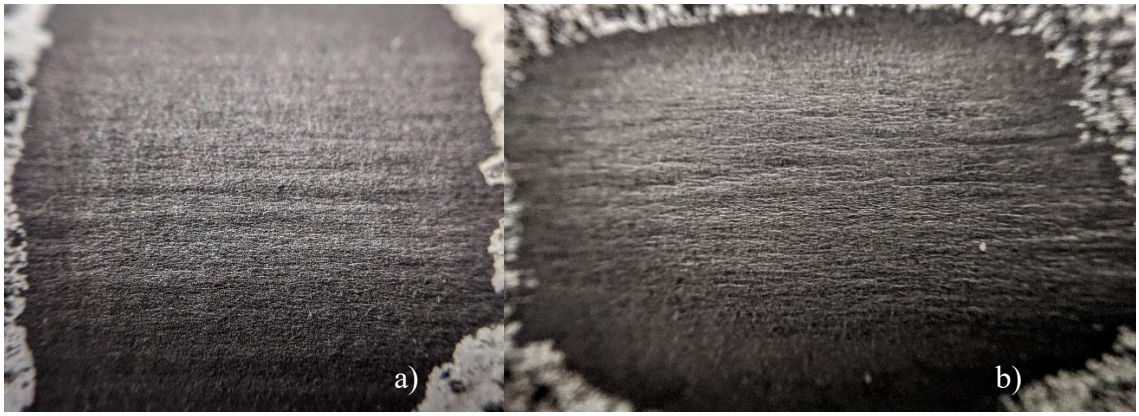

Figure 27. Surface damage on S900 specimens. a) Test #29 with 0.71 peak strain before unloading. b) Test #63 with 0.81 peak strain before unloading.

When using a R2t punch, the S1100 grade fractured in both longitudinal and transverse directions with the 4 mm sheet and in the transversal direction with the 8 mm sheet. However, for the tests that did not fracture, the maximum strains and strain distributions at 90° were found to be in between the S700 and S900 grades. As can be seen in Figures 47 and 48, the strain distributions have a peak in the middle of around 0.40 – 0.41 strain, and plateaus on the sides of the peak of around 0.12 – 0.13 strain. Despite the lower strain, the non-fractured S1100 specimens sustained similar damage on the surface as the S900, in the form of shear banding and surface cracking (Figure 28). It can then be concluded that compared to the S900, the S1100 distributes strain more evenly initially, when the strain is low, but cannot sustain as large amounts of local deformation without surface damage.

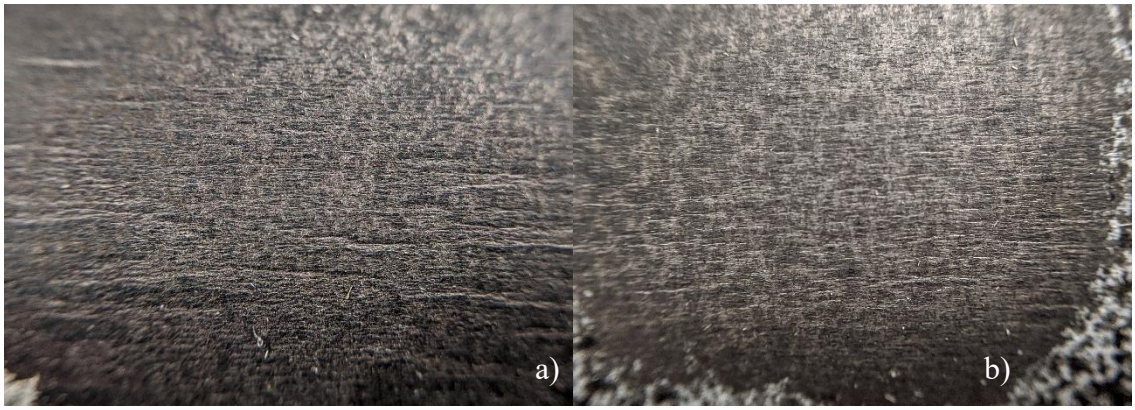

Figure 28. Surface damage on S1100 surfaces. a) Test #33 with 0.41 peak strain. b) Test #67 with 0.40 peak strain.

Similar observations were made when using R4t punches. As can be seen from Figures 32 – 34, the S1100 grade produced significantly lower strains than the S900 in all tests. The peak surface strains for the S900 grade at 90° angle were measured around 0.20 – 0.36, while the S1100 grade produced peak strains of 0.16 – 0.19, as can be seen from Figures 50 – 52 in Appendix 2.

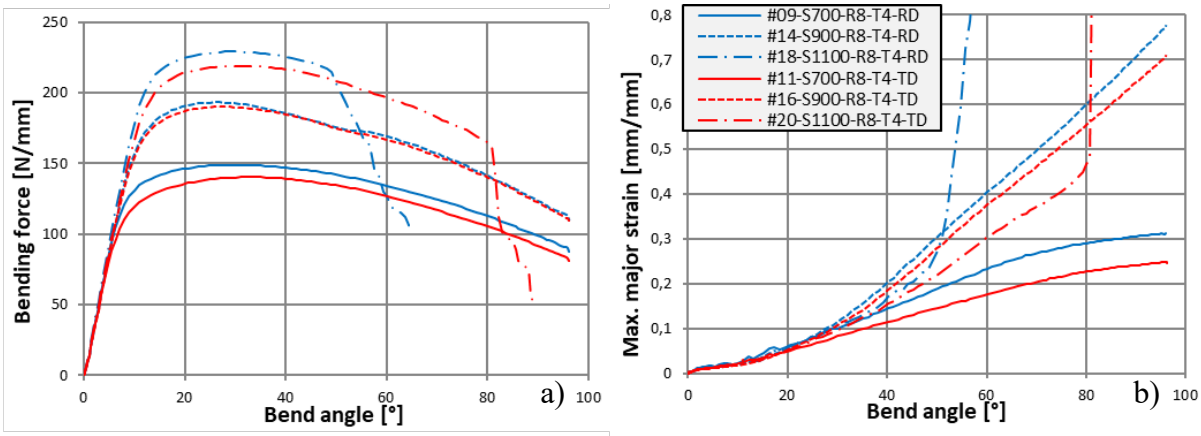

Figure 29. a) Bending force curve and b) maximum surface strain as a function of the bending angle. W = 110 mm, V_p = 1 mm/s, R_p = 8 mm, t = 4 mm.

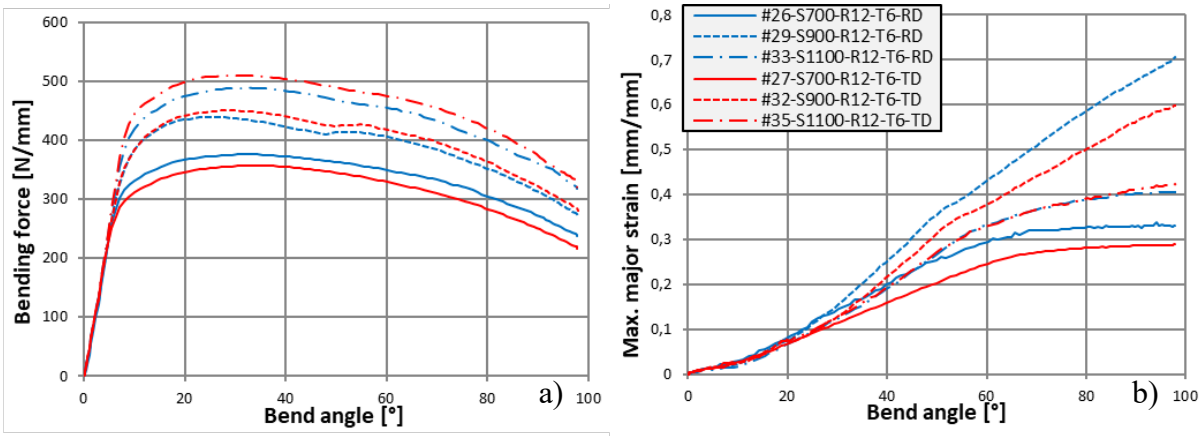

Figure 30. a) Bending force curve and b) maximum surface strain as a function of the bending angle. W = 110 mm, V_p = 1 mm/s, R_p = 12 mm, t = 6 mm.

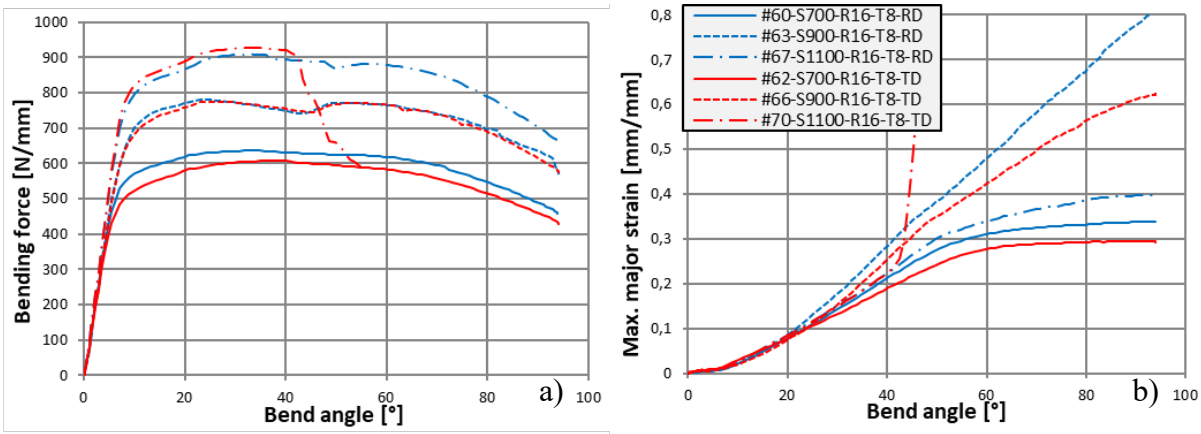

Figure 31. a) Bending force curve and b) maximum surface strain as a function of the bending angle. W = 110 mm, V_p = 1 mm/s, R_p = 16 mm, t = 8 mm.

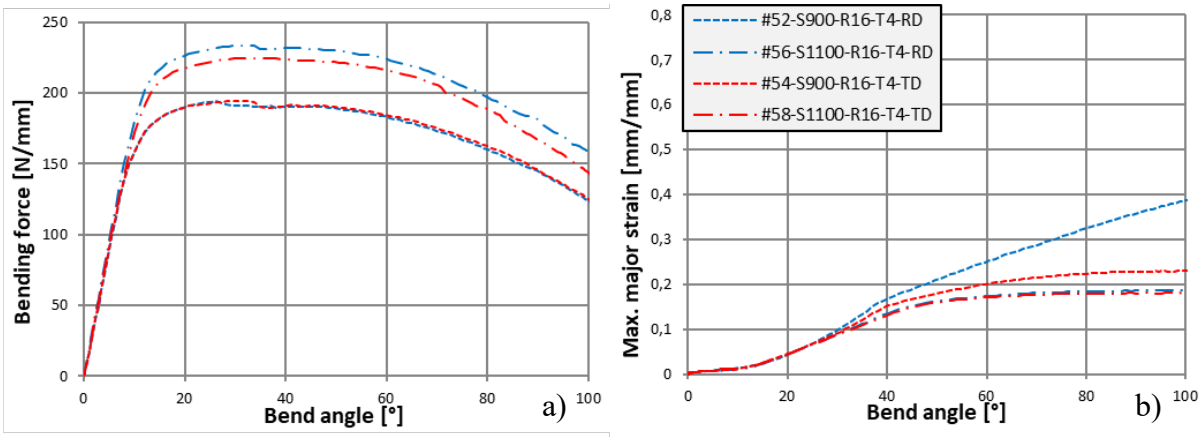

Figure 32. a) Bending force curve and b) maximum surface strain as a function of the bending angle. W = 110 mm, V_p = 1 mm/s, R_p = 16 mm, t = 4 mm.

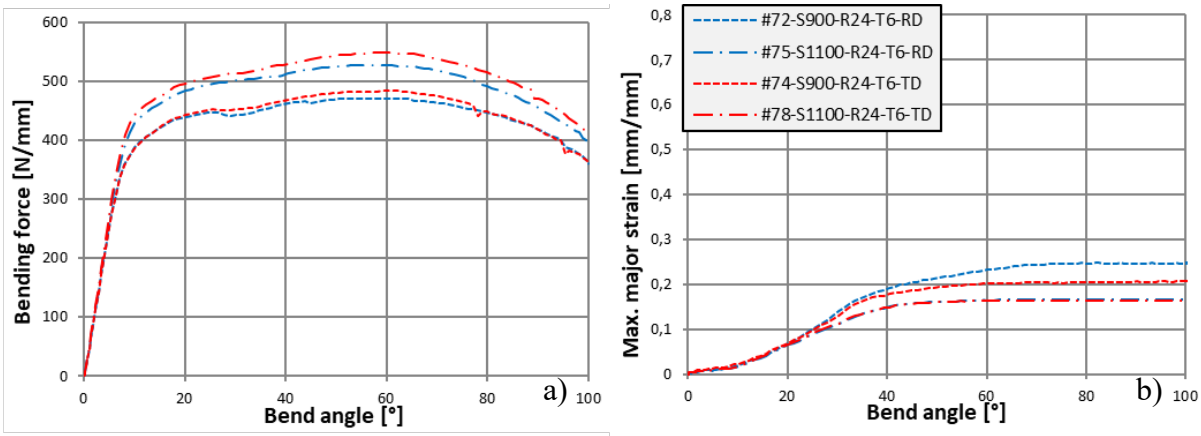

Figure 33. a) Bending force curve and b) maximum surface strain as a function of the bending angle. W = 110 mm, V_p = 1 mm/s, R_p = 24 mm, t = 6 mm.

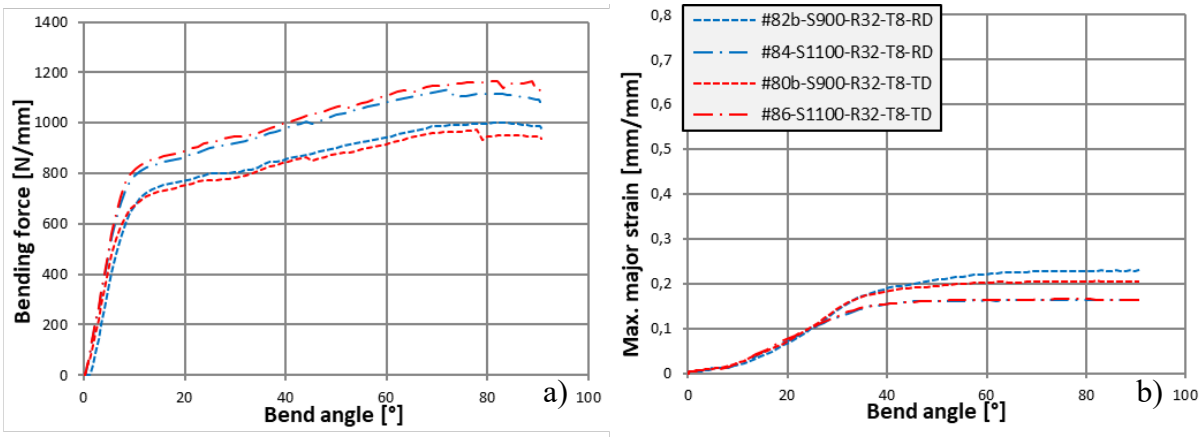

Figure 34. a) Bending force curve and b) maximum surface strain as a function of the bending angle. W = 110 mm, V_p = 1 mm/s, R_p = 32 mm, t = 8 mm.

4.4 Rolling direction

In this section, the measured effects of the rolling direction are discussed. For each material and sheet thickness, both longitudinal (RD) and transversal (TD) bending were tested. For further clarification, longitudinal bending in this thesis refers to an orientation, where the bending axis is parallel with the rolling direction.

4.4.1 Effect of rolling direction on bending force

The effect of the rolling direction varied between the different materials and sheet thicknesses. For the S700 grade, the bending force was always greater in the longitudinal direction. Longitudinal direction also required greater or equal forces for the S900 grade. Interestingly, for the S1100 grade, there was a sharp contrast in the effect of the rolling direction between the different sheet thicknesses. The 4 mm sheet appeared to require higher forces in the longitudinal direction, while the 6 mm and 8 mm sheets required higher bending force in the transversal direction. This contrast aroused suspicion of a mix-up in the rolling direction markings of the 4 mm sheet on the material supplier side, and the suspicion was further backed up by microstructure analysis. Thus, it is likely that in reality, the 4 mm sheet required more force in the transversal direction as well. The measured effect of the rolling direction on each parameter combination is presented in Table 5, expressed as a change in the peak force when changing from transverse to longitudinal bending direction.

Table 5. Effect of rolling direction change on the maximum force, expressed as a percentual change in force when switching from transverse to longitudinal bending. *Die width tests included. **Rolling direction likely reversed

	S700 R1t	**S700 R2t**	**S900 R2t**	**S900 R4t**	**S1100 R2t**	**S1100 R4t**
T4	+6.4%	+6.6%	+3.2%	+1.5%	+4.6%**	+3.5%**
T6	+3.7%	+5.4%	-0.31% *	+0.053%	-3.6%	-3.3%
T8	+6.5%	+5.6%	-0.14%	+2.3%	-1.9%	-3.5%

4.4.2 Effect of rolling direction on strain

The measured effects of rolling direction on maximum strains are presented in Table 6. For the S700 and S900 grades, longitudinal bending produced significantly higher peak strains compared to the transversal direction. The rolling direction change did not affect the strain distribution shape, as can be seen from Figures 46 – 52.

For the S1100 grade, the rolling direction was not observed to have any significant effect on the strain distributions or peak strains. It should be noted that despite not showing any measurable difference on the surface strains (Figure 49), the 8 mm sheet only fractured in the transversal direction.

There seems to be no correlation between the effects of the rolling direction in maximum force and the effects in maximum strain. Tests with identical maximum forces in both directions still had substantially higher strains in the longitudinal direction. (Figures 46 – 52 and 29 – 34)

Table 6. Effect of rolling direction change on the peak strains at 90° angle, expressed as a percentual change in strain when switching from transverse to longitudinal bending. *Die width tests included.

	S700 R1t	**S700 R2t**	**S900 R2t**	**S900 R4t**	**S1100 R2t**	**S1100 R4t**
T4	+54 %	+27 %	+8.9 %	+57 %	Fracture	+3.0 %
T6	+38 %	+15 %	+15 %*	+20 %	-2,1 %	+1.5 %
T8	+30 %	+14 %	+27 %	+12 %	Fracture	-0.73 %

4.5 Die width

The effects of die width are discussed in this section. Three die widths were tested: 70 mm, 90 mm and the default width of 110 mm. The material for all tests was the 6 mm sheet of S900 grade and testing was done in both longitudinal and transversal directions.

4.5.1 Effect of die width on bending force

The effect of the die width on the maximum bending force and maximum strain is presented in Table 7. As could be expected, the bending force increased as the die width decreased. Compared to the calculated values based on Formula (21) (SSAB), the measured increase in force between 110 mm and 90 mm die widths was close to expected. However, decreasing the die width further to 70 mm increased the force more than what could be expected based on the calculated values.

The reason for this was undoubtely the second increase in force after around 45°, leading to a second peak at around 70° angle (Figure 35a). This second peak is caused by the contact point shift towards the side of the punch and the consequental decrease in the bending moment arm. This second peak was observed to happen to some extent with all of the die widths (Figure 35a), but as the effect is magnified with the smaller die widths, only the 70 mm die width produced a second peak high enough to influence the maximum force.

Table 7. Effect of die width on maximum force and maximum strain.

	W70/W90	**W70/W110**	**W90/W110**
Max. Force	+42 %	+80 %	+27 %
Formula (21) (SSAB)	+38%	+77%	+28%
Max. Strain at 90°	-4.2 %	-4.6 %	-0.29 %

4.5.2 Effect of die width on strain

As illustrated in Figure 35b, the maximum strains at the surface followed a very similar trend until around 50° bend angle, after which the longitudinal and transverse bending directions diverged. The different die widths seemed to only affect the maximum strains after around 80° angle, when the strains of the 70 mm die width samples started to stagnate.

The strain distributions at 90° were also barely affected by the change in die width (Figure 53 in Appendix 2). On average, the peak strains were measured around 4 – 5 % lower with the 70 mm die width compared to the other die widths. With the 70 mm width, small secondary peaks were formed at around 10 mm distance from the center. Strain distributions measured at 80° angle (Figure 54 in Appendix 2) confirm that the stagnation of the peak strain is caused by the growth of the secondary peaks.

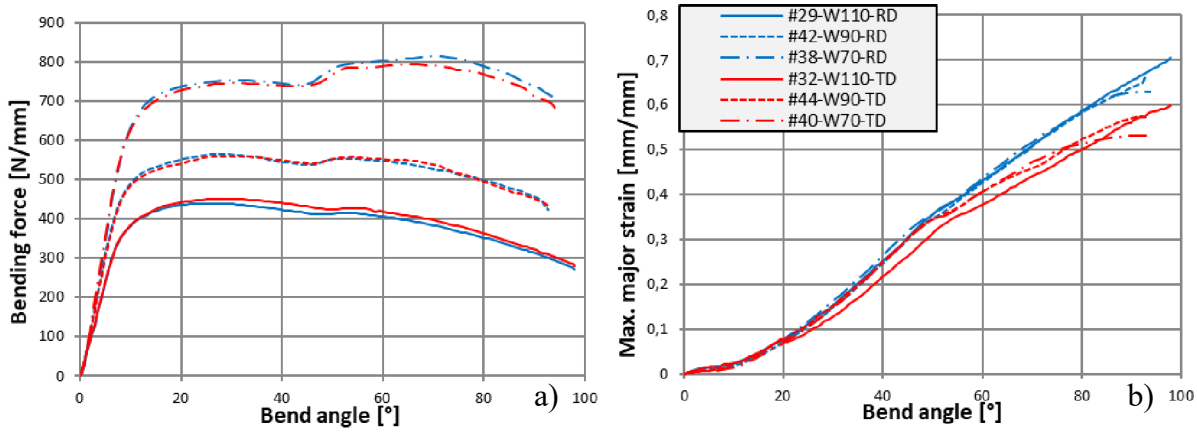

Figure 35. a) Bending force curve and b) maximum surface strain as a function of the bending angle. Material: S900, W = 110/90/70 mm, V_p =1 mm/s, R_p =12 mm, t = 6 mm.

4.6 Punch velocity

Two different punch velocities of 1 mm/s and 10 mm/s were tested. No measurable effect could be found on the bending force curves of any of the tested materials (Fig. 36a). The strain curves and 90° sections were also found near identical for all materials, as can be seen in Figures 36b and 55. From these tests, a conclusion could be made that a change of punch speed from 1 mm/s to 10 mm/s has very little effect on bending of the tested materials.

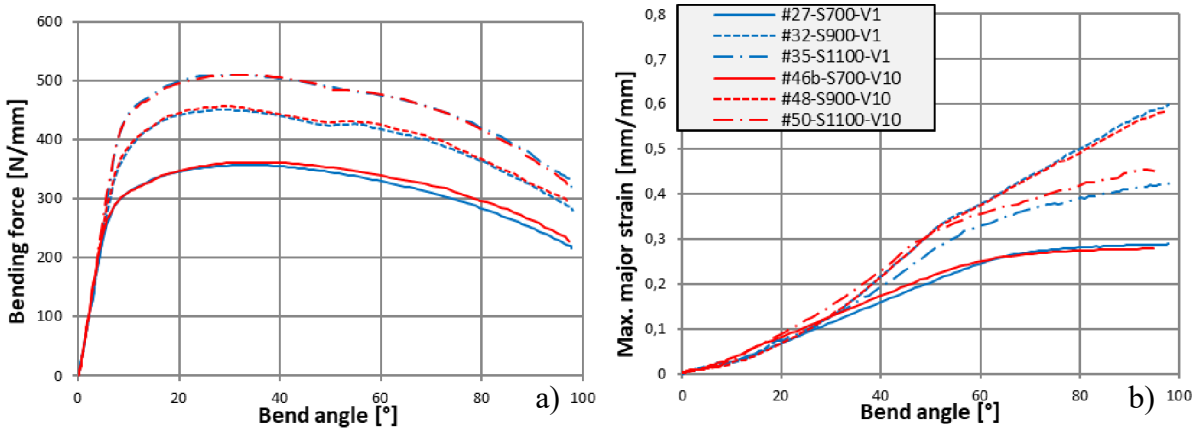

Figure 36. a) Bending force curve and b) maximum surface strain as a function of the bending angle. W = 110 mm, V_p = 1/10 mm/s, R_p = 12 mm, t = 6 mm, transverse bending.

4.7 Comparison of force estimation formulas

Using the measured bending force data, the accuracy of bending force estimation formulas (20), (21), and (28), were calculated. For the constants in the force estimation formulas, values of C = 1.6 (according to Ruukki 2014) and μ = 0.2 were used. The estimated maximum force values, based on the three formulas, were compared to the measured maximum force values, and the mean absolute percentage errors (MAPE) were calculated for each formula. Because of the slight bias of MAPE towards underestimations, the errors were also calculated using a mean of the logarithmic accuracy ratios (MLA):

$$MLA = \frac{1}{n}\sum_{i=1}^{n} \ln\left(\frac{F_{Ei}}{F_{Mi}}\right), \tag{32}$$

Where F_{Ei} is the estimated value of force and F_{Mi} is the measured force. Tests with missing tensile data (Table 2) were excluded from the comparison.

Based on the mean errors presented in Table 8, the most accurate of the three formulas was the SSAB formula, followed by Vorkov's model. Looking at Figures 56 – 59 the SSAB formula tends to underestimate the peak force in most cases, while Vorkov's formula and the Common formula tend to overestimate. Since press brakes and bending tools have maximum force limits, which cannot be exceeded, overestimating formulas may be more desirable in practice to have some safety margin in the estimations.

While the two other formulas only give a single peak force value, Vorkov's formula can also be used to calculate the force as a function of the bend angle, which may be useful for example in large radius bending where the desired bending angle can be reached before the ultimate peak of the bending force curve.

Table 8. Mean error of the force estimation formulas.

	Vorkov	**SSAB**	**Common**
MAPE	11.2 %	6.6 %	22.0 %
MLA	10.6 %	6.9 %	19.8 %

4.8 Comparison to circular model

As can be seen from Figures 40 – 55, the circular model does not fit most of the measured 90° strain distributions well. The strain in the circular model is distributed evenly across the whole circular part, while in the measured strain distributions, the strain was generally concentrated near the center of the bend in a narrower peak with maximum strains multiple times that of the circular model. The tests, where the circular model fit the best, were the ones with the lowest and widest strain distributions. Larger punch radii, transverse bend direction and the S700 material were previously mentioned as contributors to wider and lower strain distributions, and the tests that feature those properties also fit the circular model better. Figures 51 and 52 are good examples of large enough punch radii making the bend closer to the circular model.

Conversely, tests with smaller punch radii, longitudinal direction and the S900 material were found to fit the circular model worst, as they were all parameters that contributed to narrow strain distributions with high peaks. Example of especially bad fitting tests can be seen in Figures 46 – 48, where the peak strains reach 3 – 4 times the amount expected by the circular model.

As the circular model is based on simplifying assumptions, such as a rigid-plastic material, it is no surprise that most of the measured strain distributions poorly. But because surface contact between the punch and the sheet happens between the 3-point

and 4-point bending phases, the circular model may still be useful as comparison tool. For instance, the surface strain measurements can be compared to the calculated strain of a circular bend that has surface contact to the punch (i.e. wrap-around), to determine if the measured bend has lost contact to punch nose and transitioned from 3-point to 4-point bending.

In order to investigate the accuracy of comparing the measured strains to the circular model as a method for determining the shift from 3- to 4-point bending, some photos were taken from the side-view of the bending setup. The photos and their corresponding strain distributions are presented in Figures 60 – 65 in Appendix 4. It is difficult to pinpoint the exact angles when the 3-point to 4-point switch occurs from the photos alone, due to the limited image quality and the edge deformation effect possibly making the sheet appear more separated from the punch than it actually is. However, the photos seem to match the estimation method relatively well. For instance, the switch from 3- to 4-point bending should happen at around 40° in Figure 64, and from the photos it can be clearly seen that 3-point bending, surface contact and 4-point bending are in effect at 30°, 40° and 50°, respectively. On the other hand, clear 4-point bending cannot be seen at 60° in Figure 60, or at 50° in Figures 61 and 62. It is possible that the circular model slightly underestimates the strains at the switch point from 3- to 4-point bending, due to ignoring the neutral axis shift. In this case, the actual transition from 3- to 4-point bending would happen slightly later than the circular model suggests.

4.9 Four-point bending and contact point shift

Looking at Figures 23 – 36, it is apparent that both the bending force and the maximum strain curves always start in a similar manner regardless of the varied parameters. The differences in the curve shapes only show after around 30 – 50°, when the rate of change of the bending force increases and the rate of change of the maximum strain decreases simultaneously. The point at which this happened varied between the tests. The change happened at around 45 – 50° for R2t punches and around 30 – 40° for R4t punches. These sudden changes are likely a consequence of the contact points shifting towards the sides of the punch due to the loading scheme changing from 3-point to 4-point bending.

Figures 37 and 38 illustrate the effect of the contact point shift on the bending forces and maximum strains of two tests with different punches. Both the force and the strain stay

identical until around 30° as the punch radius is irrelevant in 3-point bending. After 26°, the maximum strains in test #72 exceed the strain of 0.11 calculated for a circular bend with surface contact to the punch, meaning that the plate has bent enough to have its inner radius of curvature decrease below the 24 mm punch radius, thus transitioning to 4-point bending. At the start of the 4-point bending, the contact points are still close together at the center, which means the loading scheme is still close to 3-point bending and does not yet affect the bending forces and maximum strains measurably. The measured changes begin after 30° when, presumably, the contact points start to shift quickly away from the center towards the sides of the punch. The contact point shift then decreases the bending moment arm and focuses further strain towards the sides, thus increasing the required bending force and decreasing the maximum strain at the center of the bend.

As test #29 has a smaller punch of 12 mm radius, the 3-point bending phase lasts longer. According to the calculated strains of circular bend with a 12 mm inside curvature radius, the transition to 4-point bending happens after around 35°. However, no noticeable change can be seen until around 47 – 48°. This apparent delay may be a result of two factors. Fistly, the contact point shift happens slower with smaller punches, meaning that the contact points likely stay longer close together at the center, thus remaining in a loading scheme close to 3-point bending until the contact point shift accelerates to a noticeable speed. Secondly, the calculated strain level of 0.2 may be an underestimation, since the circular model assumes the neutral axis is fixed at the middle of the cross-section of the sheet, while in reality, the neutral axis shifts slightly towards the punch, increasing the strains on the outer surface. This would mean that the transition to 4-point bending actually happens a few degrees after the estimated angle of 35°.

Similar delays were observed with other tests as well. With R4t punches, the delay was always under 5°, while with R2t punches it was around 10 – 15°. Tests on 4mm S700 sheets with R1t punches seemed to stay in the 3-point bending phase for the whole test, while the 6 mm and 8 mm sheets of S700 started to show signs of contact point shift around 20° after exceeding the calculated strain level of 0.33 at which the transition from 3- to 4-point bending should happen.

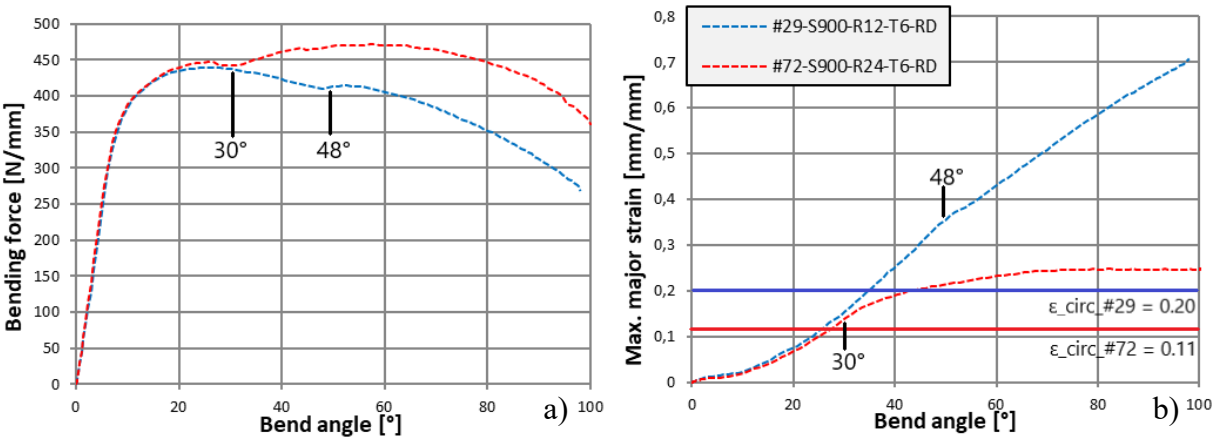

Figure 37. Effect of the contact point shift on a) the bending force and b) maximum strain development.

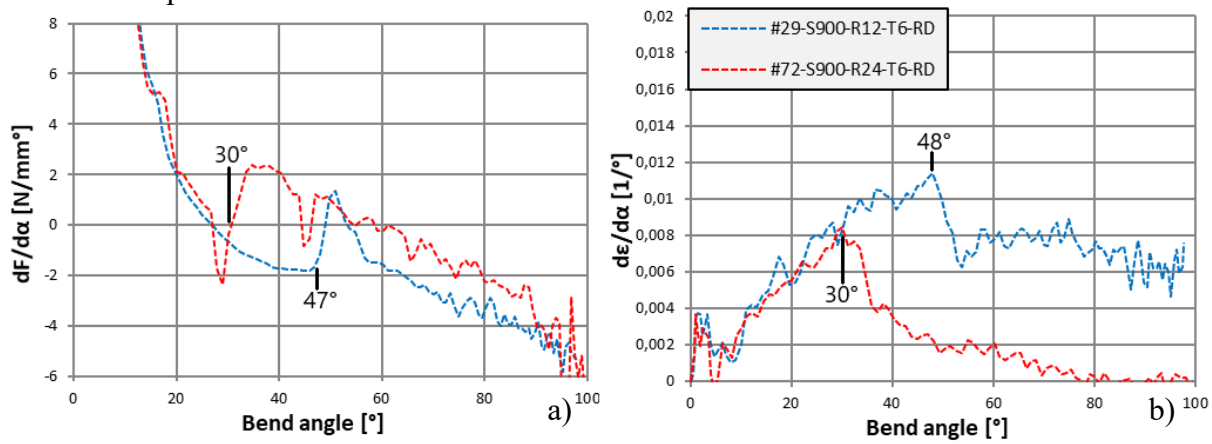

Figure 38. Effect of the contact point shift on the rates of change of the a) bending force and b) the maximum strain.

4.10 Strain distribution area

One interesting observation regarding the measured strain data was that the area under the strain distribution seemed to stay constant between all the different punches, materials, bend directions and die widths, despite the vast differences in the maximum strains and distribution shapes. The only two parameters that affected the area were the bending angle and the sheet thickness. Examples of different distributions with similar areas are presented in Figure 39. The areas for each sheet thickness, calculated using the trapezoidal rule, are presented in Table 9.

The reasons for this characteristic probably lie in the geometry of bending. The amount of strain on the surface depends on its curvature and its distance to the neutral axis. The distance to the neutral axis depends mostly on the sheet thickness, although the neutral axis shift affects it as well.

The curvature κ of a curve can be defined as:

$$\kappa = \frac{1}{R}, \tag{33}$$

Where R is the radius of curvature. The curvature κ can also be expressed as:

$$\kappa = \frac{d\varphi}{ds}, \tag{34}$$

Where φ is the tangential angle (turning angle) and s is the arc length of the curve. The total curvature of a curve can be calculated with a definite integral of the curvature along the curve:

$$\int_a^b \kappa(s)\, ds = \int_a^b \frac{d\varphi(s)}{ds} ds = \varphi(b) - \varphi(a) \tag{35}$$

This can be applied to bending as well, as the neutral axis of the bend is essentially a convex curve. The bending angle α is the difference in tangential angles between the two ends of the plate. If a and b are considered to be the end points of the neutral axis at opposite sides, the total curvature of a neutral axis can be calculated as follows:

$$\int_a^b \kappa_n(s)\, ds = \int_a^b \frac{1}{R_n}(s)\, ds = \varphi(b) - \varphi(a) = \alpha\,, \tag{36}$$

Where κ_n is the curvature of the neutral axis. The definite integral of the strain distribution, using the simplistic Formula (18):

$$\int_a^b \varepsilon_b(s)\, ds = \int_a^b \frac{y}{R_n}(s)\, ds = \frac{t}{2}\int_a^b \frac{1}{R_n}(s)\, ds \tag{37}$$

After substituting Equation (36), Equation (37) becomes:

$$\int_a^b \varepsilon_b(s)\, ds = \frac{1}{2} t\alpha \tag{38}$$

This would mean that if the sheet thickness and the bend angle are constant, the integral of the strain distribution is also constant. While this model is inaccurate for most applications because of its simplification in assuming a perfectly elastic material with a fixed neutral axis, it does provide some context for this observed phenomenon.

Table 9. The area under the strain distributions for each sheet thickness.

Sheet thickness	A_ε at 90° [mm]
4	2.9 – 3.2
6	4.9 – 5.1
8	6.5 – 6.9

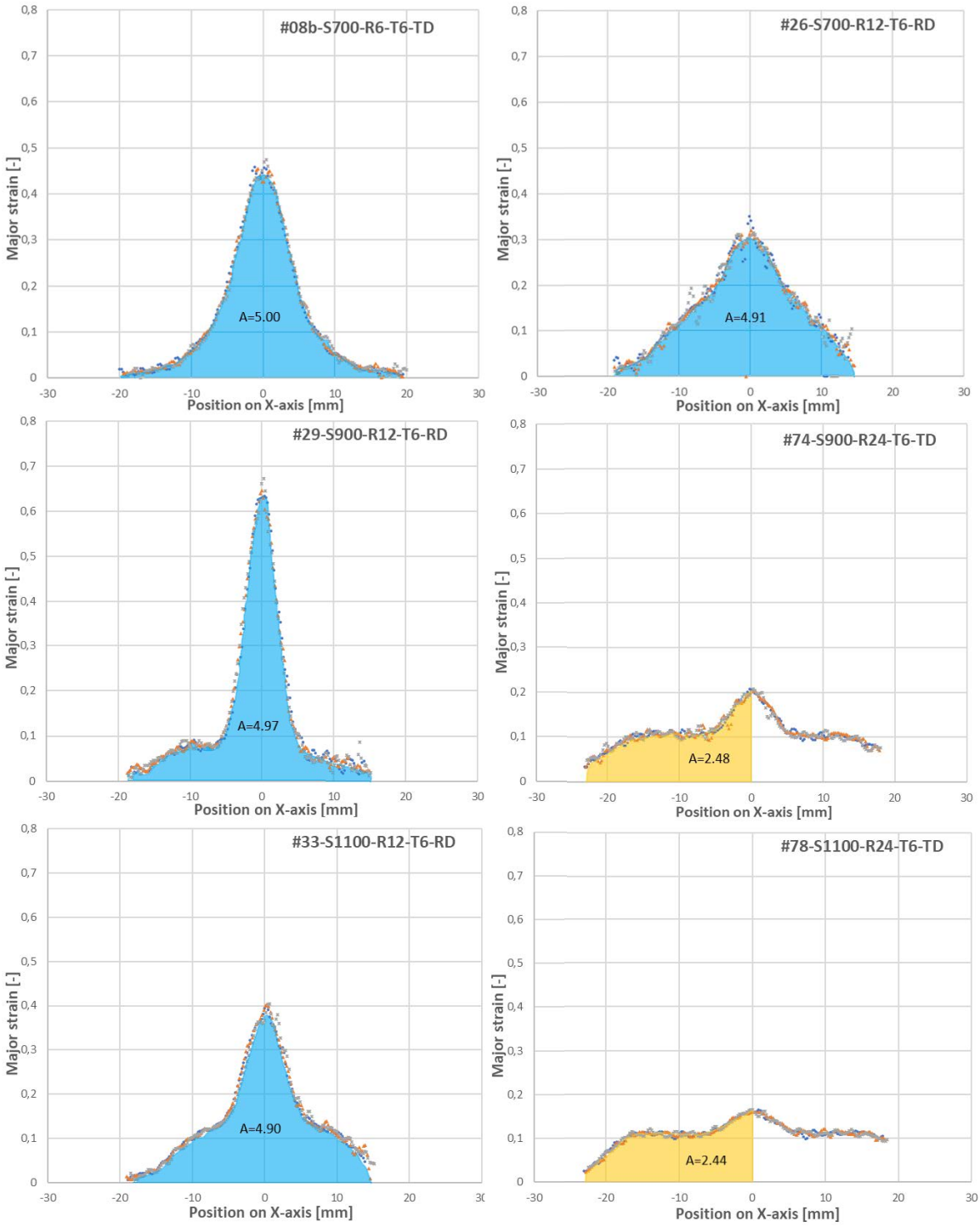

Figure 39. The area under the strain distributions of 6 mm sheets at 90° bending angle.

5 CONCLUSIONS

The effects of the selected bending parameters on bending forces and strains on the outer surface were investigated with bending tests, utilising a universal tensile test machine and digital image correlation in the test setup.

The R/t ratio was found to affect the bending force especially in combination with thicker sheets. Larger punches were found to require higher forces when bending 6 mm and 8 mm sheets as well as shift the force peak towards the end of the tests because of the contact point shift after transitioning from 3- to 4-point bending. The R/t ratio was found to have a crucial effect on the measured strains. Smaller punches were found to result in narrower strain distributions and significantly higher maximum strains, which also resulted in fracturing in the S1100 material.

Sheet thickness was found to have differing effects on the bending force depending on the R/t ratio of the used punch. When using smaller punches, the bending force was found to scale directly proportionally to the square of the sheet thickness. Using larger punches was found to magnify the effect even further because of the contact point shift. The maximum strains were found to be slightly affected by the sheet thickness. The maximum strains in 6 mm and 8 mm sheets were measured to be similar in most of the experiments. The maximum strains in 4 mm sheets were measured lower than the other thicknesses in the S700 material but higher in the S900 and S1100. The strain distributions were found to increase in width proportionally to the sheet thickness.

The difference in bending force between the materials was found to be reasonably consistent with the ultimate tensile strengths but further testing was deemed necessary for any definite conclusions. The S1100 and especially the S900 were observed to develop a second peak in the force curve with the thicker sheets, as a consequence of the contact point shift. The measured strain distributions and maximum strains were found to differ significantly between the materials. S700 was found to produce the widest strain distributions with lowest maximum strains. Highest and narrowest strain distributions were measured in S900, which produced maximum strains up to 0.78 at a 90° bend angle. S1100 was surprisingly found to have generally lower and wider strain distributions than the S900. However, the S1100 could not sustain as high amount of strain as the S900 without fracturing or shear banding.

The rolling direction was found to have varying effects on both the bending force and the strains depending on the material. With S700, longitudinal bending required higher forces and produced higher maximum strains and narrower strain distributions. With the S900, the bending forces were slightly higher or equal in the longitudinal direction, but the strain distributions were significantly higher and narrower in the longitudinal direction. The S1100 was found to require more force in the transversal direction. The measured strains were identical in both directions of the S1100 material, although the transversal direction produced more fractures.

The die width was found to affect the bending force more than expected due to the magnified effect of the contact point shift when using smaller die widths. The measured strains on the surface were found to be mostly unaffected by the die width. Punch velocity was found to have no measurable effect on either the bending force or the strains on the outer surface.

Out of the three compared bending force estimation formulas, the SSAB formula was found to be the most accurate. However, it was also found to generally underestimate the maximum force, which may be problematical in practice.

The circular model was found to fit the measured strain distributions rather poorly due to its simplifying assumptions. Most of the measured strain distributions were significantly higher and narrower compared to the circular model. Larger punches, S700 material and the transversal bending direction were found to fit the circular model best, as they produced the widest and lowest strain distributions. Additionally, the areas under the measured strain distributions were observed to stay constant between the different punches, materials, bend directions and die widths. Out of the studied parameters, the area was found to depend only on the sheet thickness and the bend angle.

The effects of the contact point shift were found to happen after a certain delay after the estimated transition from 3- to 4-point bending. This delay was found to be shorter with larger punches, presumably because of the contact points moving faster with the larger punches, but underestimation of strain in the circular model was also suspected as a possible contributor.

6 FURTHER RESEARCH

The aim of this thesis was to provide a basis for further research by taking a broad look at the effects of a wide variety of parameters on the bending forces and strains on the outer surface. The sample size was small for each of the tested parameter combinations and thus further research is necessary for providing statistically significant numerical values for the measured effects.

Further testing could be conducted with even smaller punches, in order to determine the bending radii and angles at which each material fractures. Testing could also be continued beyond the 90° angle to investigate if the findings of this thesis also apply to the larger bending angles.

The tested samples could be further examined for surface quality and defects to provide a link between the defects and the measured strains on the surface. Further examination could be done to measure the hardness and microstructural changes across the cross-section of the bend to provide possible explanations for the findings in this thesis. Tensile testing with DIC strain measurements could also be useful for studying the correlation between the area reduction in tensile tests and the bendability of the materials.

REFERENCES

Aerens, R. and Masselis, S., 2000. Le pliage en l'air. Centre de Recherches Scientifiques et Techniques de l'Industrie des Fabrications Métalliques (CRIF), (MC110).

Arola, A.M., Kaijalainen, A.J. & Kesti, V., 2015. Evaluation of bendability of hot-rolled S960 grade steel using optical strain measurements and FE-modelling, Key Engineering Materials 2015, Trans Tech Publ, p. 610-616.

Arola, A.M., Kesti, V. & Ruoppa, R., 2015. The effect of punch radius on the deformation of ultra-high strength steel in bending, Key engineering materials 2015, Trans Tech Publ, p. 139-146.

Arola, A., Kaijalainen, A., Kesti, V., Pokka, A.P. & Larkiola, J., 2019. Digital image correlation and optical strain measuring in bendability assessment of ultra-high strength structural steels. Procedia Manufacturing, 29, p. 398-405.

Asnafi, N., 2000. Springback and fracture in v-die air bending of thick stainless steel sheets. Materials & Design, 21(3), p. 217-236.

Cheong, K., Omer, K., Butcher, C., George, R. & Dykeman, J., 2017. Evaluation of the VDA 238-100 tight radius bending test using digital image correlation strain measurement, Journal of Physics: Conference Series 2017, IOP Publishing.

Dadras, P., 1985. Stress-strain Relationships in bending. ASM Handbook., 8, p. 118-124.

Dannenmann, E., 1974. Tool Geometry and Punch Force in V-Die Bending. Werkstattstechnik, 64(9), p. 527-531.

Dao, M. & Li, M., 2001. A micromechanics study on strain-localization-induced fracture initiation in bending using crystal plasticity models. Philosophical Magazine A, 81(8), p. 1997-2020.

Datsko, J. & Yang, C.T., 1960. Correlation of bendability of materials with their tensile properties. Journal of Engineering for Industry. 82, p. 309-330.

De Vin, L.J., Streppel, A.H., Singh, U.P. & Kals, H.J.J., 1996. A process model for air bending. Journal of materials processing technology, 57(1-2), p. 48-54.

De Vin, L.J., 2000. Curvature prediction in air bending of metal sheet. Journal of Materials Processing Technology, 100(1-3), p. 257-261.

Horrocks, D. & Johnson, W., 1967. On anticlastic curvature with special reference to plastic bending: a literature survey and some experimental investigations. International Journal of Mechanical Sciences, 9(12), p. 835-844.

SFS- EN ISO 7438, 2016. Metallic materials. Bend Test. Finnish Standards Association SFS: 11 + 1 p.

Jones, E.M.C. & Iadicola, M.A., eds, 2018. A Good Practices Guide for Digital Image Correlation. International Digital Image Correlation Society.

Kaupper, M. and Merklein, M., 2013. Bendability of advanced high strength steels—A new evaluation procedure. CIRP Annals, 62(1), p. 247-250

Lange, K., 1985. Handbook of metal forming. McGraw-Hill Book Company, 1985, 1216 p. ISBN 0-87263-457-4

Lievers, W.B., Pilkey, A.K. & Worswick, M.J., 2003. The co-operative role of voids and shear bands in strain localization during bending. Mechanics of materials, 35(7), p. 661-674

Mandigo, F.N., 1985. Bending ductility tests. ASM Handbook., 8, p. 125-131.

Newby, J.R., 1985. Metals Handbook, Volume 8: Mechanical Testing.

Perduijn, A.B. & Hoogenboom, S.M., 1995. The pure bending of sheet. Journal of Materials Processing Technology, 51(1-4), p. 274-295.

Ruukki, 2014. Särmäys, Raex kulutusteräkset, ultralujat Optim QC teräkset [online document]. Available from: https://docplayer.fi/storage/24/4423982/1591302227/XsV-mY4i2CJOHtwoVnfIuQ/4423982.pdf [Accessed 4 June 2020]

SSAB, 2015. Strenx, Hardox and Docol - Bending of high strength steel [online document]. Available from: https://ssabwebsitecdn.azureedge.net/-/media/files/en/general-multibrand/912-en-bending-of-high-strength-steel.pdf [Accessed 4 June 2020]

Stelson, K.A., 1986. An adaptive pressbrake control for strain-hardening materials. Journal of Engineering for Industry. 108, p. 127-132.

Taylor, B., 1988. Formability testing of sheet metals. ASM Handbook., 14, p. 877-899.

Troive, L., 2017. New method for evaluation of bendability based on three-point-bending and the evolution of the cross-section moment, Journal of Physics: Conference Series 2017, IOP Publishing.

VDA 238-100, 2010. Test specification. Plate bending test for metallic materials. German Association of the Automotive Industry VDA: 8 + 5 p.

Vorkov, V., Aerens, R., Vandepitte, D. & Duflou, J.R., 2017. Experimental investigation of large radius air bending. The International Journal of Advanced Manufacturing Technology, 92(9-12), p. 3553-3569.

Vorkov, V., Aerens, R., Vandepitte, D. & Duflou, J.R., 2014. The multi-breakage phenomenon in air bending process, Key Engineering Materials 2014, Trans Tech Publ, p. 1047-1053.

Väisänen, A., Mäntyjärvi, K. & Karjalainen, J.A., 2009. Bendability of ultra-high-strength steel, Key Engineering Materials 2009, Trans Tech Publ, p. 611-620.

Wang, C., Kinzel, G. & Altan, T., 1993. Mathematical modeling of plane-strain bending of sheet and plate. Journal of Materials Processing Technology, 39(3-4), p. 279-304.

Appendix 1. Test numbering and parameter combinations.

Parameters								Results	
TEST #	Rp (mm)	W (mm)	Material	t (mm)	RD/TD	Vp (mm/s	(R/t)	F_{max}/b	ε_{max} (90°)
02b	4	110	700	3,97	R	1	1	149,43	0,43
03b	4	110	700	3,97	T	1	1	140,36	0,28
06b	6	110	700	6,02	R	1	1	368,07	0,64
08b	6	110	700	6,02	T	1	1	350,49	0,46
09	8	110	700	3,97	R	1	2	148,94	0,31
11	8	110	700	3,98	T	1	2	140,20	0,24
14	8	110	900	3,98	R	1	2	193,00	0,71
16	8	110	900	3,97	T	1	2	189,92	0,65
18	8	110	1100	4,09	R	1	2	229,00	Fracture
20	8	110	1100	4,07	T	1	2	218,82	Fracture
22b	8	110	700	7,92	R	1	1	639,09	0,67
24b	8	110	700	7,92	T	1	1	598,99	0,51
26	12	110	700	6,06	R	1	2	375,46	0,33
27	12	110	700	6,06	T	1	2	356,18	0,29
29	12	110	900	6,00	R	1	2	438,77	0,65
32	12	110	900	6,00	T	1	2	449,84	0,56
33	12	110	1100	6,04	R	1	2	488,57	0,40
35	12	110	1100	6,04	T	1	2	509,74	0,41
38	12	70	900	6,00	R	1	2	813,04	0,63
40	12	70	900	6,00	T	1	2	792,39	0,53
42	12	90	900	6,00	R	1	2	563,88	0,64
44	12	90	900	6,00	T	1	2	559,68	0,57
46b	12	110	700	6,04	T	10	2	361,29	0,28
48	12	110	900	5,98	T	10	2	455,48	0,55
50	12	110	1100	6,02	T	10	2	509,22	0,45
52	16	110	900	3,97	R	1	4	193,86	0,36
54	16	110	900	3,95	T	1	4	193,99	0,23
56	16	110	1100	4,05	R	1	4	233,41	0,19
58	16	110	1100	4,05	T	1	4	224,44	0,18
60	16	110	700	7,92	R	1	2	635,44	0,34
62	16	110	700	7,92	T	1	2	606,58	0,29
63	16	110	900	7,94	R	1	2	781,42	0,78
66	16	110	900	7,94	T	1	2	774,08	0,61
67	16	110	1100	8,02	R	1	2	908,90	0,40
70	16	110	1100	8,02	T	1	2	926,63	Fracture
72	24	110	900	5,98	R	1	4	470,92	0,25
74	24	110	900	5,98	T	1	4	483,07	0,21
75	24	110	1100	6,04	R	1	4	527,44	0,17
78	24	110	1100	6,04	T	1	4	548,51	0,16
80b	32	110	900	7,92	T	1	4	971,84	0,20
82b	32	110	900	7,92	R	1	4	1001,27	0,23
84	32	110	1100	8,02	R	1	4	1132,91	0,16
86	32	110	1100	8,02	T	1	4	1164,85	0,16

Appendix 2. Strain distributions.

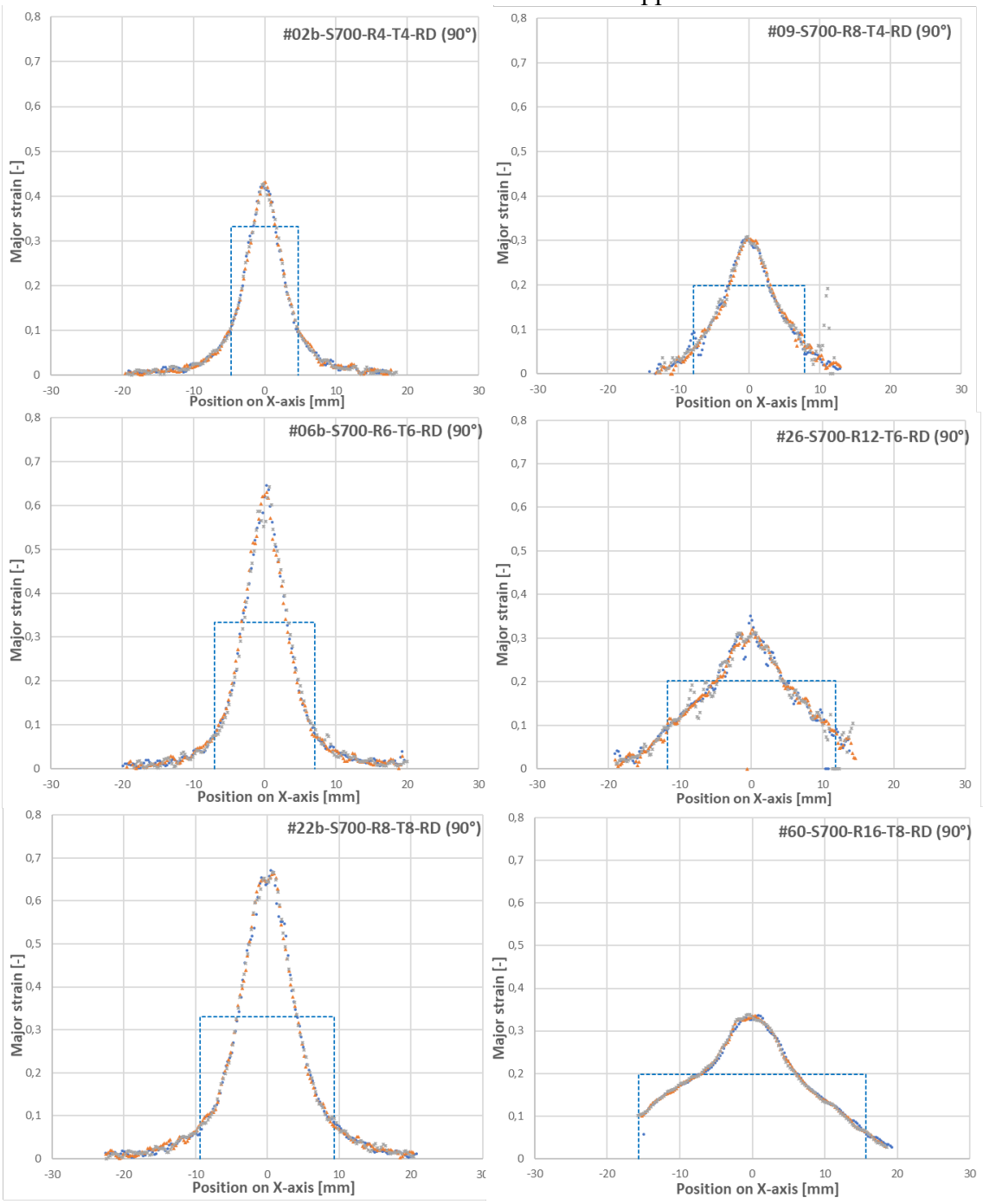

Figure 40.

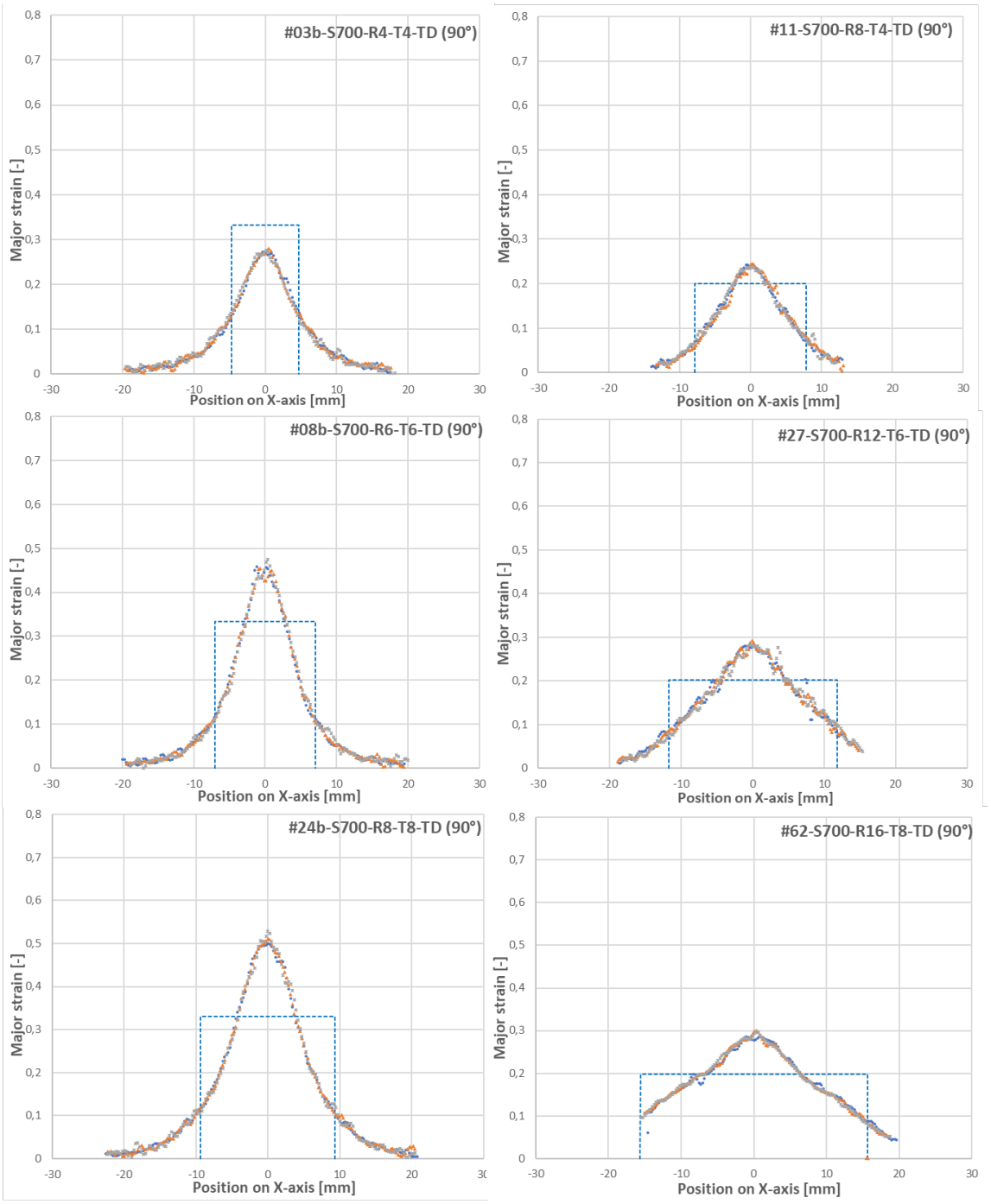
#03b-S700-R4-T4-TD (90°)
#11-S700-R8-T4-TD (90°)
#08b-S700-R6-T6-TD (90°)
#27-S700-R12-T6-TD (90°)
#24b-S700-R8-T8-TD (90°)
#62-S700-R16-T8-TD (90°)
Major strain [-]
Position on X-axis [mm]

Figure 41.

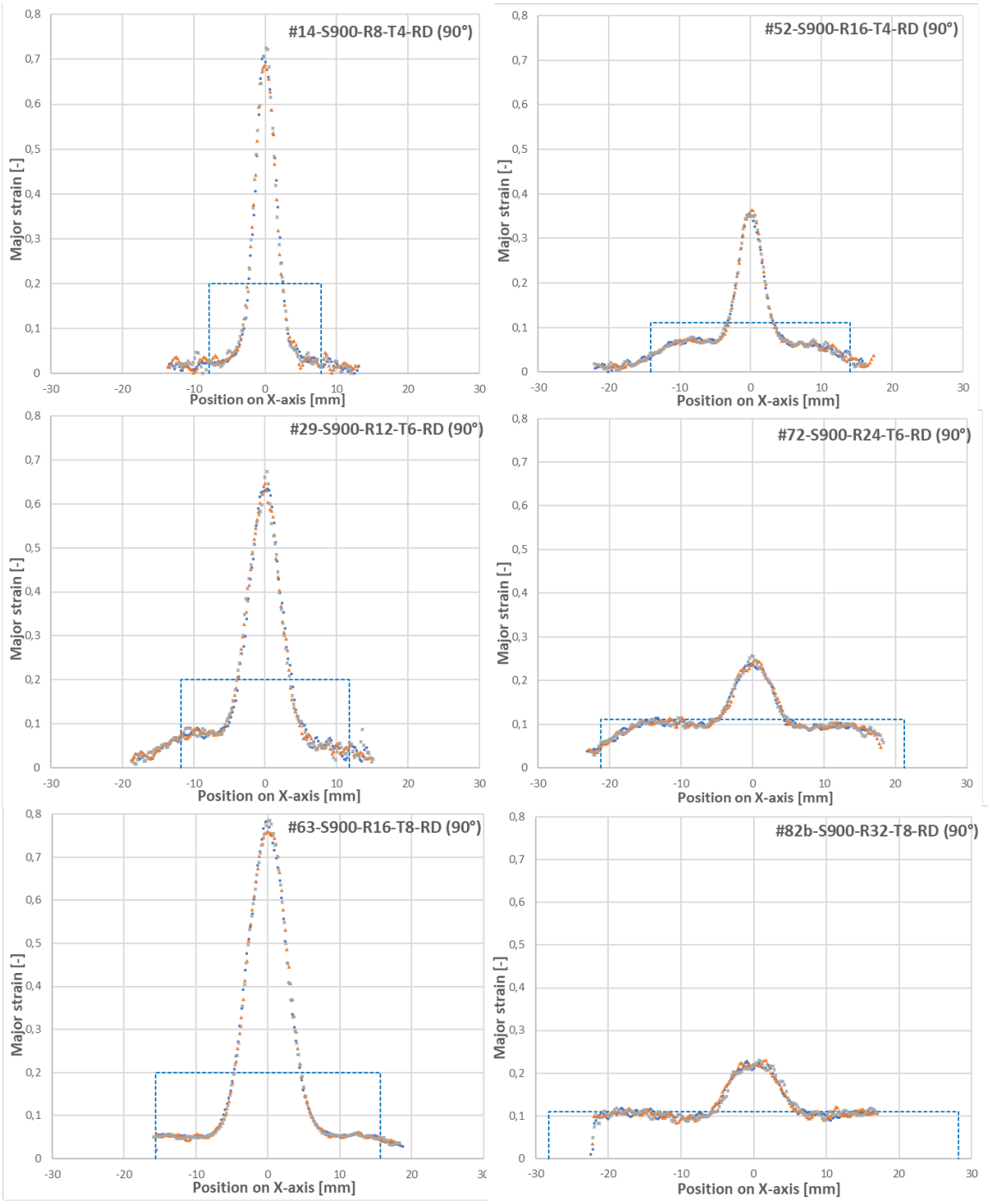
#14-S900-R8-T4-RD (90°)
#52-S900-R16-T4-RD (90°)
#29-S900-R12-T6-RD (90°)
#72-S900-R24-T6-RD (90°)
#63-S900-R16-T8-RD (90°)
#82b-S900-R32-T8-RD (90°)
Major strain [-]
Position on X-axis [mm]

Figure 42.

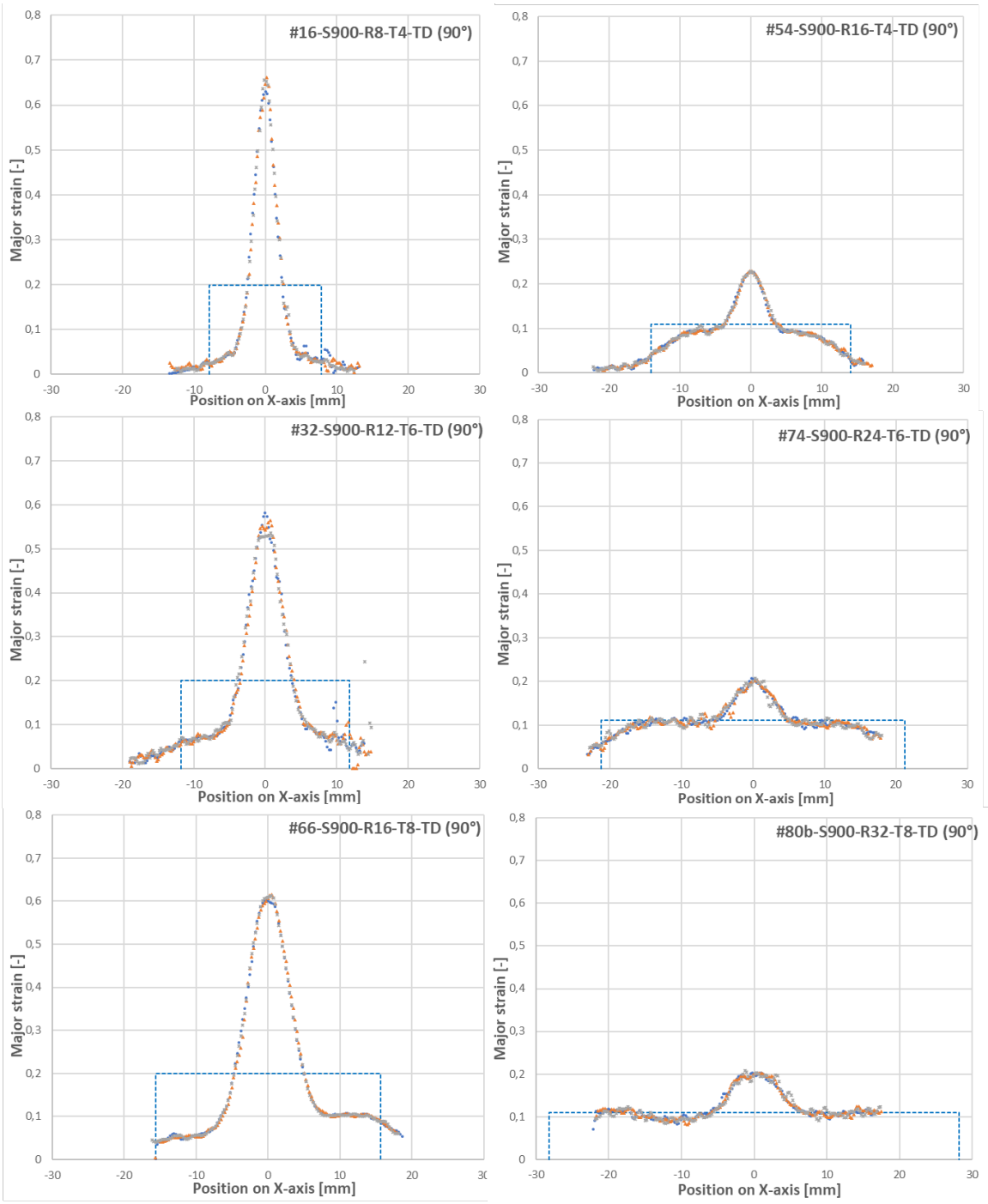
#16-S900-R8-T4-TD (90°)
#54-S900-R16-T4-TD (90°)
#32-S900-R12-T6-TD (90°)
#74-S900-R24-T6-TD (90°)
#66-S900-R16-T8-TD (90°)
#80b-S900-R32-T8-TD (90°)
Major strain [-]
Position on X-axis [mm]

Figure 43.

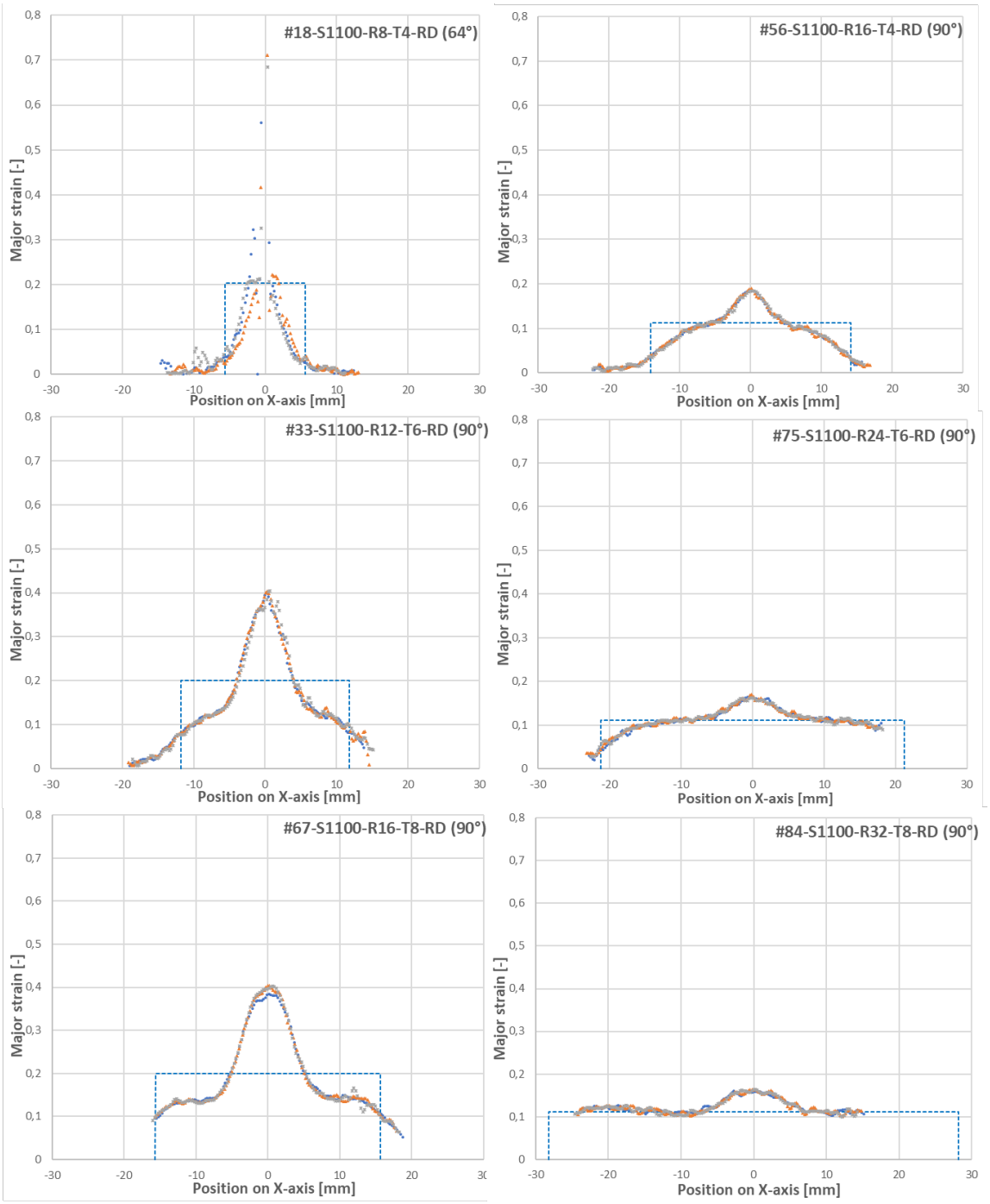
#18-S1100-R8-T4-RD (64°)
#56-S1100-R16-T4-RD (90°)
#33-S1100-R12-T6-RD (90°)
#75-S1100-R24-T6-RD (90°)
#67-S1100-R16-T8-RD (90°)
#84-S1100-R32-T8-RD (90°)
Major strain [-]
Position on X-axis [mm]

Figure 44.

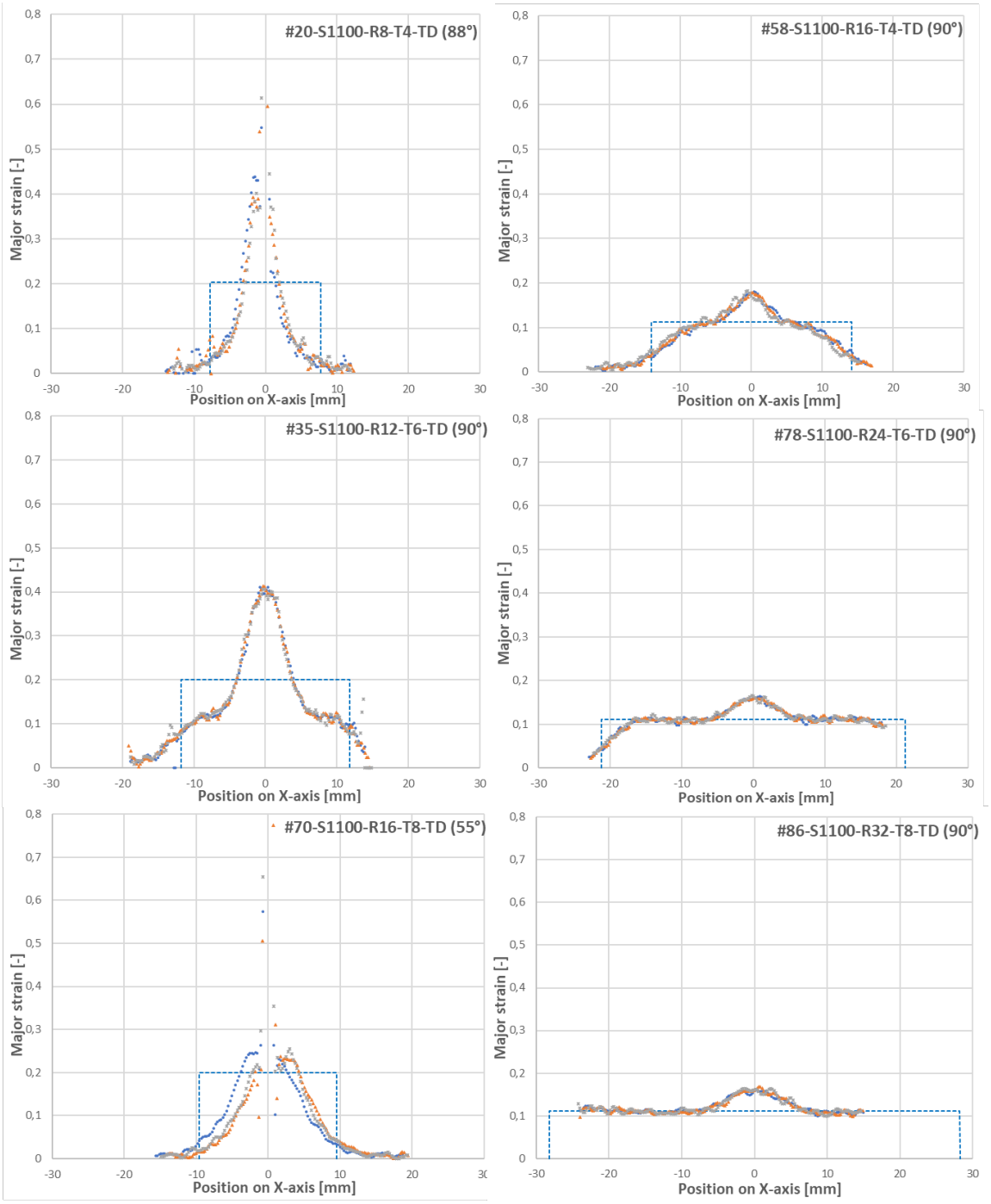
#20-S1100-R8-T4-TD (88°)
#58-S1100-R16-T4-TD (90°)
#35-S1100-R12-T6-TD (90°)
#78-S1100-R24-T6-TD (90°)
#70-S1100-R16-T8-TD (55°)
#86-S1100-R32-T8-TD (90°)
Major strain [-]
Position on X-axis [mm]

Figure 45.

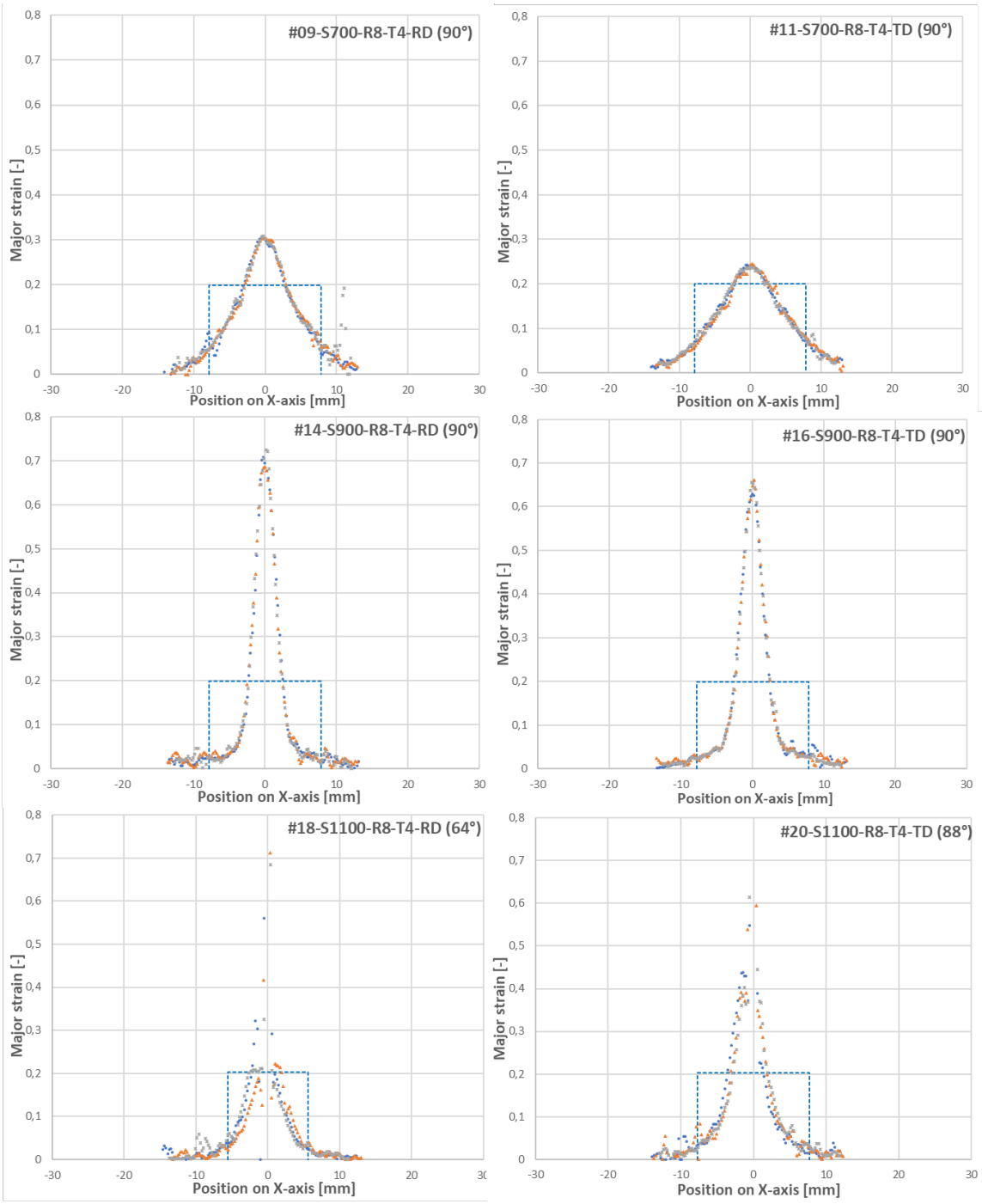
#09-S700-R8-T4-RD (90°)
#11-S700-R8-T4-TD (90°)
#14-S900-R8-T4-RD (90°)
#16-S900-R8-T4-TD (90°)
#18-S1100-R8-T4-RD (64°)
#20-S1100-R8-T4-TD (88°)
Major strain [-]
Position on X-axis [mm]

Figure 46.

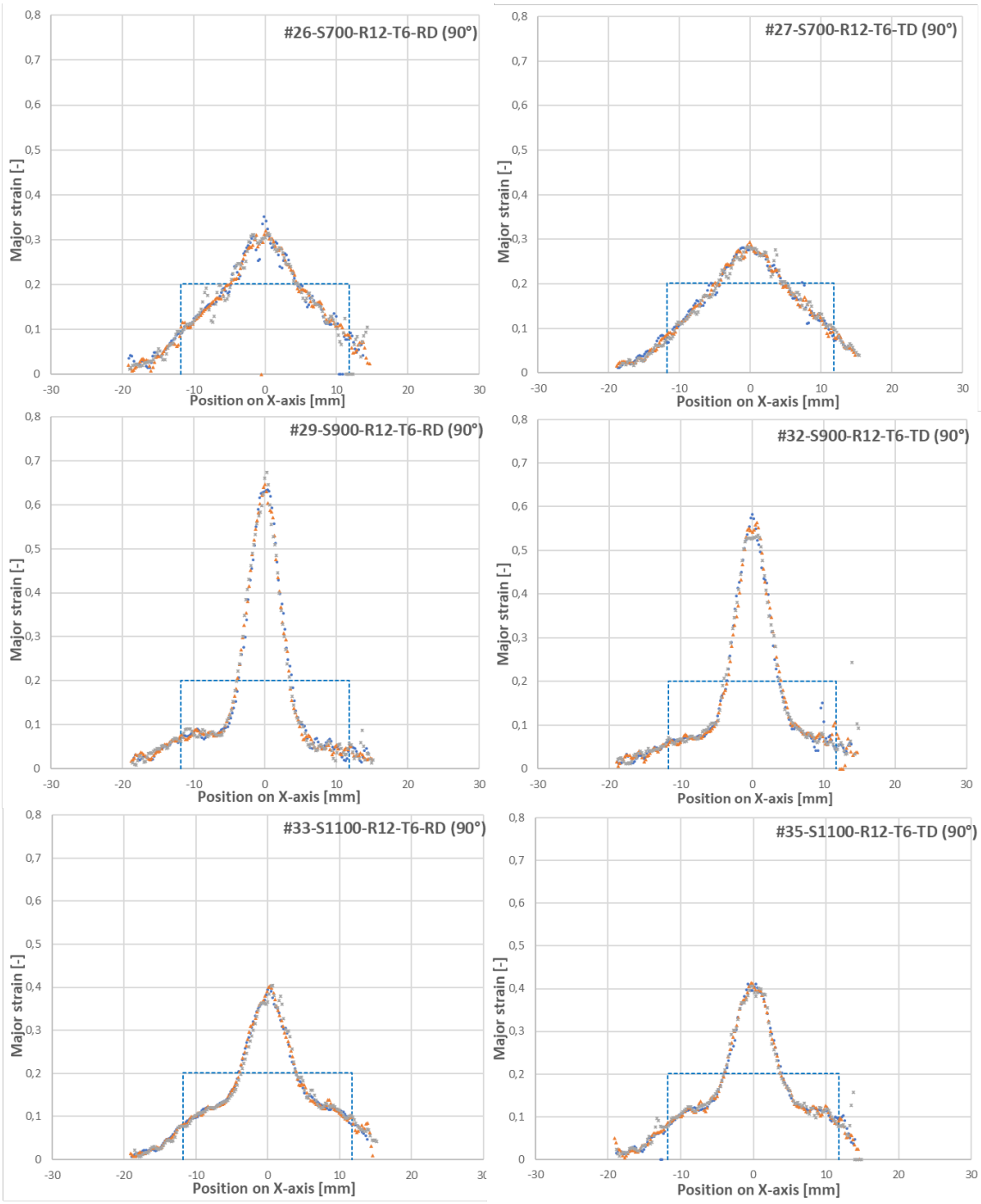
#26-S700-R12-T6-RD (90°)
#27-S700-R12-T6-TD (90°)
#29-S900-R12-T6-RD (90°)
#32-S900-R12-T6-TD (90°)
#33-S1100-R12-T6-RD (90°)
#35-S1100-R12-T6-TD (90°)
Major strain [-]
Position on X-axis [mm]

Figure 47.

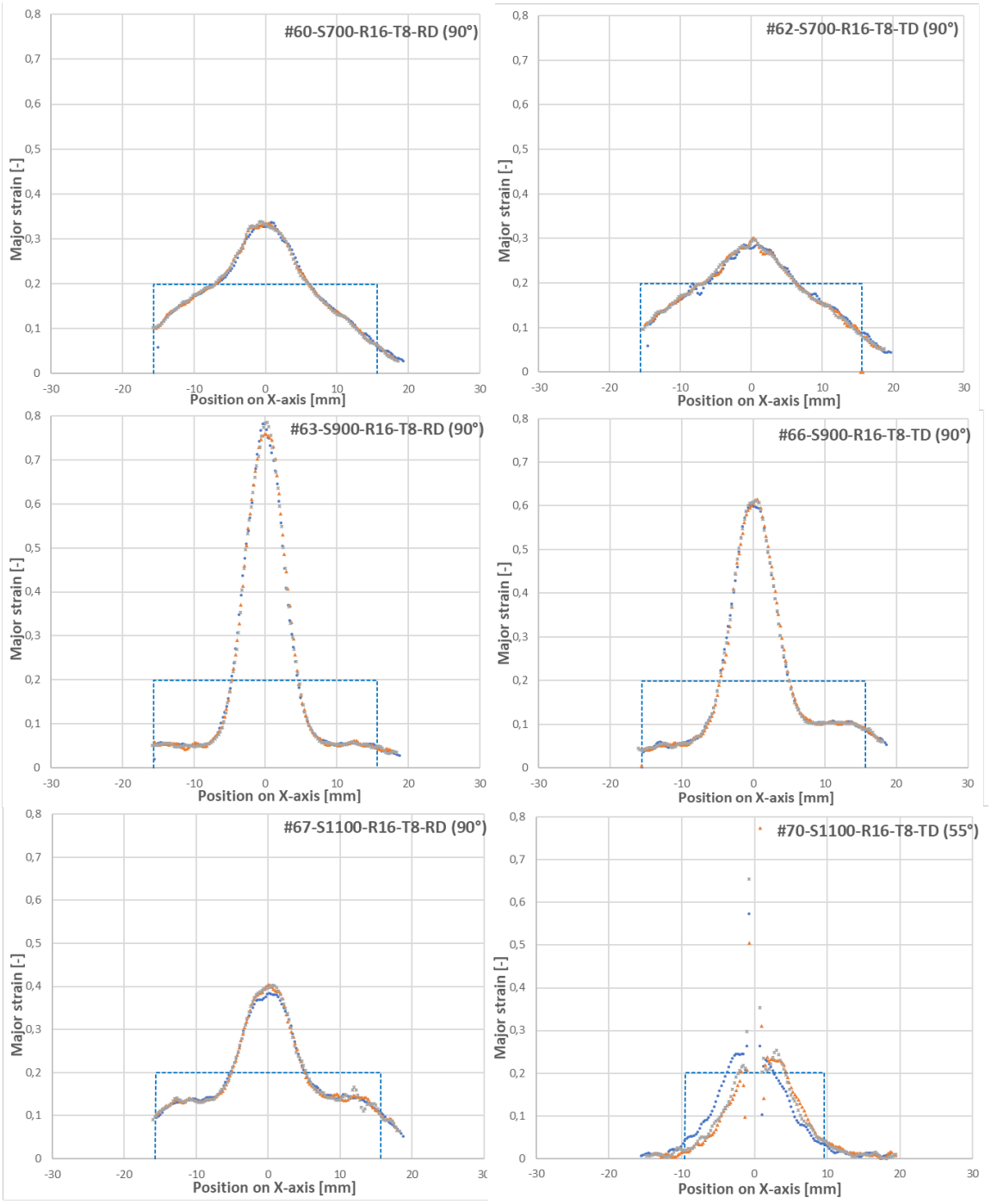
#60-S700-R16-T8-RD (90°)
#62-S700-R16-T8-TD (90°)
#63-S900-R16-T8-RD (90°)
#66-S900-R16-T8-TD (90°)
#67-S1100-R16-T8-RD (90°)
#70-S1100-R16-T8-TD (55°)
Major strain [-]
Position on X-axis [mm]

Figure 48.

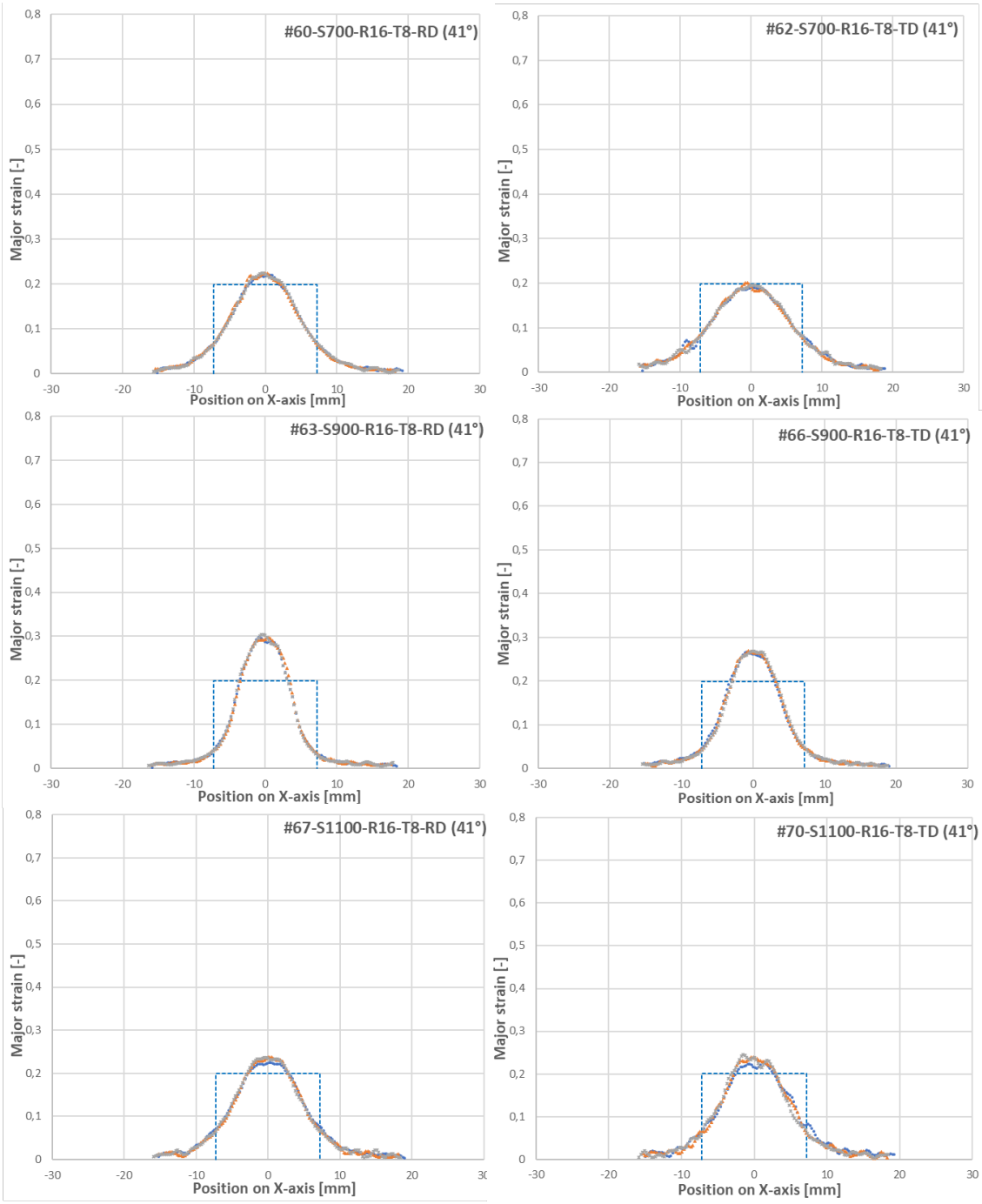
#60-S700-R16-T8-RD (41°)
#62-S700-R16-T8-TD (41°)
#63-S900-R16-T8-RD (41°)
#66-S900-R16-T8-TD (41°)
#67-S1100-R16-T8-RD (41°)
#70-S1100-R16-T8-TD (41°)
Major strain [-]
Position on X-axis [mm]

Figure 49.

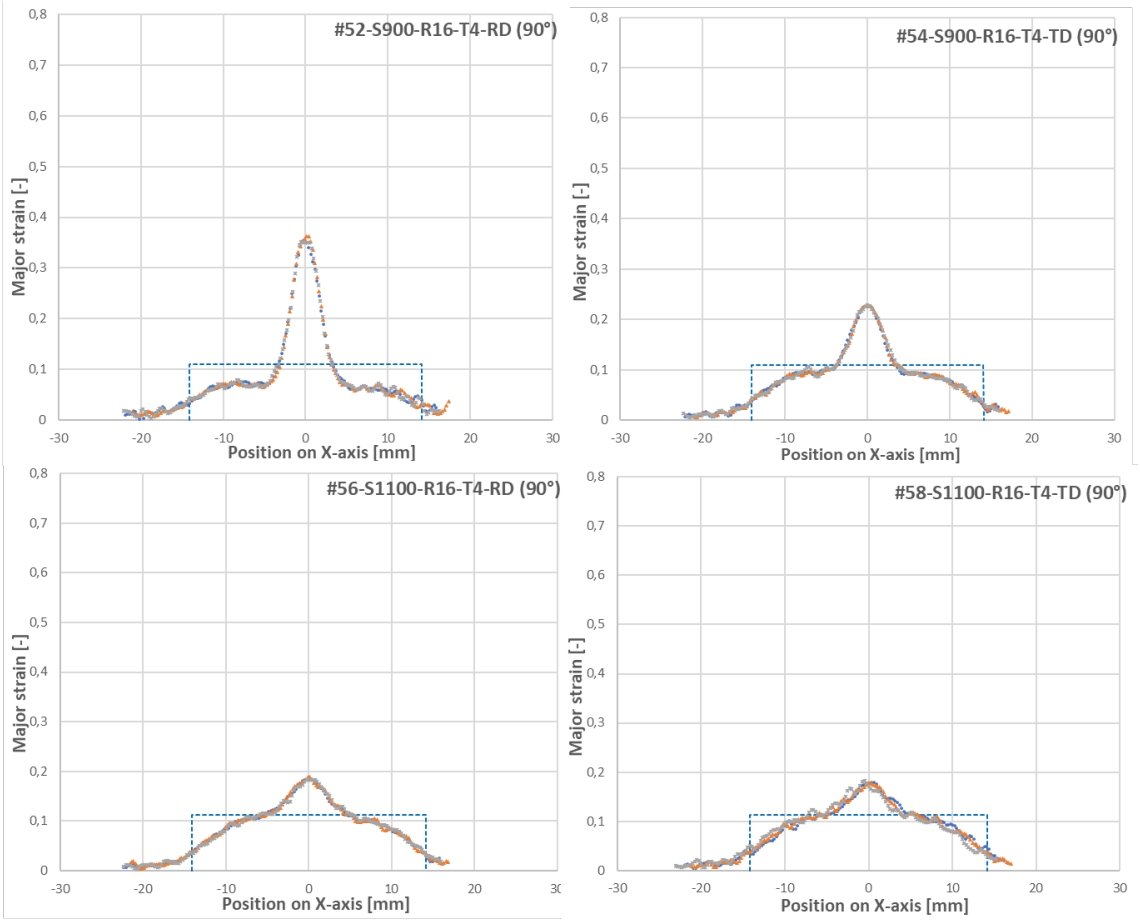

Figure 50.

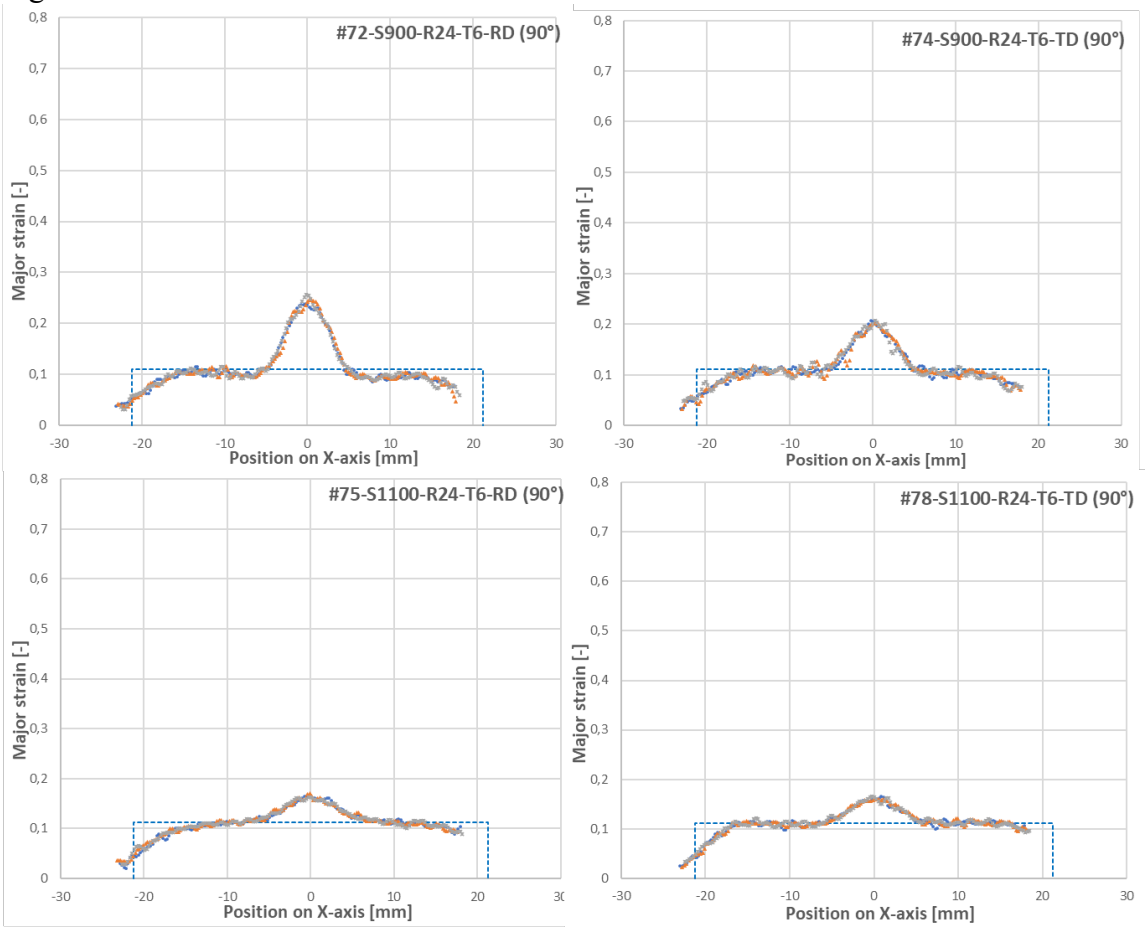

Figure 51

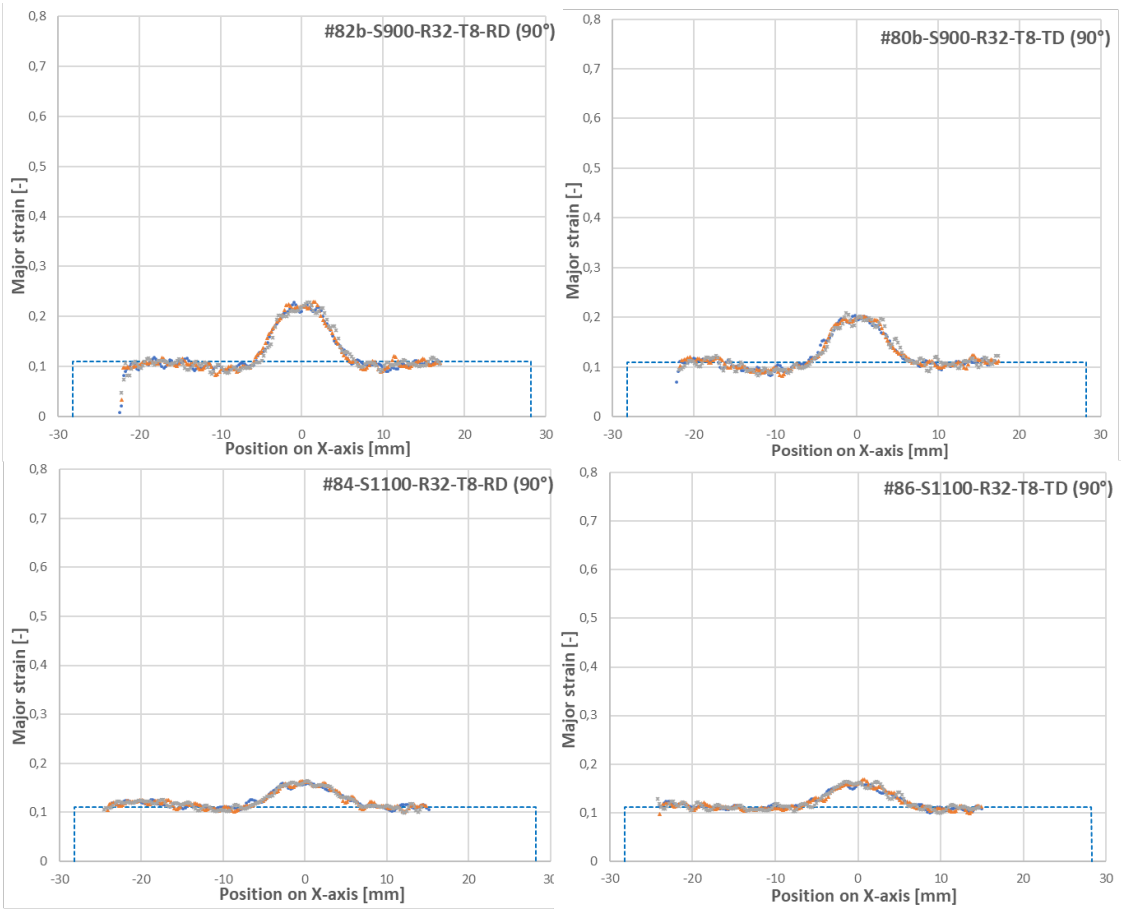
#82b-S900-R32-T8-RD (90°)
#80b-S900-R32-T8-TD (90°)
#84-S1100-R32-T8-RD (90°)
#86-S1100-R32-T8-TD (90°)
Major strain [-]
Position on X-axis [mm]

Figure 52

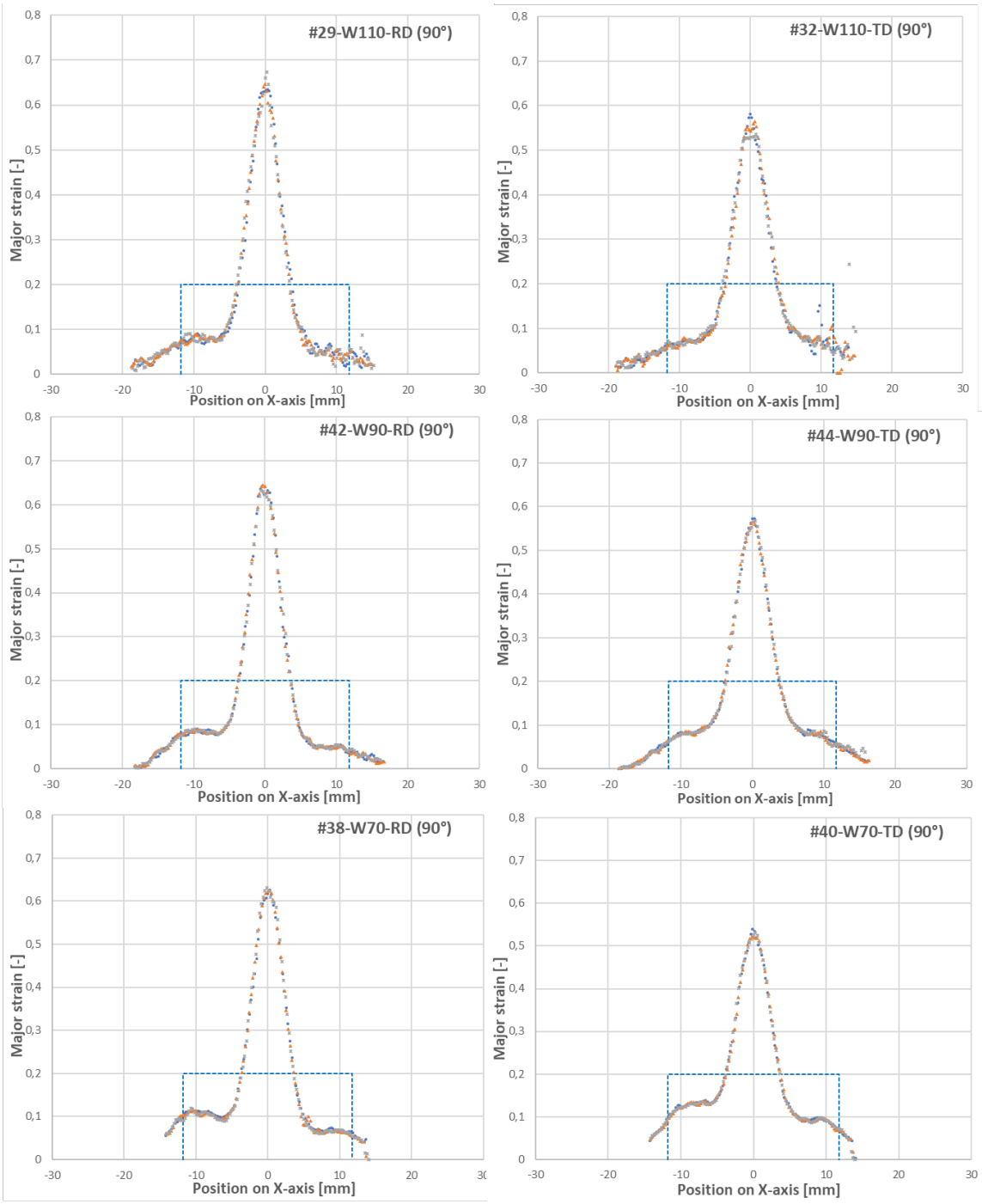
#29-W110-RD (90°)
#32-W110-TD (90°)
#42-W90-RD (90°)
#44-W90-TD (90°)
#38-W70-RD (90°)
#40-W70-TD (90°)
Major strain [-]
Position on X-axis [mm]

Figure 53

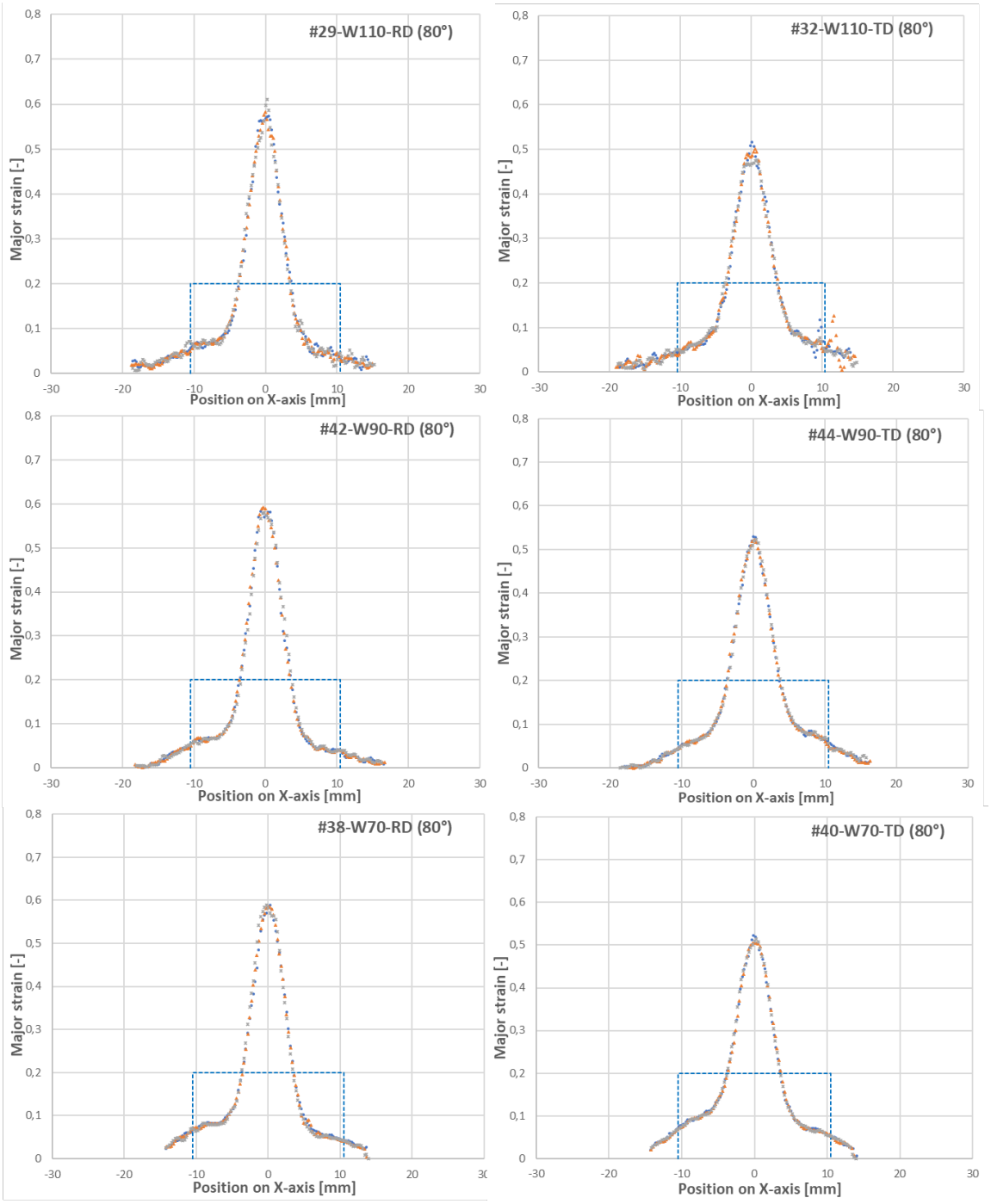
#29-W110-RD (80°)
#32-W110-TD (80°)
#42-W90-RD (80°)
#44-W90-TD (80°)
#38-W70-RD (80°)
#40-W70-TD (80°)
Major strain [-]
Position on X-axis [mm]

Figure 54

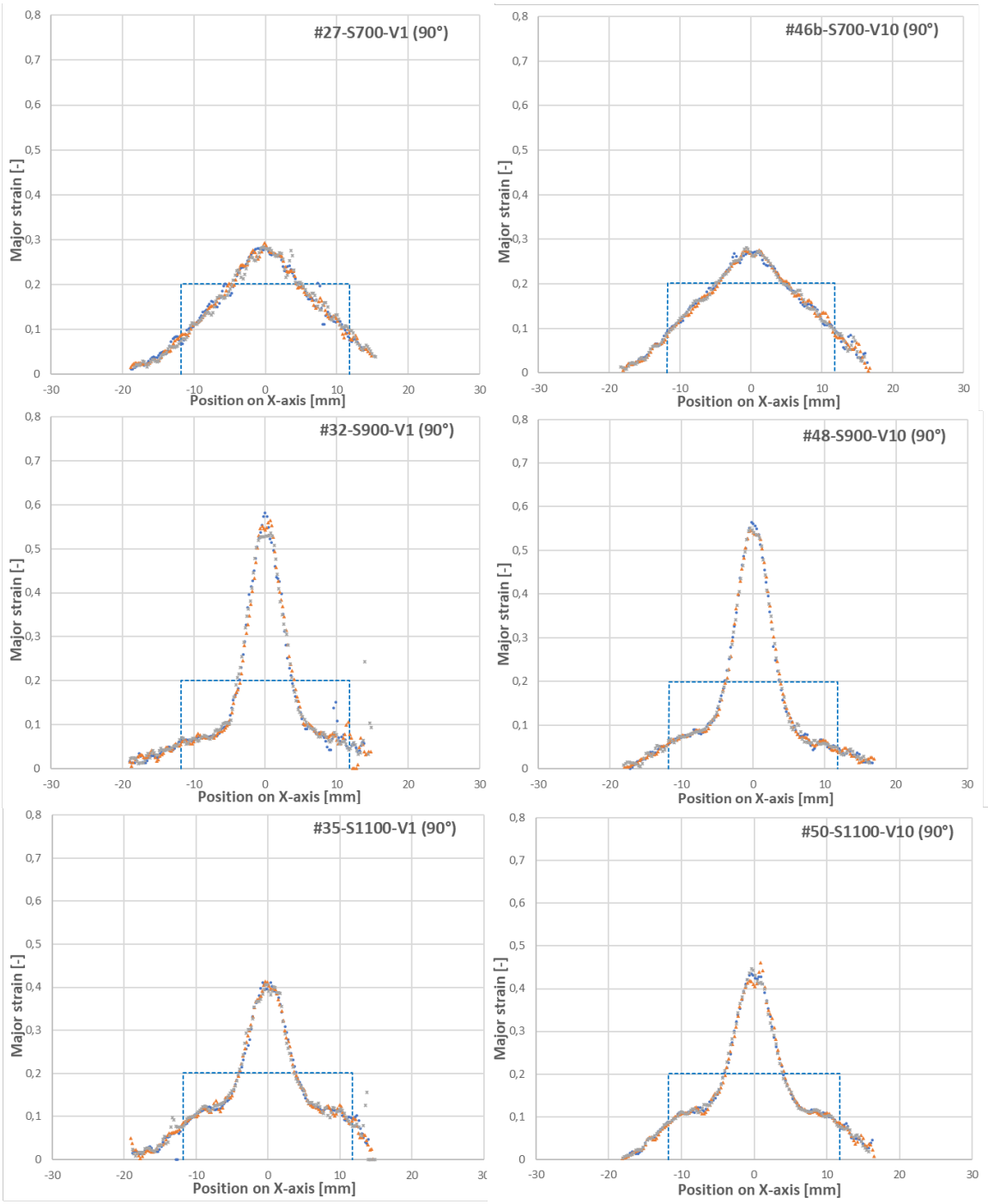
#27-S700-V1 (90°)
#46b-S700-V10 (90°)
#32-S900-V1 (90°)
#48-S900-V10 (90°)
#35-S1100-V1 (90°)
#50-S1100-V10 (90°)
Major strain [-]
Position on X-axis [mm]

Figure 55

Appendix 3. Bending force estimations.

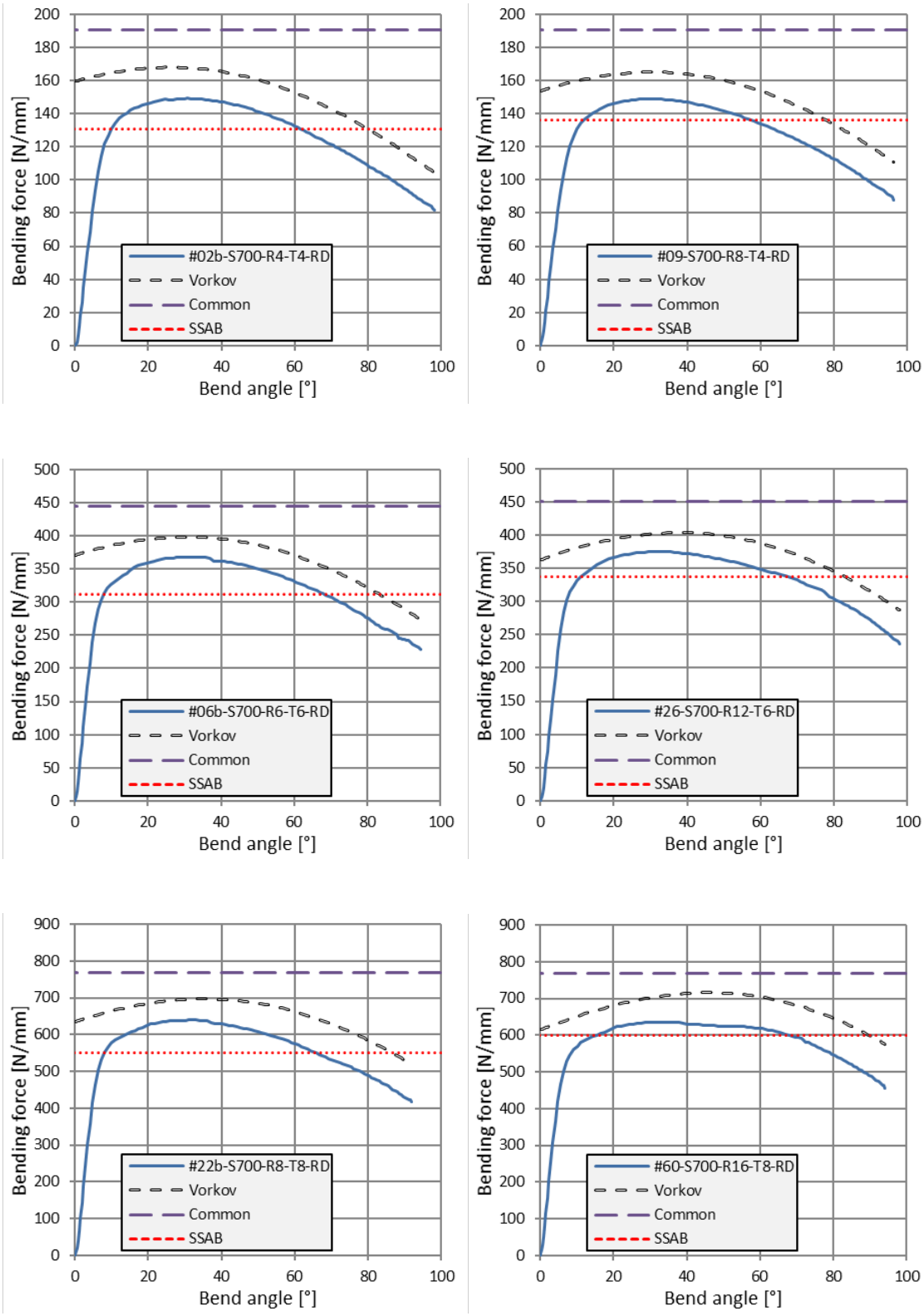

Figure 56. Estimated and measured bending forces on S700.

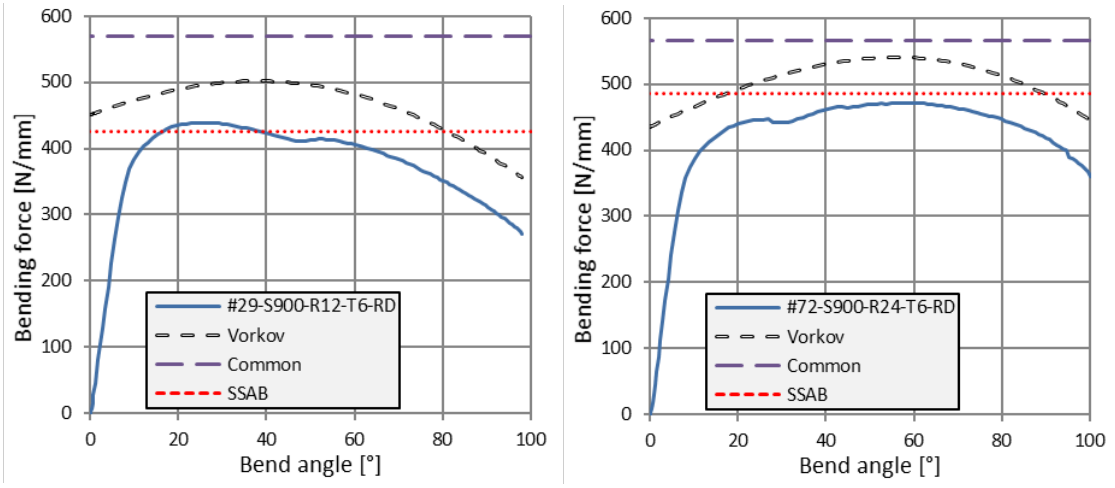

Figure 57. Estimated and measured bending forces on S900.

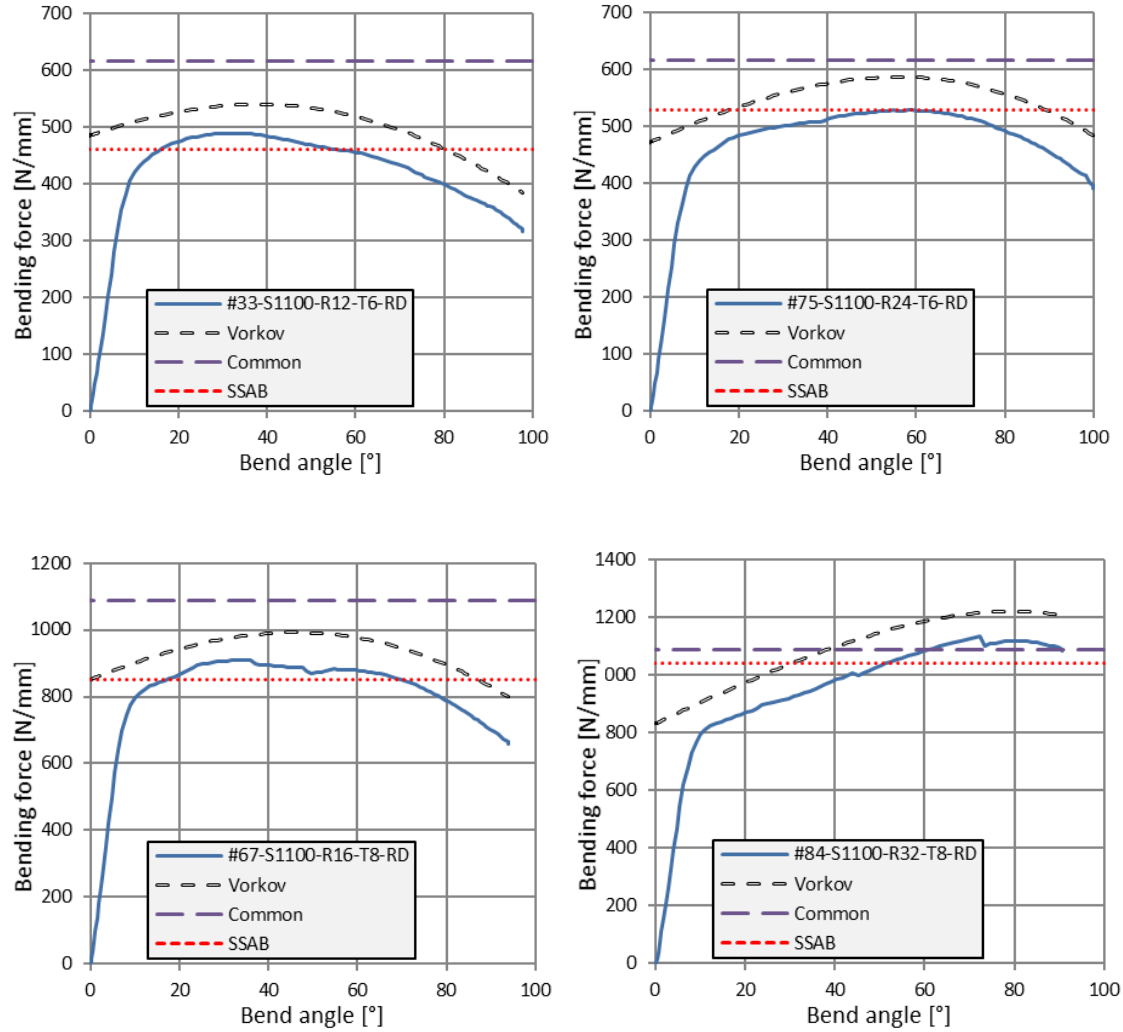

Figure 58. Estimated and measured bending forces on S1100.

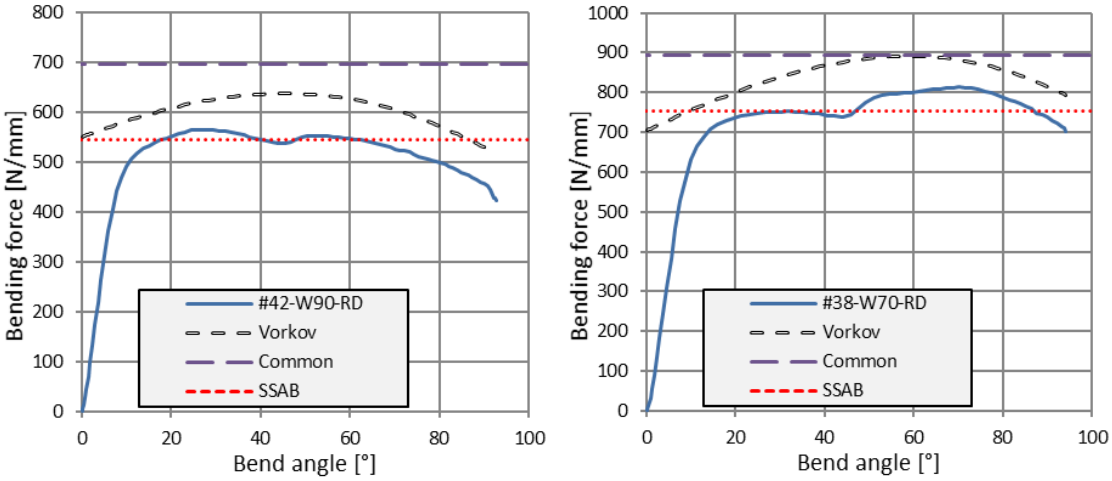

Figure 59. Estimated and measured bending forces on S900 with different die widths.

Appendix 4. Side-view photos and corresponding strain distributions.

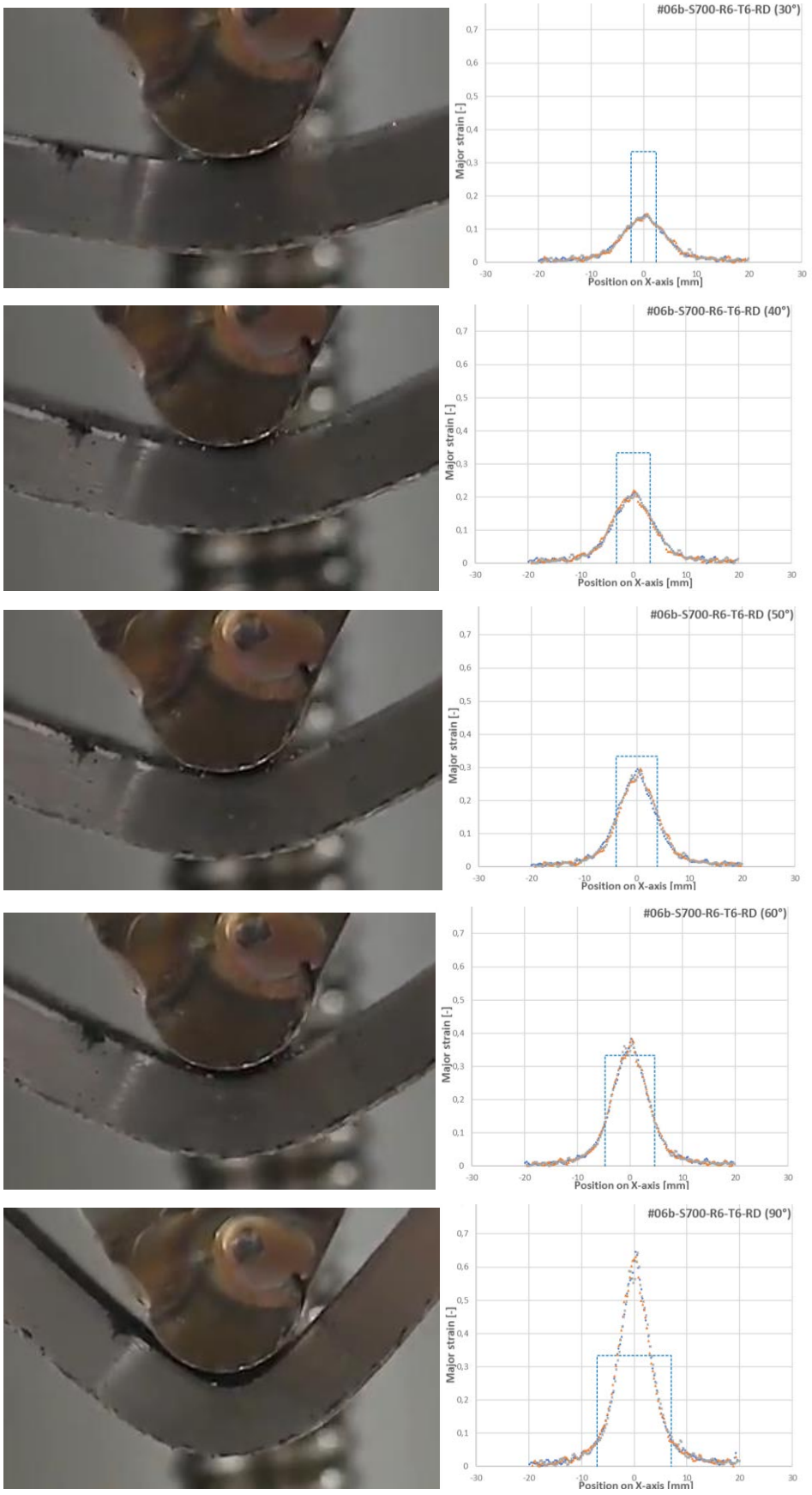

Figure 60. Photos of test #06b at 30°, 40°, 50°, 60° and 90° angles with their corresponding strain distributions.

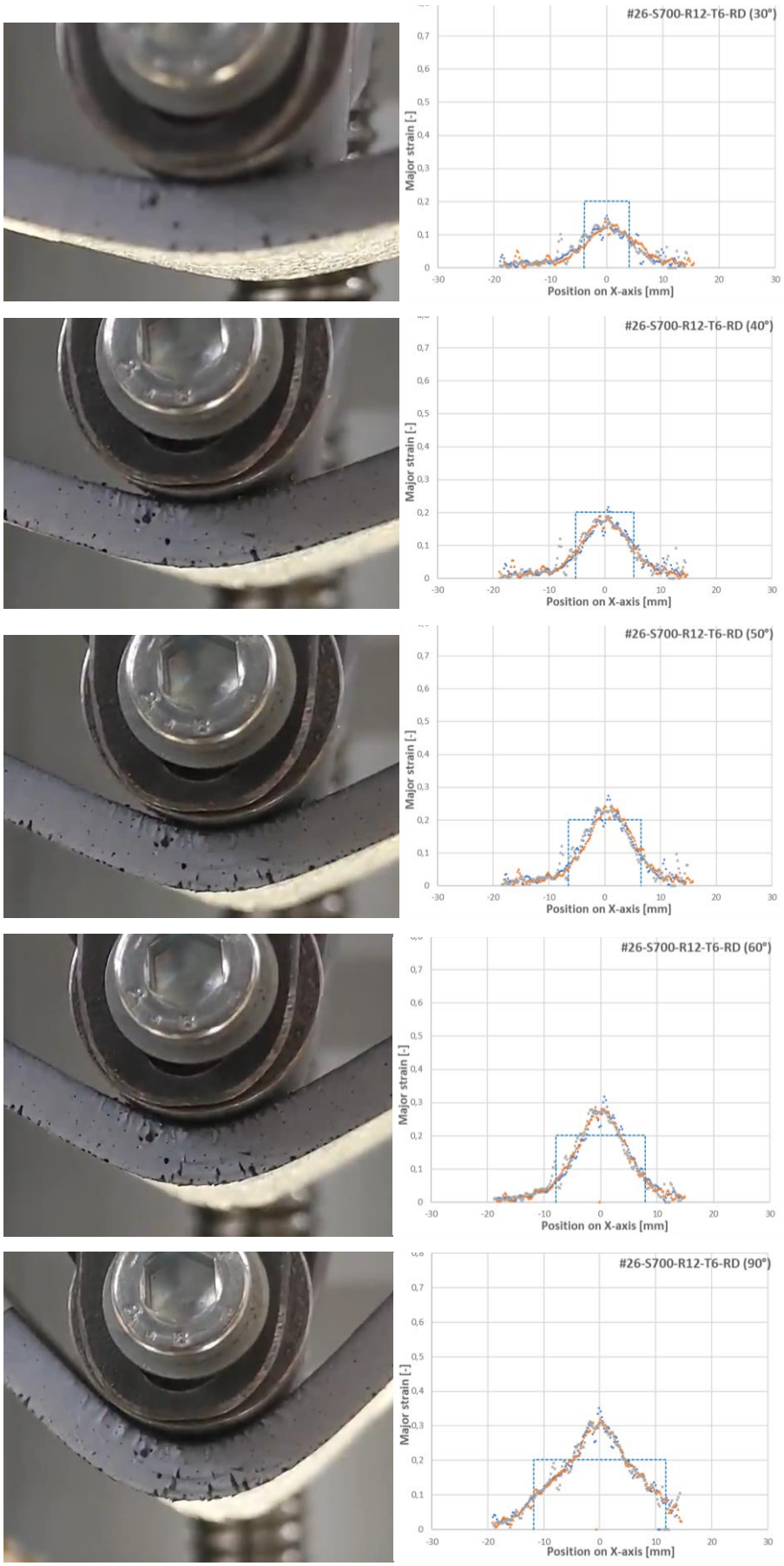

Figure 61. Photos of test #26 at 30°, 40°, 50°, 60° and 90° angles with their corresponding strain distributions.

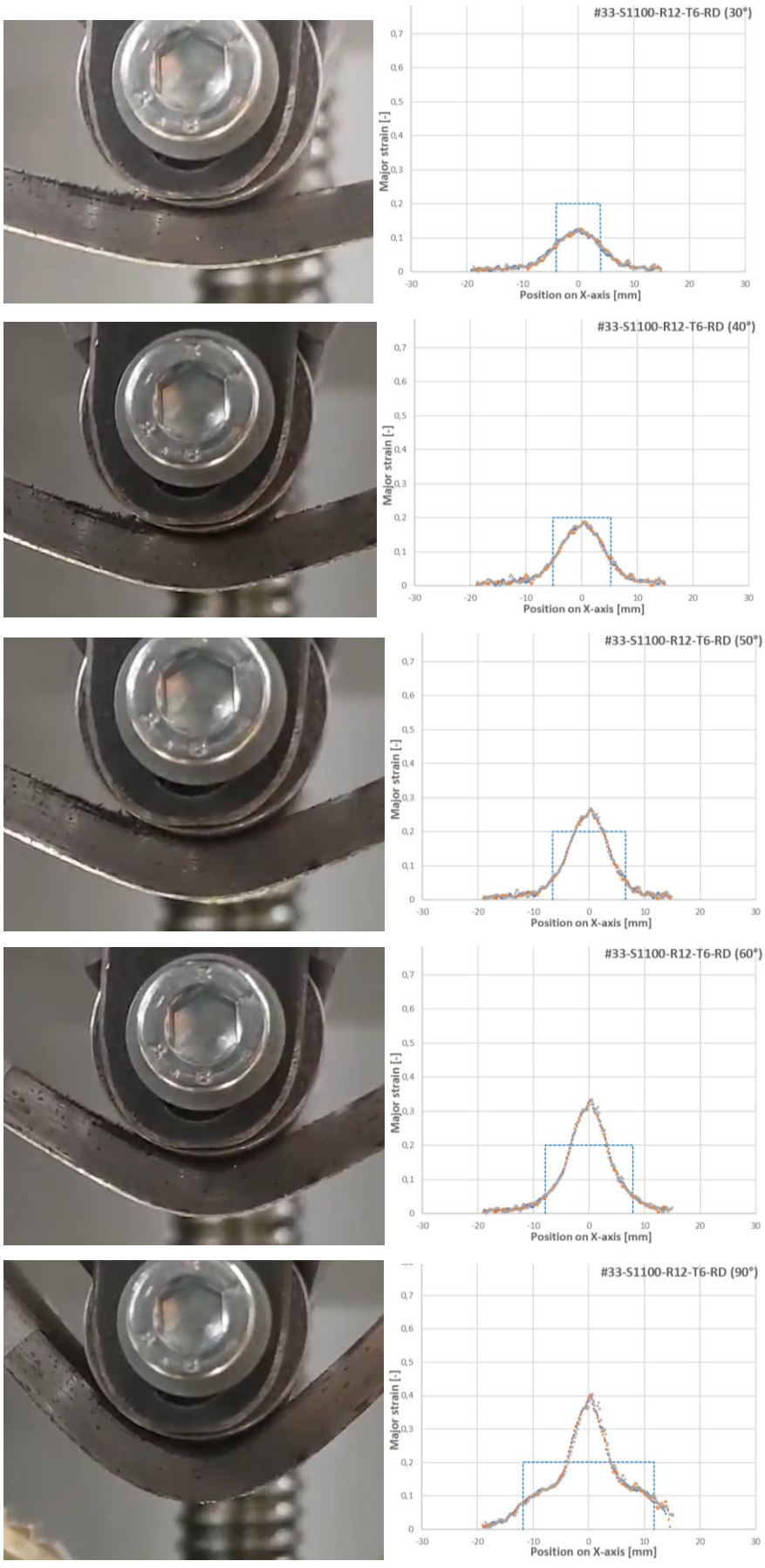

Figure 62. Photos of test #33 at 30°, 40°, 50°, 60° and 90° angles with their corresponding strain distributions.

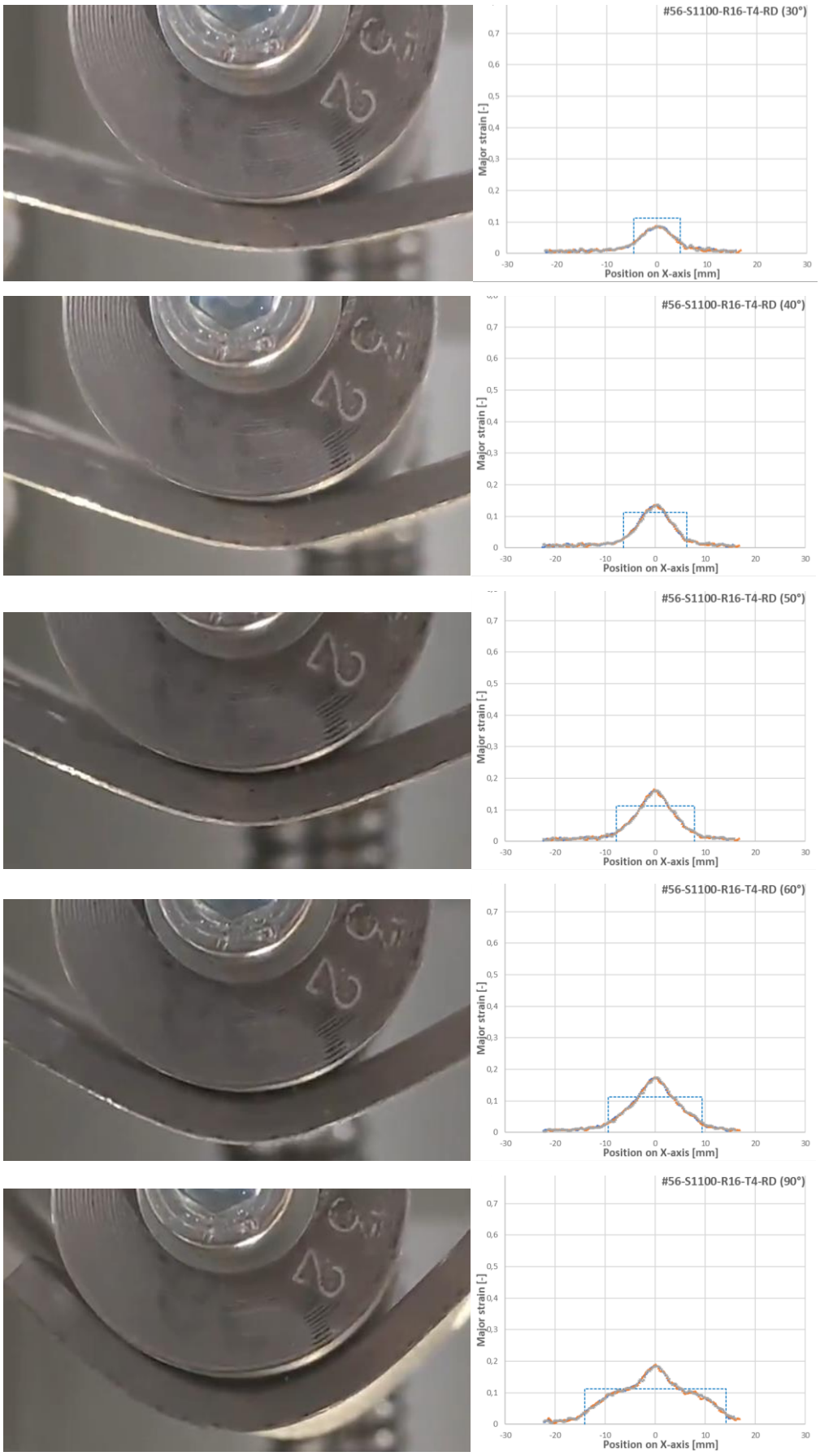

Figure 63. Photos of test #56 at 30°, 40°, 50°, 60° and 90° angles with their corresponding strain distributions.

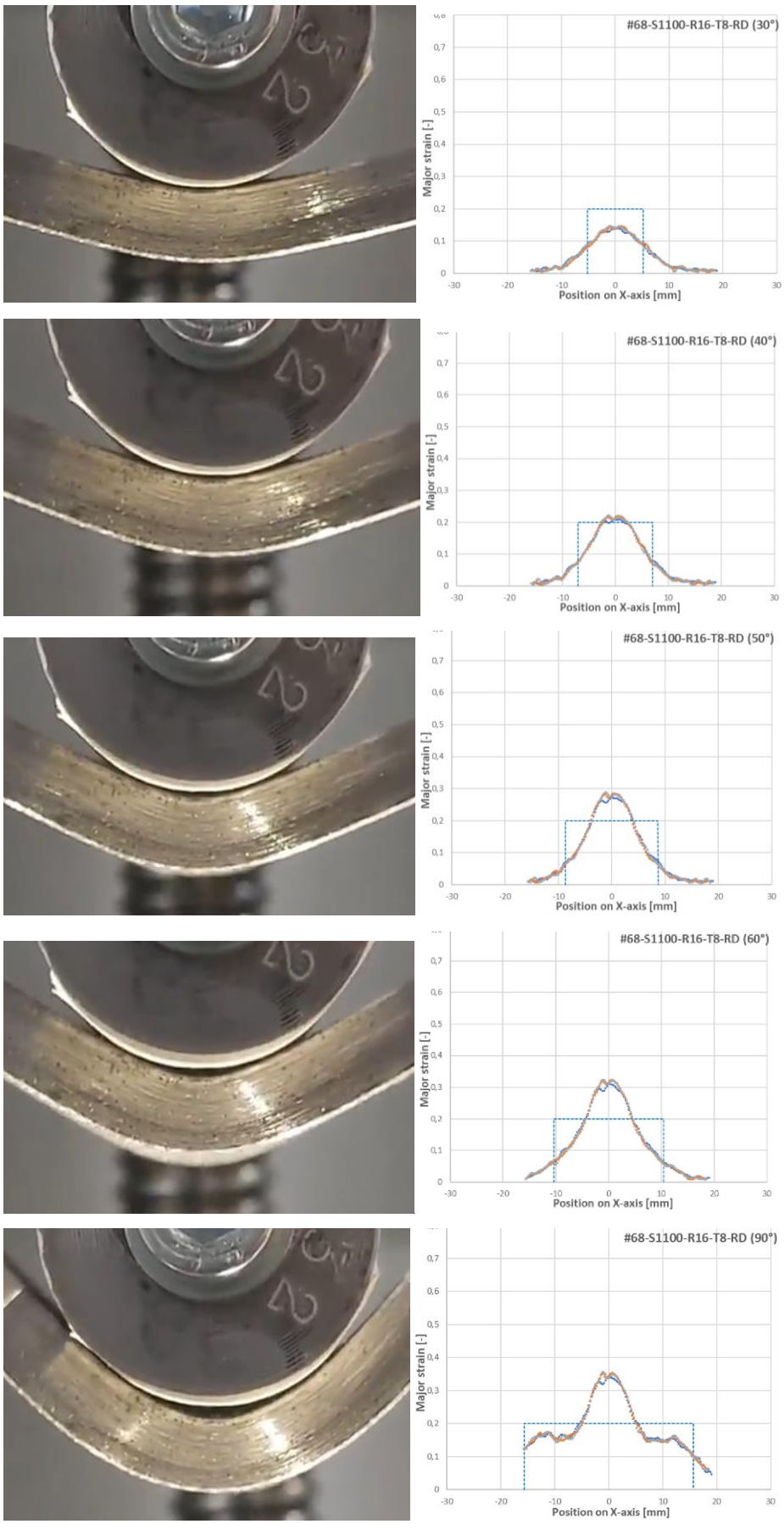

Figure 64. Photos of test #68 at 30°, 40°, 50°, 60° and 90° angles with their corresponding strain distributions.

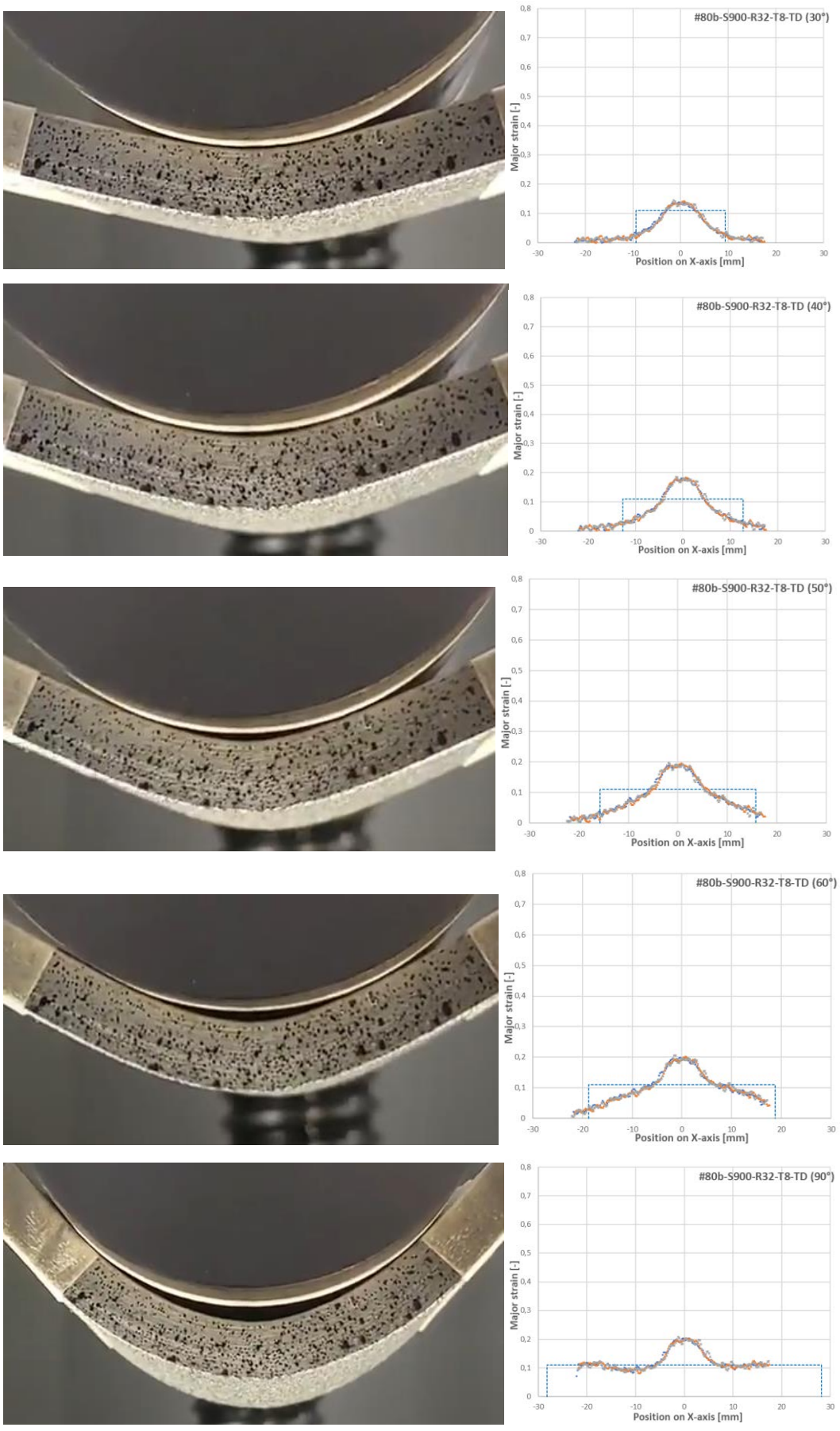

Figure 65. Photos of test #80b at 30°, 40°, 50°, 60° and 90° angles with their corresponding strain distributions.